**Title**
Design of Impact-Resistant Tensegrity Landers

**Author**
Zhang, Alan S

**Publication Date**
2022

# Design of Impact-Resistant Tensegrity Landers

by

Alan S Zhang

A dissertation submitted in partial satisfaction of the

requirements for the degree of

Doctor of Philosophy

in

Engineering - Mechanical Engineering

in the

Graduate Division

of the

University of California, Berkeley

Committee in charge:

Professor Alice Agogino, Chair
Professor Dennis Lieu
Professor Ronald Fearing

Summer 2022

Design of Impact-Resistant Tensegrity Landers

# Abstract

Design of Impact-Resistant Tensegrity Landers

by

Alan S Zhang

Doctor of Philosophy in Engineering - Mechanical Engineering

University of California, Berkeley

Professor Alice Agogino, Chair

Modern emergency response operations increasingly use remote ground-based sensors to provide real-time situational awareness for first responders. However, human users often must personally enter a dangerous situation to place the sensors. The seamless deployment of such sensors without human intervention allows for faster, wider distribution at minimal risk to human lives. This work presents a systematic approach to the design of impact-resistant tensegrity landers capable of autonomous high-altitude aerial deployment of critical sensor payloads in disaster scenarios.

Tensegrity structures are derived from the concept of "tensile integrity" and are composed of rigid rods suspended by elastic cables in a tension network. Their lightweight and flexible properties protect the sensor payload from landing impacts at high velocities. Design equations and simulation models are first used to inform the hardware design of the tensegrity structure and provide upper-bound estimates of viable tensegrity lander designs. A comprehensive range of drop test experiments are conducted to validate the impact behavior and demonstrate the impact-resistance in the highest-altitude drop test experiments of tensegrity landers to date. The experimental results are leveraged to propose empirical scaling laws for the rapid and efficient design of future generations of tensegrity landers. Furthermore, two new tensegrity lander designs, an asymmetrically-weighted structure and a badminton-inspired structure, augment the tensegrity with self-stabilizing functionality to control for the landing orientation of optimal impact mitigation as indicated by the drop test experiment data. The results reveal further opportunities to optimize the design of the structure by aligning the stiffness of the structure with the desired landing orientation. Such a tailored structure can have motorized cables decoupled from the impact event that can then be used to provide locomotion for an ideal hybrid lander-rover tensegrity system.

Overall, the work contributes design methods, reorientation capabilities, and validated hardware prototypes to the grand challenge of tensegrity robotics: demonstrating a fully autonomous tensegrity robot capable of safely navigating through unstructured terrain.

To a bright future. Fiat lux.

# Contents

# List of Figures

# List of Tables

# Acknowledgments

To my dissertation committee members who have supported me with unwavering patience and encouragement: Professors Alice Agogino, Dennis Lieu, and Ronald Fearing. Thank you for all the guidance and insight. Your mentorship means the world to me and I am immensely grateful for the countless ways you have impacted my perspectives on research.

To my faculty mentors who have guided me in my growth as a teacher: Professors Dennis Lieu, Hayden Taylor, Hannah Stuart, Sara McMains, and Oliver O'Reilly. Thank you for setting a shining example of what it means to teach at the university level and helping me find my own path in teaching and learning.

To my colleagues in the Berkeley Emergent Space Tensegrities Lab and Squishy Robotics: Douglas Hutchings, Drew Sabelhaus, Hao Hong, Alberto Ibarra, Mayank Gupta, Grant Emmendorfer, Toni Bronars, Ryan Cosner, and Hadar Gamliel. We did everything we set out to do - build cool robots and drop them from the sky.

To my fellow BESTies in the broader Agogino research group: Andrew Barkan, George Moore, Elena Durán-López, and Deniz Dogruer. Thank you for brightening up my Wednesdays as we navigated the pandemic and the last years of our PhDs together.

To the mechanical engineering department staff: Yawo Akpawu, Isabel Blanco, Ricky Vides, Rene Viray, Irma Paz-Viray, Mike Neufer, Tom Clark, Daniel Paragas, and Scott McCormick. Thank you for being so friendly, welcoming, and ready to support me with anything I needed in my journey.

And finally, to all my family and friends, thank you for the adventure.

# Chapter 1

# Introduction

Modern emergency response operations increasingly use drones and remote sensors to provide real-time situational awareness for first responders. Ground-based sensors in particular can provide the long-term continuous monitoring that aerial drones inherently cannot. However, human users often must personally enter a dangerous situation to place the sensors. The seamless deployment of such sensors without human intervention allows wider distribution and minimizes risk to human lives. Autonomous deployment capabilities – potentially via airdrops – are required to achieve this goal.

This dissertation presents a systematic approach to the design of impact-resistant tensegrity landers capable of autonomous high-altitude aerial deployment in disaster scenarios. Tensegrity structures are derived from the concept of "tensile integrity" and are composed of rigid rods suspended by elastic cables in a tension network. Their lightweight and flexible properties protect the critical electronics payload from landing impacts at high velocities. The work spans the modeling, design, and experimental testing of the tensegrity landers. The primary focus is the hardware design and impact analysis to ensure the safety of the payload. It demonstrates a design methodology that is applicable to building viable tensegrity landers for any given deployment conditions in the future.

The remainder of this chapter frames the background and motivation for using tensegrity structures as landers and then discusses prior work in this problem space. Chapter 2 presents a review of tensegrity geometry, statics, and kinematics. Design equations are used alongside deployment constraints to inform material and manufacturing selections for constructing the hardware prototypes. Chapter 3 derives analytical solutions to model the landing impacts and discusses the simulation tools used to implement them. Chapter 4 analyzes drop test experiment data through a robust sweep of design parameters such as lander size and payload weight. The data is fit against the models to form a series of empirical scaling laws for generating future designs. Chapter 5 is on the rotation control of the lander in free-fall for situations with orientation-dependent sensors such as cameras or antennas. Two solutions are designed with a model-based approach and their self-righting behaviors are validated in experiment. Finally, Chapter 6 summarizes the dissertation and discusses future work and applications for tensegrity landers.

## 1.1 Background and Motivation

Robots can navigate the extreme environments of disaster zones to assist with relief efforts and save lives. Conventional forms of transportation are unable to pass blocked or damaged roads, so humans often must manually transport critical supplies of food, water, and first-aid. Similarly, humans may experience difficulty in traversing the rubble when searching for survivors. In both scenarios, robots that are able to quickly and reliably navigate across uneven terrain provide invaluable benefits in humanitarian crises [1].

Critically, in the immediate aftermath of disasters such as gas leaks and chemical spills, improved situational awareness for first responders at the scene can accelerate rescue operations while also reducing human risks. A key priority in such missions is to minimize the risk to human users who often need to personally enter a dangerous area to manually deploy the sensors. However, safe deployment of delicate sensors and instruments in these environments is not straightforward due to limitations in movement and transportation. Traditional wheeled vehicles have difficulty in the uneven terrain, and while disaster robots provide a promising solution they require human users to be on site for deployment. Alternatively, unmanned aerial vehicles (UAVs) can easily fly over the target zone even as first responders are en route, but they have their own set of limitations. Drones can be used for data acquisition from the air, but they cannot provide persistent monitoring over time as their flight times are limited by a relatively short battery life. Furthermore, they cannot land on the uneven terrain typical of disaster environments and thus they are limited in the ground-level data they can provide. To maximize performance of the system it is possible to combine the UAV with a sensor payload deployable by airdrop into the disaster zone. A variety of strategies have been developed to address the challenges presented by the high landing impacts from airdrops. Most importantly, airdropped payloads must guarantee the safety of any human occupants inside the drop zone. Solutions to mitigate impact such as reducing payload weight, deploying parachutes, and utilizing honeycomb decelerator material have been considered for human safety factors in airdrops [2].

Tensegrity structures are composed of rigid bars suspended by elastic cables inside a flexible tension network based on the principle of “tension integrity” or “floating compression” [3, 4]. The system maintains its shape in static equilibrium by balancing compressive forces in the bars and tensile forces in the cables. In this fashion the rigid bodies are "floating" in space and are supported solely by the elastic cables without contacting any of the other rigid bodies. The structures can then dissipate locally applied forces across the global tension network and thus become mechanically stable and robust to external forces. Theoretically, each member is either in pure tension or pure compression, so there are no amplified forces from moment arms or stress concentrations as seen in conventional robot mechanism designs [5]. Due to the nature of how the members are connected inside of the tension network, the system is capable of global force distribution across all of the members which makes it highly robust to external impacts. Overall, tensegrities are naturally compliant structures characterized by their flexibility, stability, and high strength-to-weight ratios, and these benefits motivate the use of the tensegrity as a soft robotic platform [6].

First developed for art and architecture during the 1960s [7], tensegrities have subsequently been used in many science and engineering applications. They can model the phenomenons of biological structures found in nature across multiple scales [8–10], act as smart sensors [11], form lattice metamaterials for optimized strength at minimal mass [12], and be deployed as controllable structures [13]. They recently have been of great interest in many soft robotic applications that take further advantage of their natural mechanical properties [14, 15]. Lightweight and compliant tensegrity systems are promising solutions in robotic applications that require flexible motion and robust movement across difficult terrain. Researchers are developing multiple forms of tensegrity-based robots in pursuit of this goal. Designs and applications include: simple walking geometries [16, 17], bio-inspired tensegrity joints to mimic natural motion [18], flexible robot spines for quadruped walking robots [19], duct-climbing robots that can traverse narrow vertical spaces [20, 21], programmable structures that have controlled deployment through 3D-printing [22], and spherical probes as planetary explorers and landers [23].

A natural addition to the use of tensegrity structures as planetary landers is the deployment of remote sensors to provide situational awareness in tactical and emergency response operations. Tensegrity structures are ideal candidates for high-altitude autonomous deployment from a UAV due to their light weight, impact resilience, and ability to protect their sensor payload without a parachute or consumable energy-dissipating honeycomb decelerator material. The collapsible design can enable ease of transport and portability. They are easily carried by drones or light aircraft and can be accurately dropped into a target area with relatively low levels of lateral drift. The impact properties such as terminal velocity can be specifically tuned depending on the size of the structure and the payload weight it carries. With the correct design parameters, not only would the robot survive the singular landing impact on unknown terrain from the initial drop, but it would be continually robust to a variety of external disturbances encountered during operation. Furthermore, depending on the desired deceleration properties the tensegrity can often be reused for multiple deployments. Overall they provide an efficient and effective solution to the need for situational awareness and rapid emergency response in disaster scenarios.

## 1.2 Prior Work

The Berkeley Emergent Space Tensegrities (BEST) Laboratory, in collaboration with NASA Ames Research Center, has worked on multiple shape-shifting six-bar spherical tensegrity robots to use as the next generation of planetary landers and rovers for space exploration missions [24]. Due to the robots' promising ability to survive high-altitude landings and subsequently navigate across difficult terrain, the BEST Lab and its spin-off startup Squishy Robotics are also researching the robots' performance as a search and rescue rover deployed by a drone during a disaster scenario. In both types of applications the robustness of the tensegrity structure is critical to mission success and depends on the robot's natural ability to survive drops and absorb impacts.

Prior work has focused on design and control using series-elastic actuation on a standard six-bar icosahedron geometry where each tensile element consists of a cable and spring in series. This configuration provides a good approximation of a sphere with a minimal number of members. The spherical structure is of great interest in a high-altitude deployment application due to its symmetrical nature. Its locomotion capabilities and impact resistance are not completely dependent on its orientation so there is little need to control how the robot lands on the ground or prevent the robot from accidentally rolling over. The robots' current locomotion scheme uses motors to alter the cable lengths and deform the structure, allowing the robot to perform a "punctuated rolling" motion through controlled shape-shifting [25]. For faster and more efficient movement the robot benefits from the additional compliance provided by lower stiffness elastic elements. However, in a typical mission the robot must also be able to survive drops from its initial deployment as well as subsequent landings from rolling down hills or off ledges. In these extremely dynamic events the structure benefits from higher stiffness elastic elements that can reduce the deformation experienced during impact. These two major functionalities of the tensegrity are inherently opposed and ongoing research still seeks to fully develop the tensegrity landers' dual capabilities.

While there has been work on simulating the robots during drop tests or hopping motions there are few quantitative drop test experiments on the physical robot itself. The simulations alone are not sufficient to understand the impact dynamics as they often use ideal assumptions and simplified dynamics. Therefore the results do not fully capture the impact behavior of the structure. In terms of hardware design some measures such as cushioned end caps have been explored to reduce damage to the structure during impact, but a better understanding of the structural response is needed to identify critical failure points and implement impact-resistant designs in their place.

This work analyzes the robots' impact characteristics and evaluates the tensegrity structure's protective properties during a wide variety of experimental landing scenarios. The primary focus is on the autonomous delivery of sensors using tensegrity robots that are capable of being deployed from commercial drones or other aircraft. These robots use the impact-resilient tensegrity structure as a protection apparatus for the rapid delivery of a sensor payload from an aerial vehicle to the ground. The research leverages the tensegrity structure and its associated benefits to design a novel robot specifically built to protect the payload and survive impacts after being dropped from a large height. Initially designed for commercial use in Hazardous Materials (HazMat) scenarios, the robot can also be customized for other uses including CBRN (Chemical, Biological, Radiological, Nuclear) situations, wildland fire monitoring, and small medical supplies delivery. In particular, this robot can withstand repeated drops of over 100 m while safely carrying a payload with visual, chemical, and atmospheric sensors commonly used for emergency response. It can survive these impacts using structural compliance alone, without the use of additional landing equipment. This capability enables the robot to utilize its passive compliance towards many advantageous properties such as faster deployment, reduced upkeep costs, and increased structural robustness, for an overall advancement in the range of robot capabilities during disaster response scenarios.

# Chapter 2

# Tensegrity Design

## 2.1 Six-bar Spherical Tensegrity

Valid tensegrity systems of various form factors can be found to meet virtually any size and shape constraint [26]. In particular, the tensegrity system studied in this work is the six-bar spherical tensegrity structure, one of the more commonly researched tensegrity configurations in the literature. It has the best approximation of a sphere for the number of members in the system and has an open volume in the center of the structure to suspend a sensor payload. Tensegrity forms exist for rounder spheres, but increasing amounts of additional members are needed for each improvement in the spherical approximation [27], causing the control of such a system to be prohibitively complex. The six-bar tensegrity thus has an optimal balance of spherical shape and simplicity of design. Due to its symmetry it is relatively easier to model and control, since the locomotion capabilities and impact resistant are not completely dependent on its orientation in space.

The topology of the six-bar spherical tensegrity robot is based on a tensegrity structure that consists of six rods and twenty-four cables (Fig. 2.1). The six rods are divided into three parallel pairs aligned with the Cartesian axes. Another name for the six-bar tensegrity, "expanded octahedron", is derived from linearly offsetting each of the three primary axes of an octahedron to form these six rods. Each rod end is connected by four cables to neighboring rods but never to its parallel paired rod. This creates a structure with eight equilateral triangle faces and twelve isosceles triangle faces which are formed by the position of the rod ends. As not all nodes are connected by cables, each of the twelve isosceles triangles are referred to as open faces with cables connecting two of their three edges. The eight equilateral triangles are referred to as closed faces with cables connecting all three edges. The discrepancy in the sizes of the triangular faces is caused by the tensegrity forming a Jessen's icosahedron rather than a true icosahedron due to the self-tensioning properties of the system.

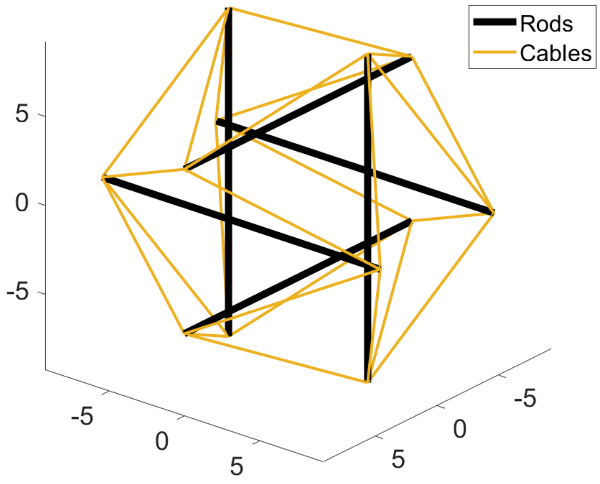

Figure 2.1: Representative plot of a six-bar tensegrity structure. The rod pairs are aligned with the coordinate axes.

## Prior Work on Six-bar Spherical Tensegrities

Numerous mechanical models have been developed to analyze valid tensegrity configurations generated from the tensegrity form-finding problem [26]. The solutions typically focus on small deviations from the unique equilibrium states of tensegrity structures and depend on solving for the minimal potential energy in the system at each position. While some prior work does not explicitly analyze the six-bar tensegrity structure, the fundamental methods and resulting findings are generalizable and readily applied to all tensegrity structures. The stiffness of the structure is based on the tensegrity member connectivity, geometry, material properties, and the prestress of the tensegrity cables [28]. Increased pretension makes the system stiffer and more robust to external loading as more force is required to make a string go slack and greatly impact the mechanical response of the structure. Furthermore, equally scaling the prestress of the entire system will increase the potential energy while still maintaining its consistent shape [29, 30]. The structural stiffness changes as different bending or compressive loads are applied to the tensegrity system. In compression, the stiffness will generally increase with the applied load but will ultimately drop to zero at a critical external force to fully collapse the structure in a characteristic dual-regime stiffening-softening response [31, 32].

Generalized equations of motion have subsequently been derived to analyze the dynamic behavior of tensegrity structures. As with the form-finding process, the equations model the structures around equilibrium configurations for ease of analysis before linearizing the system dynamics for the complete solution [33–35]. Initial solutions have been considered for planar, one degree-of-freedom structures [36, 37] and then extended into higher order systems [38].

In most cases, studies of tensegrity dynamics have been motivated by developing control laws to manipulate the member lengths of the structures for deployment. Tensegrities are controllable structures that require relatively low energy to change shape. If they can be reconfigured into a new equilibrium position, then no additional energy is needed to maintain the new shape of the structure [29]. Many different control strategies have evolved to generate complex motions using tensegrity structures. Depending on the purpose of the robot the motion could be constrained along a prescribed path or range of motion such as for a flexible robot spine [19]. For a spherical tensegrity robot the primary goal is to find locomotion schemes that support the needs of the planetary exploration or disaster search-and-rescue mission [39]. Such control algorithms utilize the symmetry of the structure to achieve a consistent and repeatable rolling or walking motion that can be used when the robot is sitting on any of its icosahedron faces. The control of a six-bar structure has been shown to be governed by a finite set of ordinary differential equations (ODEs) parameterized by a set of eighteen generalized coordinates [40]. In most practical robotic systems the processing power might not be able to adequately control all these variables and provide sufficiently low response times needed for locomotion, leading researchers to search for ways to estimate actuation parameters [41] or automate the control using reinforcement learning [42, 43]. In addition, alternative methods of locomotion that do not depend on the complex control of bar or cable lengths have been explored, such as vibrating the structure to move along a surface [44] or inserting propeller blades into the structure for short-distance flights or hops [45], but these methods are less predictable and reliable than the traditional cable-based locomotion schemes.

Of particular interest is the model presented for a two-stage tensegrity structure in [6]. While the overall shape and size are the same, the two-stage tensegrity structure differs from the six-bar structure in several ways. It is considered to be two stacked three-bar tensegrity prisms joined together by a slight overlap rather than a single structure, and the top and bottom faces are assumed to be rigid, homogeneous plates rather than three independent cables that form a triangular face. Nevertheless, the remaining physical assumptions as well as the approach to modeling and analysis were formative to how future researchers studied tensegrity structures. The following discussions in this work will use their defined cable classification nomenclature. When resting on a triangular base, the six-bar tensegrity structure has three unique cable types (in addition to the cables on the top and bottom faces, which were not considered in their model): 1) *Saddle* (S) cables that connect one rod from each stage and form the outer circumference of the spherical tensegrity, 2) *Vertical* (V) cables that connect rods of the same stage, and 3) *Diagonal* (D) cables that connect one rod from each stage (Fig. 2.2). Each triangular face of the six-bar tensegrity, with the exception of the top and bottom faces, is composed of exactly one cable of each type and defines the structure as an SVD-class tensegrity [46].

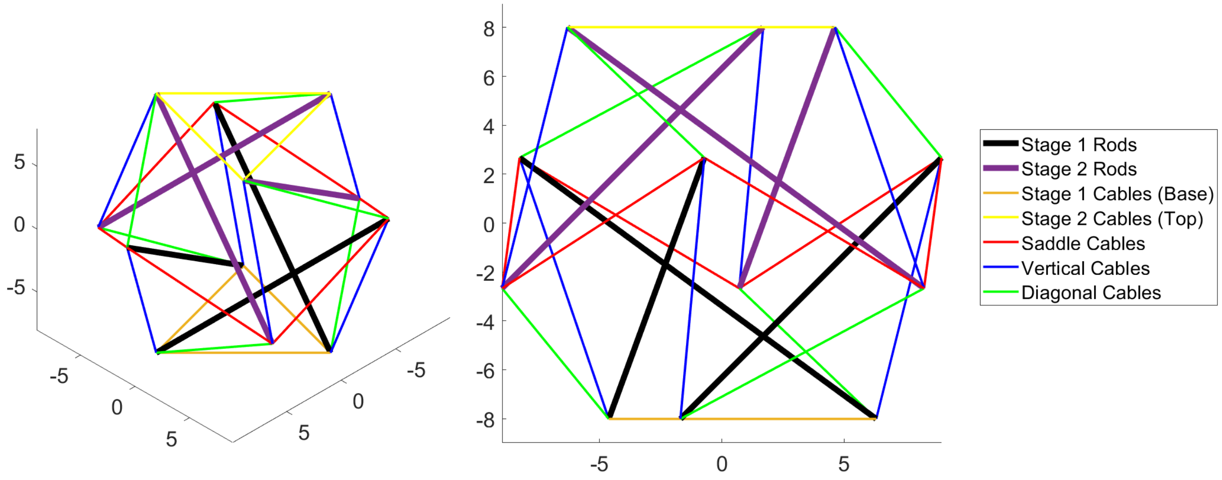

Figure 2.2: Isometric (left) and side (right) views of two-stage SVD (six-bar) tensegrity structure resting on its triangular base

## 2.2 Design Equations

The following series of design equations are proposed in the context of designing tensegrity structures to withstand landing impacts. They are meant to be used as a high-level first pass for hardware parameters of the landers specifically and would lead to excessively robust designs for a controllable mobile robot that is not currently being deployed from high altitudes.

### Geometric Parameters

The first choice of physical parameters for the six-bar tensegrity structure is often the rod length $L_r$ to get a general sense of the overall size of the lander. The rod pairs are nominally spaced a distance of $\frac{L_r}{2}$ apart to form the structure. Although the real value deviates slightly due to the properties of Jessen's icosahedron, modeling the geometry as a regular icosahedron is both simpler and sufficiently accurate when building the physical prototypes. The cable length $L_c$ can be calculated as an edge of the icosahedron assuming that the tensegrity is stable and well-tensioned,

$$L_c = \frac{1}{2}\sqrt{\frac{3}{2}}L_r \tag{2.1}$$

Each edge of the six-bar tensegrity structure has equal length in the static condition based on its inherent symmetry. The radius $r_s$ of a circumscribed bounding sphere for a regular icosahedron of edge length $L_c$ is

$$r_s = \frac{L_c}{4}\sqrt{10 + 2\sqrt{5}} \tag{2.2}$$

Choosing the correct size of the tensegrity lander will depend on deployment options such as the necessary deceleration for the payload. With increasing rod length, there is more open volume contained by the tensegrity for the payload's stopping distance during impact. The size increase of the tensegrity also comes at a relatively low cost of increased mass due to the sparse nature of tensegrity structures. However, scaling the structure too far might result in inefficient use of the limited capacity of planes or drones, although the structures can be packed flat before deployment. This deployment option requires mechanisms to provide external forces to hold the structure in a non-equilibrium state and then intelligently release the structure mid-flight, and will not be covered in the scope of this work.

## Rod Forces

When the tensegrity structure impacts the ground, the majority of the ground reaction forces are initially directed through the rods before being dissipated throughout the rest of the structure. If the rods are impacting at an angle they will experience both normal (compressive) and shear force components along the length of the rod and across the cross-section, respectively. A maximum value for the force components can be found when the rod is either impacting the ground horizontally (highly unlikely given the structure size and rod interactions) or vertically (as seen in Fig. 2.1). This vertical landing orientation for the rods is therefore a worst case condition for the forces experienced by a single rod. Rod material failure in this mode is generally through compressive stress $\sigma_c$,

$$\sigma_c = \frac{F_c}{A_{rod}} \tag{2.3}$$

where $F_c$ is the normal force, and $A_{rod}$ is the cross-sectional area of the rod. The rod may also fail through buckling forces,

$$P_{cr} = \frac{\pi^2 EI}{(KL)^2} \tag{2.4}$$

where $P_{cr}$ is Euler's critical buckling load, $E$ is the Young's modulus of the column material, $I$ is the area moment of inertia of the column, $K$ is the column effective length factor (taken to have a value of 0.65 given the fixed rotation and translation of the tensegrity rods), and $L$ is the unsupported column length. It has been shown that the onset of buckling is an excessively strict criterion for tensegrity failure, and that remaining within the elastic buckling regime can benefit the impact behavior and optimize the mass and strength of the structure [47]. The landing force $F_{land}$ can be estimated using the change of momentum of the system,

$$F_{land} = \Delta(mv) = m\Delta v \tag{2.5}$$

where $m$ is the mass of the tensegrity structure and $v$ is its velocity, which is in turn estimated through conservation of energy $E$,

$$E = mgh = \frac{1}{2}mv^2 \tag{2.6}$$

where $g$ is gravitational acceleration and $h$ is the drop height of the lander. The tensegrity landers have a low rebound velocity after impact so for an additional safety factor in the design $\Delta v$ can be considered to be approximately equal to the landing velocity. Making a conservative assumption that the entirety of the landing force is focused on a single rod, material parameters can be chosen to meet the strength requirements for landing with a generous safety factor. Since it is more likely for slender rods to experience buckling than compressive failure, it is also necessary to consider the total energy absorbed by the structure and compare it to the energetic toughness of the rod material.

## Cable Forces

By definition, the cables of the tensegrity structure will only experience tensile loads. Any compressive or lateral loads will cause the cables to collapse, lose tension, and temporarily decouple from the rest of the tensegrity structure. Although it is possible for cables to experience this during impact, the near-instantaneous response of the structure to return to equilibrium does not justify modeling the tensegrity as a function of the number of slack cables. For example, consider a single slack cable within the structure: the two rod nodes it is connected to must have moved closer together than their static equilibrium distance. As a result the three other cables attached to each of these rod nodes have been extended past equilibrium and will provide a large restoring force to bring the rods back to their starting position, demonstrating the flexibility and robustness of the structure.

The cables will experience a tensile stress $\sigma_t$,

$$\sigma_t = \frac{F_t}{A_{cable}} \tag{2.7}$$

where $F_t$ is the tensile force applied to the cable of cross-sectional area $A_{cable}$. Cable failure will be governed by the yield strength of the material. When the cable also includes elastic elements, they will experience the same total force through the cable assembly but undergo much higher deformation. Springs are limited by their maximum elastic extension, after which they will begin to plastically deform and lose their elasticity. The force needed for a spring's elastic extension $F_{spring}$ is given by

$$F_{spring} = kx + F_0 \tag{2.8}$$

where $k$ is the spring constant, $x$ is the amount of linear deformation or extension, and $F_0$ is the initial tension of the spring. Springs are rated by the maximum forces they can withstand before failure, and the cable forces must be designed around this limit. It is important to understand that any additional pretension in the springs will make the tensegrity structure stiffer as previously stated, but effectively reduce the amount of additional impact energy they can withstand. Since the springs around the entire structure will be passively absorbing impact energy, conservation of energy can again be used to equate the sum of all spring energies in the system to ensure that the springs remain in their operational limits,

$$E = mgh = \sum_{i=1}^{24} (\frac{1}{2} k_i x_i^2 + F_{0,i} x_i) \tag{2.9}$$

However, not all of the impact energy is purely transferred into the springs, and not all of the springs are necessarily extended by equal amounts, if at all, in every landing impact so this approach has difficulty in accurately predicting the spring behavior. The need to identify which springs are engaged during the impact of the tensegrity structure motivates a further investigation of three unique landing orientations in the following chapters. For design purposes, the difference in cable lengths between the deployed (icosahedron) and undeployed (flattened) state can be used as an approximation of the spring forces needed to fully collapse the structure upon impact when landing in an orientation such as in Fig. 2.2. From the geometry of the flattened hexagon, the saddle and diagonal cables extend by approximately 20% of their original length, the top and bottom cables do not change, and the vertical cables go slack, meaning that the impact energy is equally distributed among those select twelve cables in this scenario.

## Spring Constants and Pretension

The overall effective stiffness of the tensegrity structure directly depends on the spring constants used in the cable elements. Stiffer springs will produce a more robust structure, but generally are much heavier. The additional impact energy therefore will remove any added benefit of the stiffer springs. Due to this tradeoff between spring designs, it is beneficial to also consider the spring's stiffness to mass ratio as a parameter that captures the overall effectiveness of the spring as an impact absorber. Choosing such a spring will optimize the cable performance as outlined in the above equations.

The sensor payload is suspended in the center of the structure and is connected by a set of twelve cables, one from each rod end cap to the nearest tangent point on the spherical payload. During impact, the payload motion within the internal volume of the tensegrity structure is constrained in all directions by these springs. As the primary motivation of the tensegrity structure is to protect its central payload, the spring constants for the internal payload cables must be chosen carefully. The tensegrity structure absorbs a large amount of the impact energy through its deformation and rebound, but at the instantaneous moment of impact the payload still has a downwards velocity. The effective spring constant of the combined payload cables must inhibit the payload motion and reduce the probability of it impacting the ground. Assuming that the payload is moving straight down the expression for the effective vertical spring constant of an angled spring can be used to find an overall lumped spring constant $k_P$ that governs the payload motion,

$$k_P = \sum_{i=1}^{n} k_i \cos^2(\theta_i) \tag{2.10}$$

where $k$ is the spring constant and $\theta$ is the angle measured from the vertical axis for each of the $n$ springs that are currently engaged (the extension springs underneath the payload, for example, will not contribute any forces during compression). The expected forces on the payload can be found from the desired deceleration characteristics and then used with $k_P$ to calculate the stopping distance the payload needs. This distance should be, at minimum, half the height of the tensegrity structure since the payload is suspended in the center. Generally, because the structure is also compressing under impact, the effective stopping distance is reduced and additional safety factors from the material choice and hardware designs will be needed.

For the spring pretension for all cables in the tensegrity structure, a higher pretension results in a stiffer structure but reduced energy capacity for absorbing impact energy in the springs. A stiff structure is particularly useful in resisting deformations from its static equilibrium state. In the design of tensegrity landers for impact there is a need to minimize mass, and therefore energy capacity, of the springs. Therefore it is desired to have high stiffness to mass ratio springs at a low pretension, in order to maximize the impact energy they can absorb. From the prestressability conditions of tensegrity structures, the pretension can be uniformly scaled across all cables without changing the overall shape. However, the structure will deform more upon impact, so care must be taken to ensure that the collisions between rods and the payload are not too severe.

The work in [48] explores the optimal pretension of a three-bar tensegrity prism to maximize its compressive stiffness. While the results may not scale directly to other topologies, they are helpful in identifying potential key cables for the six-bar structure: the six-bar structure has an aspect ratio (height to diameter) of 0.75 so it can be tentatively said that it is controlled by failure criterion (e.g. yield of rod or cable material) rather than stopping criterion (rod collision or locking). The work also classifies tensegrity structures with this aspect ratio as being dominated by horizontal pretension. It is indeed observed that in the compressive mode to flatten the structure discussed above, the saddle and diagonal springs are oriented close to the horizontal direction and are the primary support against loading in the compressive direction. Increasing the pretension in these cables will make the tensegrity more robust against such compressive loads.

## 2.3 Hardware Prototypes

The BEST Lab has developed multiple versions of a six-bar tensegrity robot for testing control and locomotion policies. The TT-3 mobile robot could locomote on flat terrain and also survive a drop of 2 m while carrying a small payload [25]. As previously stated, the goals of mobility and impact resilience are inherently opposed, since locomotion through cable actuation requires relatively low tensions in the cable elements to reduce motor loads and improve energy efficiency, while impact resilience generally requires higher pretensions to prevent excessive deformation of the structure during landings. Furthermore, the actuators and motors needed for locomotion control add weight that increases the impact force without providing any benefits to the impact response. For comparison, NASA's SUPERball v2 robot weighs 38 kg without its payload and has been tested at drop heights of 3.4 m [49]. Solutions to mitigate motor loads during impact such as cable brakes have been explored [50], but navigating the tradespace of impact resilience and motor locomotion remains very much an area of active research.

With the goal of redesigning for higher drops, the TT-$5_{meso}$ [51] was the lab's first prototype of a droppable tensegrity robot capable of carrying a larger payload, while maintaining mobility operations for a drop higher than 2 m (Fig. 2.3). It featured lightweight, hollow aluminum rods with plastic endcaps, a wooden payload box, and strain-stiffening latex tubing for the tensile elements. The latex properties would enable the low strains for locomotion without demanding excessive motor power and simultaneously resist large strain deformation and energy absorption during impact. However, while the design of TT-$5_{meso}$ made compromises in cable stiffness and rod strength to enable mobility, it was insufficiently robust to survive falls from over 5 m.

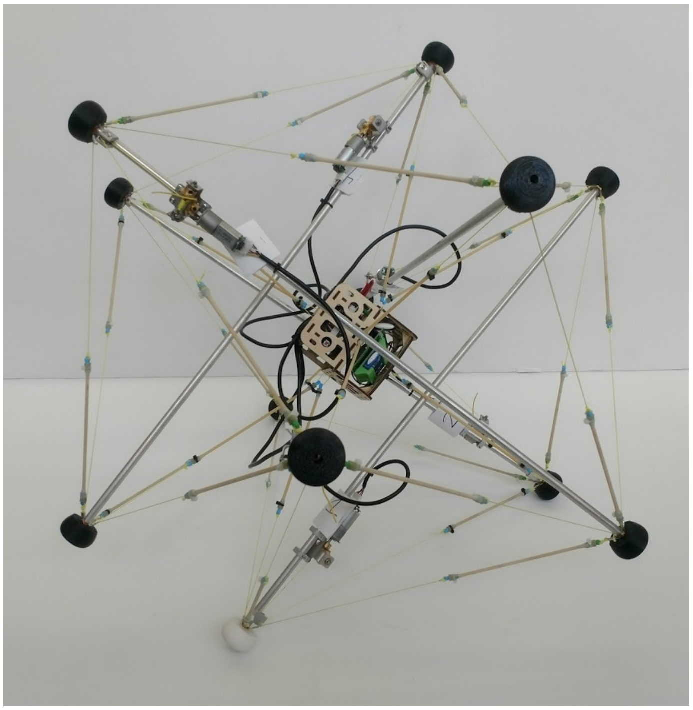

Figure 2.3: TT-$5_{meso}$ six-bar tensegrity prototype

The lab's next generation of tensegrity robots were developed in collaboration with its spin-off startup Squishy Robotics. Based on feedback from first responders, the tensegrity system was split into two platforms: 1) a stationary robot that can carry delicate sensors and other payloads from aerial vehicles, but with no ground locomotion capabilities, and 2) a mobile robot that could walk on rough terrain, but not currently capable of large drops. This strategy allowed the focus of the work to be on a better understanding the design trade space of an impact-resistant stationary tensegrity robot without considerations for ground mobility.

The stationary robot is based heavily on the experience of the TT-$5_{meso}$ experiments. Its design is meant to be a robust tensegrity for the purpose of providing impact protection for payloads. The design process for refining the impact-resistance of the structure was to form general engineering constraints from the design equations and then methodically tune the physical parameters through simulation, rapid prototyping, and physical testing.

Initial stationary system prototypes were based on TT-$5_{meso}$. They used carbon fiber rods for the main structure as a direct response to the need to simultaneously reduce mass and increase rigidity of the compressive elements. Cable connectors on the rod ends linked to a silicon rubber lattice with similar tensile properties to the strain-stiffening latex tubing of the TT-$5_{meso}$. These prototypes also had new designs in the form of a plastic capsule for the payload and neoprene foam as the impact absorbing endcaps to protect the rods and cables from damage. These first stationary system prototypes were able to readily survive drops from up to 10 m. The carbon fiber tubes showed promising behavior, but the payload, endcaps, and tensile rubber lattice required further investigation. Since the tensegrity structure mitigates the impact on the central payload without entirely preventing it from occasionally colliding with the rods or the ground during impact, the plastic payload could easily fracture from repeated drops. The foam endcaps were not able to protect the cable connector pieces on the rod ends, and the silicone rubber lattices used to maintain the tensile network suffered damage from the high strain rate over repeated tests. Overall, the system could undergo no more than five drops before failure.

Upon switching back to steel springs for the increased stiffness and damage resistance, subsequent prototypes demonstrated better impact performance but suffered from the spring end hooks deforming during impact. Noticeable damage and plastic deformation accumulated over time after approximately ten drops and could potentially lead to unreliable performance in the repeated landings and collisions the robot would expect to experience in a real product lifecycle.

Nevertheless, the design showed great potential and springs were continually used up to the most recent iteration of the stationary robot (Fig. 2.4). It has a heavily modified endcap design as well as carefully tuned spring constants for both the main six-bar tensegrity structure and the payload mounting connectors. It also features shorter rods made from carbon-fiber tubing to reduce weight and prevent premature buckling, soft thermoplastic polyurethane (TPU) endcaps to protect the rods and cable connections from impact damage, a flexible TPU payload shell, TPU rod sleeves to protect against collisions with the payload, and steel springs as linear elastic elements. Since the amount of shock that an object experiences during impact depends greatly upon the impact surface, material properties, and physical geometry, the TPU components were all designed with rotational symmetry based on their mounting points [52]. Namely, the component features include approximately hemispherical endcaps, a spherical payload shell, and uniform thickness rod sleeves to maintain a consistent level of robustness to impact from all potential loading directions. When the structure is able to control the randomness of its impact orientation, as seen later on in Chapter 5, future TPU components can be redesigned with additional features such as buffers or ribs that are specially tailored to provide cushioning and impact protection in primary loading directions.

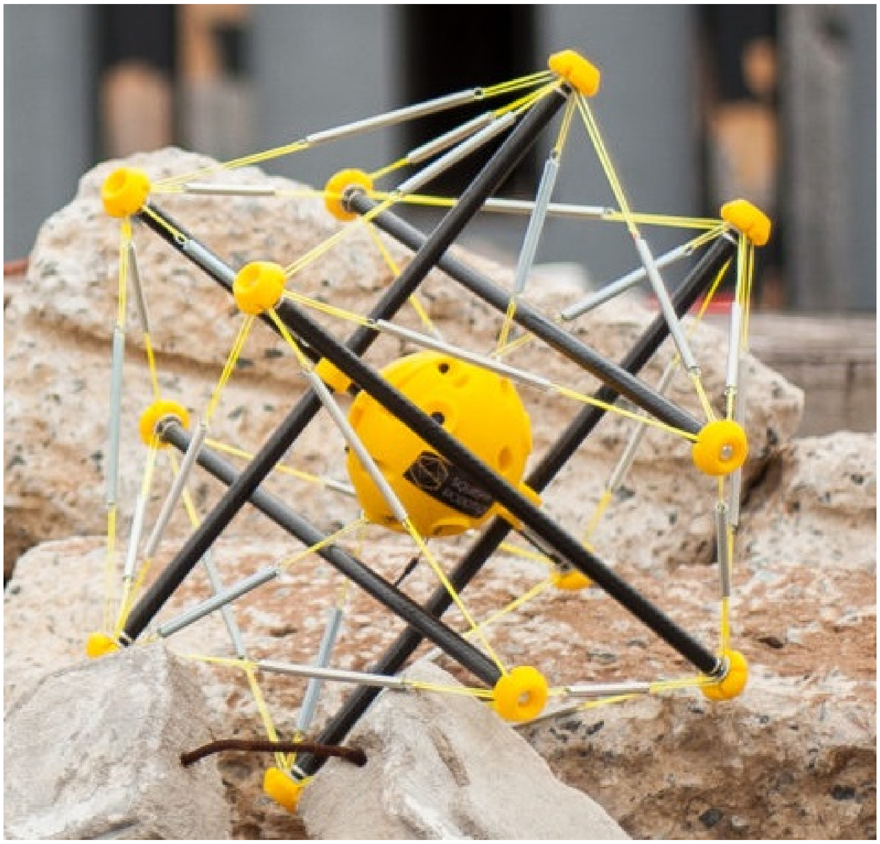

Figure 2.4: Squishy Robotics stationary robot in a simulated disaster environment

The impact-resilient properties of this stationary robot system have been maximized through multiple iterations over time. Overall, this design aims for a smaller, lighter, and stiffer structure in order to provide as much payload protection during impact as possible. Through a rigorous set of drop test experiments across multiple variations of hardware parameters, the measured peak payload acceleration is minimized while there have been notable improvements in the overall fatigue life (i.e., the number of randomly oriented drops that the structure can withstand before the onset of plastic spring deformation or rod damage). Finally, the material properties of the rods and cables used in the design calculations were further validated in experiment by National Testing Systems (NTS) (Fig. 2.5).

Figure 2.5: From left: Cable pull test setup, rod compression test setup, rod buckling after loading. Photos courtesy of NTS.

Rod compression tests determined the forces they could handle before failing, for comparison against the design equations. The samples were compressed at a rate of 0.04 in/min until buckling, at which the rate was increased to 0.20 in/min until the rod snapped. The rod reported a peak load of 1811.28 lbf, with a 703.51 lbf load and 0.710 in displacement at break (Fig. 2.6).

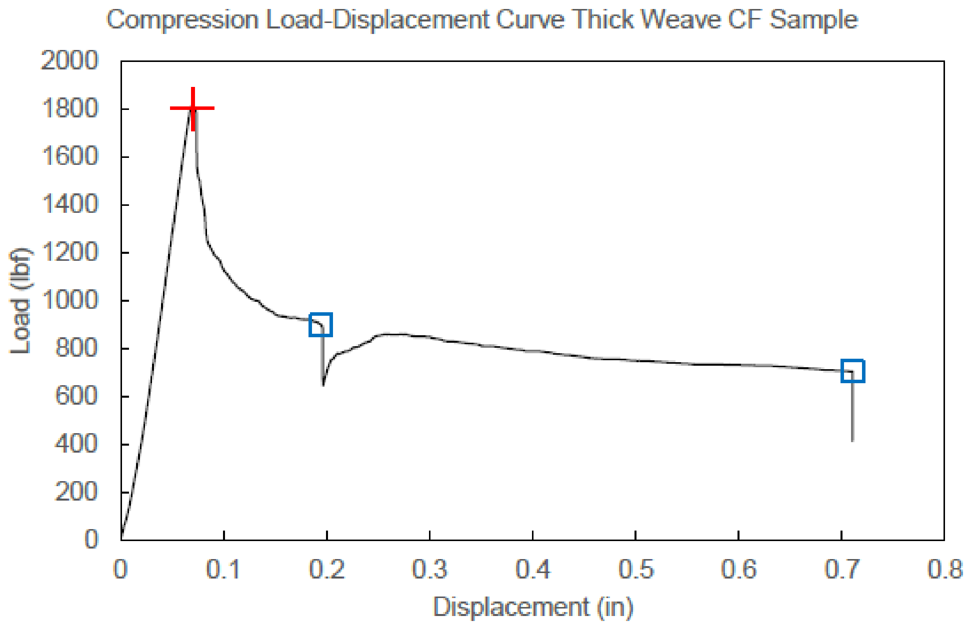

Figure 2.6: Compressive load curve for carbon fiber rod. Peak load noted by the red cross; break point noted by blue square. The first break had audible cracking of the rod but not complete snapping of the rod. Figure courtesy of NTS.

Cable tension tests determined the breaking point of the crimps holding the cable together. This value greatly exceeds the maximum spring force, so it is used as a maximum threshold of cable force in the event of spring failure. The cables were looped around 1/8" hooks and pulled at a rate of 0.5 in/min until failure (i.e., snapping of cable, removal from crimp, or any other result leading to a loss of bearing load). The cables reported an average maximum load of 78.87 lbf corresponding to a displacement of 1.629 in. at failure (Fig. 2.7).

The improved endcap and payload designs provide additional impact absorption, though the improved performance of the stationary system is primarily due to the reduced weight and increased stiffness. Compared to previous robots, the mass has been approximately reduced by half mostly due to the removal of motors and actuators, the rods shortened by one-third, and the stiffness increased almost two-fold (Table 2.1). Note that the stiffness parameter $k$ refers to the uniaxial tensile stiffness of the elastic elements when pulling the element along the cable direction, not an overall effective stiffness of the structure's deformation as a whole. The exterior elements form the main icosahedron structure, while the interior elements refer to the connections suspending the payload in the center of the structure. The twelve interior springs and central payload add a substantial amount of rigidity to the structure and play a critical role in impact protection. A previous iteration had $k = 520$ N/m springs for both the exterior and interior springs, and a substantial improvement was observed when the interior springs were switched to the new $k = 740$ N/m springs.

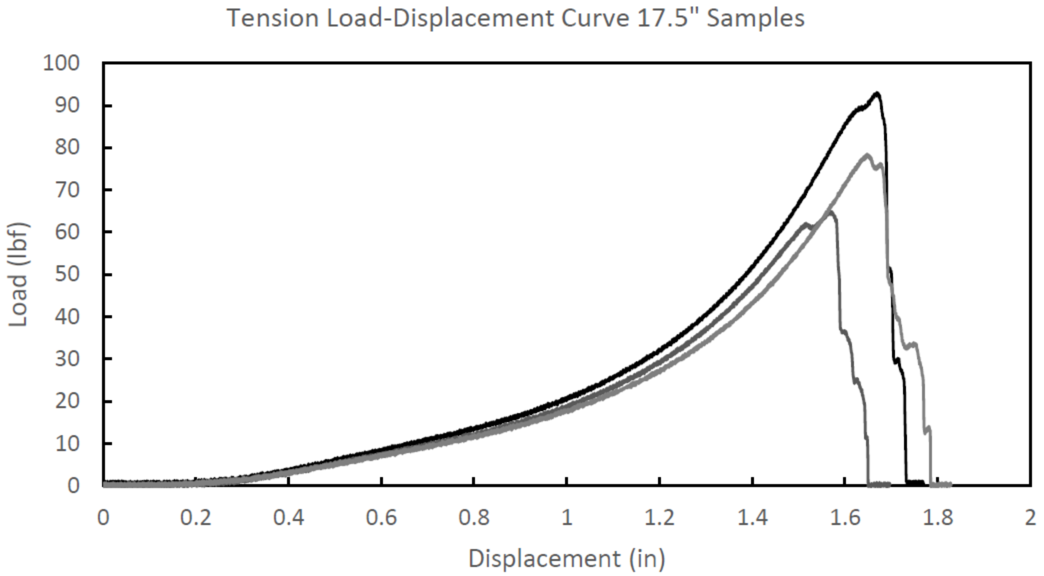

Figure 2.7: Tension-load displacement curve for crimped nylon cables. Figure courtesy of NTS.

| **Robot** | **Mass (kg)** | **Rod Length (cm)** | **Cable stiffness $k$ (N/m)** |
|---|---|---|---|
| TT-3 | 2.4 | 67 | 200 |
| TT-$5_{meso}$ | 1.7 | 72 | 271 |
| Stationary Robot | 1.1 | 47 | 520 (exterior)<br>740 (interior) |

Table 2.1: Comparison of six-bar tensegrity robot design parameters

Importantly, the design parameters such as rod length and spring stiffness can be tuned to accommodate a variety of third-party payload weights and configurations. For clarity on the different designs, the robots will also be henceforth be referred to by the diameter of the effective circumscribing bounding sphere for each tensegrity structure, with additional modifiers as necessary. The version presented in Table 2.1 is for the standard 22" HazMat Stationary Robot platform, although scaled versions will be explored in this work for a broad understanding of the deployability and impact performance of the system (Fig. 2.8 and Table 2.2). The scaled tensegrities give a concrete visualization of how the overall size of the sparse and lightweight structure scales with rod length. Such larger robots are able to add additional space to the payload's stopping distance, at a minimal increase in mass.

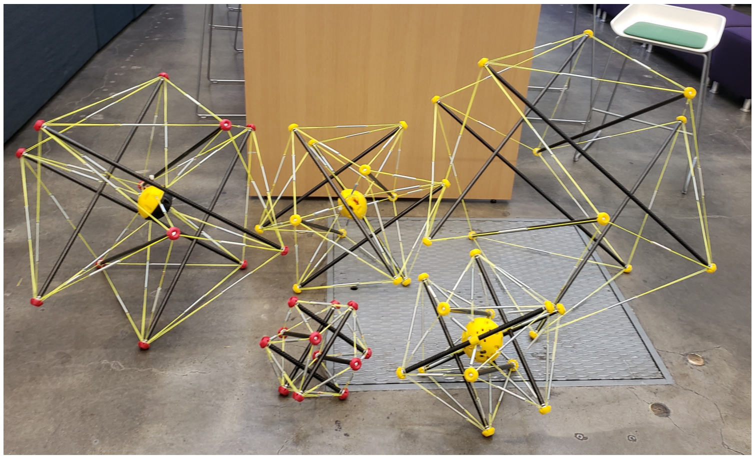

Figure 2.8: Tensegrity structures of multiple scales. From left: 38", 13", 30", 22", and 48" robots.

| **Robot** | **13"** | **22"** | **30"** | **38"** | **48"** |
|---|---|---|---|---|---|
| **Rod Length (cm)** | 28 | 47 | 66 | 84 | 102 |
| **Bounding Sphere Diameter (cm)** | 33 | 56 | 76 | 97 | 122 |
| **Mass Without Payload (kg)** | 0.647 | 0.784 | 0.875 | 0.920 | 1.010 |

Table 2.2: Overview of scaled tensegrity structure parameters

# Chapter 3

# Impact Modeling

## 3.1 Overview

As previously discussed in Chapter 1, prior work on simulating tensegrity robots during impacts from landing or hopping motions has often used ideal assumptions and simplified dynamics to parameterize the rods and cables. As a result, the simulations alone are not necessarily sufficient to understand the exact nature of the impact as they do not fully capture the dynamic behavior of the structures. Nevertheless, the simulation of tensegrity landers has proved invaluable in rapidly iterating through hardware parameters against design benchmarks, as well as providing key design insights on methods to improve the impact-resistance of the system. High-fidelity simulation tools can be used to rapidly test a large variety of parameterized tensegrity models to optimize design considerations in a considerably shorter amount of time than in hardware. Namely, valuable information on internal rod bending and compression stresses, cable tensions, and rigid body accelerations during short-duration high-load impacts can provide valuable insights on the overall geometries and components necessary for robust tensegrity topologies and designs.

In particular, numerous models for the buckling behavior of tensegrity rods during dynamic events have found that the ideal tensegrity assumption of uni-axial loading break down (i.e., the rods are not necessarily always in pure compression) [53, 54]. In fact, the rods are shown to absorb a greater portion of the kinetic energy than previously known through their elastic buckling and thus significantly contribute to the structure's capabilities in protecting the payload. This key finding provided a new theoretical design framework to design around the expected forces on the tensegrity rods, as shown in the previous chapter. It is sometimes beneficial for the analysis to consider the rods and cables of the tensegrity structure as discrete components of an overall system. During certain impact events, when the ideal tensegrity assumptions break down there is a loss of tension in the system and for an instantaneous moment each rod may only have a subset of its cables coupling its forces with its neighbors'. It is during these moments that the rod can be considered isolated in a worst case landing scenario with no way to dissipate its local forces into the global tensegrity network. Designing the rods to absorb energy through buckling modes accounts for such scenarios and improves the mass efficiency of the system.

Prior work in the BEST lab has utilized a variety of simulation packages to aid in rapid design and prototyping of tensegrity structures for many applications. One of the earliest simulation environments for testing and evaluating tensegrity robot locomotion and mobility is the open-source NASA Tensegrity Robotics Toolkit (NTRT). NTRT enables the rapid creation and simulation of tensegrity structures by presenting a C++ API that allows designers to assemble and control fundamental tensegrity components such as cables, rigid bodies, and actuators. Specifically, the simulation environment is intended for obstacle collision detection and real-time simulation. Unfortunately, the Bullet Physics Library which NTRT is built on primarily uses simplified rigid bodies which do not model the internal bending and tensile and compressive stresses very well. As a result, while NTRT can provide many valuable insights into locomotion, it is not well-suited for dynamic and transient impact analysis.

Unifying the modeling and simulation of tensegrity structures during impact with matching experimental results very much remains a major challenge in the field. Very recently published "quasi-static compression experiments and dynamic drop weight impact tests...[are] the first to experimentally corroborate theoretical studies of buckling tensegrity structures" [55]. In this study, the tensegrity structure was a twelve-bar truncated regular octahedron, chosen for its six square orthogonal faces to allow tessellation in 3D lattices to form a tensegrity metamaterial. Furthermore, the sample size of a unit cell was approximately 5 cm and it was loaded with forces of up to 20 N. Although the tensegrity topology is different from the six-bar tensegrity structure and the scale of impact forces and velocity are orders of magnitude lower, it serves to emphasize the tremendous difficulty in correctly aligning simulation models with experimental values for tensegrity impacts, and highlights a promising methodology to advance the research in the future.

## 3.2 Analytical Solutions

In analyzing the impact-resistance of the tensegrity lander, the primary metric of success is the peak acceleration experienced by the sensor payload suspended in the center of the structure (damage thresholds for impact tolerance are generally specified through peak accelerations and displacements in the literature rather than stresses and strains). While the other components of the hardware such as the rods and cables are allowed to experience unexpected failures from overloading in the worst case scenarios, the sensor pod itself is mission critical and cannot sustain any damage without compromising the operation of the tensegrity lander during deployment. It is important to establish damage boundaries for the impact tolerance of an electronics package, although the measurement process is often challenging [56]. Drop test models and simulation in the literature primarily focus on the protection of electronics at the board level, namely the evolution of stresses and strains in the solder joints or at layer interfaces of the circuit board [57]. However, there is limited literature analysis correlating drop tests at the board level with those at the product level, namely considering the interactions between the electronics, fasteners, and outer enclosure [58]. Notably, there is also a gap that exists in the study of repeated drops of electronics at the product level that this work will consider for the repeated drop test experiments of the tensegrity landers.

When considering the case of the tensegrity structure deployed in a high-altitude landing, the impact response of the sensor electronics in the payload are even further removed. If the TPU payload shell can be considered as the product level, then the tensegrity structure is one layer above that at a system level. This separation poses an even greater challenge than previously expected in mapping the tensegrity structure's impact to the forces experienced by the electronics. Before even considering the effects between the sensor board and the payload shell, the landing dynamics of the tensegrity structure are already complex, multibody, highly coupled, and nonlinear. Conventional equations of motion for a six-bar tensegrity structure involve eighteen generalized coordinates for kinematics, or twenty-four degrees of freedom for full control using cable dynamics. Furthermore, there is currently no way to reliably measure any of the individual cable behavior in real-time experiments. The complexity of a potential solution motivates a search for ways to simplify the analysis through models that can approximate the effective behavior of the structure during impact and simplify the equations of motion.

The impulse momentum model is a common and simple method to model impact using the conservation of momentum, but is limited in scope to rigid body collisions and does not consider the deformation of the bodies. They are better suited for collisions that involve small deformations and minimal contact times. On the other hand, contact models based on Hertzian contact theory allow for elastic deformation of interacting bodies but assume a perfectly elastic collision with no energy losses. For a flexible system such as the tensegrity structure, a potentially suitable candidate for impact modeling is the mass-spring-damper model that can combine elastic deformation and energy dissipation [59]. Consider the classical mass-spring-damper model of an object of mass $m$ contacting the ground through an interface of linear stiffness coefficient $k$ and damping constant $c$ (Fig. 3.1). Its oscillatory motion is parameterized by the directional coordinate $x$ in the equation of motion used to solve for the total force on the object. Assuming no other external forces are present, the equation of motion for the mass-spring-damper is given by

$$m\ddot{x} + c\dot{x} + kx = -mg \tag{3.1}$$

where $g$ is the gravitational acceleration in the negative $x$ direction.

The mass-spring-damper model is readily able to use the contact time of a collision $t_c$ and its coefficient of restitution $e$, two of the more easily measured parameters of an impact experiment, to derive $k$ and $c$ for a system. Stiffness and damping are not easily solved for, since they do not necessarily scale directly from the material properties especially under higher rates of loading. Indeed, a quasi-static compression test of the tensegrity structure presented below will report notably different effective stiffness values than those measured through impact experiment. Assuming that $k$ and $c$ are constant during impact and that

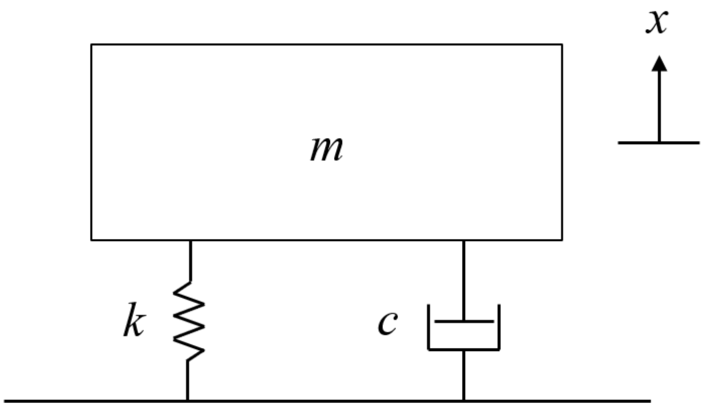

Figure 3.1: Mass-spring-damper model

the object has a low weight to stiffness ratio ($\frac{mg}{k} \ll 1$), then the equation of motion can be solved such as in [60] to provide closed-form expressions for stiffness and damping as a function of measured contact time and coefficient of restitution.

$$k = \frac{m}{t_c^2}(\pi^2 + (\ln e)^2) \tag{3.2}$$

$$c = -\frac{2m}{t_c} \ln e \tag{3.3}$$

The tensegrity landers are considered for three unique landing orientations during impact: closed face, open face, and double rod, i.e., when the robot landing is directly aligned with a vertical pair of parallel bars (Fig. 3.2). For additional clarity, the closed face and double rod landing orientations can also be seen in Fig. 2.2 and 2.1, respectively.

Since the impact orientation of the structure is inherently random and dependent on a variety of drop conditions, these three landing orientations are tested in order to capture a range of possible impact behaviors for the system. Qualitatively, the closed face orientation provides the most flexibility and energy absorption through structural deformation since that is the direction the structure is most readily compressed. The double rod orientation is the stiffest orientation in terms of structural deformation since the majority of the shock loading is imparted axially along the rods and there is little to no compression in this loading direction. Finally, the open face orientation is a balanced mix between the two behaviors since the rods are impacting at a near-vertical angle, but there is a slightly greater degree of compressibility in the structure.

Figure 3.2: Tensegrity structure with highlighted closed face (red), open face (blue) and double rod (green) landing orientations

The 22" tensegrity robots were tested in a series of controlled drops from 1.5 m for each landing orientation to characterize the model coefficients from measured data. Frame-by-frame analysis of camera video was used to calculate contact time $t_c$ and coefficient of restitution $e$ based on the structure position over time relative to a reference distance calibration included in the shot of the video. The theoretical force was then calculated by the mass-spring-damper model parameters using the structure's instantaneous deformation $x$ and velocity $\dot{x}$ at the moment of impact (Table 3.1). For comparison with the model, the the tensegrity structures were dropped on a force plate that recorded the impact force profile for each of the drop events (Fig. 3.3).

| **Parameter** | **Closed Face** | **Open Face** | **Double Rods** |
|---|---|---|---|
| $t_c$ **(s)** | 0.040 | 0.033 | 0.027 |
| $e$ | 0.56 | 0.50 | 0.57 |
| $k$ **(kN/m)** | 7.0 | 10.4 | 15.4 |
| $c$ **(N-s/m)** | 32.0 | 46.2 | 45.8 |
| **Impact Force (N)** | 360 | 508 | 524 |

Table 3.1: Mass-spring-damper model parameters and impact force calculations, 22" robot 1.5 m drop tests

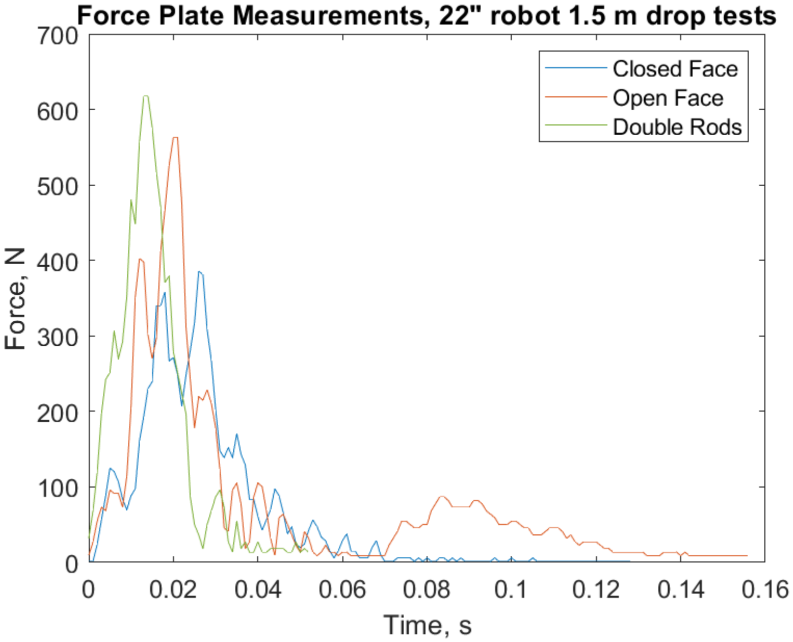

Figure 3.3: Representative impact force profiles, 22" robot 1.5 m drop tests

Inspecting the trends in the mass-spring-damper parameters and the impact force profiles verifies the qualitative behavior observed between the three primary impact orientations. Contact time of impact decreases from closed face, to open face, to double rods while the effective stiffness of the structure increases. The increase in peak force is also captured by the force plate, although there is only a slight difference between the open face and double rod orientations, perhaps due to the low impact velocity. The secondary impact in the open face force measurements is from the structure bouncing sideways on the force plate: in this landing configuration, the structure is resting at an offset angle and is prone to immediately rolling upon impact. This overall behavior of the landing configurations remains consistent over a significant number of tests and highlights the importance of considering orientation during impact experiments (Fig. 3.4).

For the closed face and open face orientations the impact force predicted by the mass-spring-damper model falls within the range of the force plate measurements. However, there is a model mismatch for the double rod landings where the force is underestimated compared to the experiments. In previous experiments to fit the mass-spring-damper model in the literature, higher stiffness values for the system resulted in greater discrepancies with experimental values, likely due to energy losses from vibration not being considered [61]. There may also have been limitations and measurement errors present in the experiment, especially with the video camera framerate capturing the motion of the tensegrity structure in discretized locations and potentially being slightly phase shifted in time away from the precise moment of impact. Nevertheless, the good level of agreement for the other two

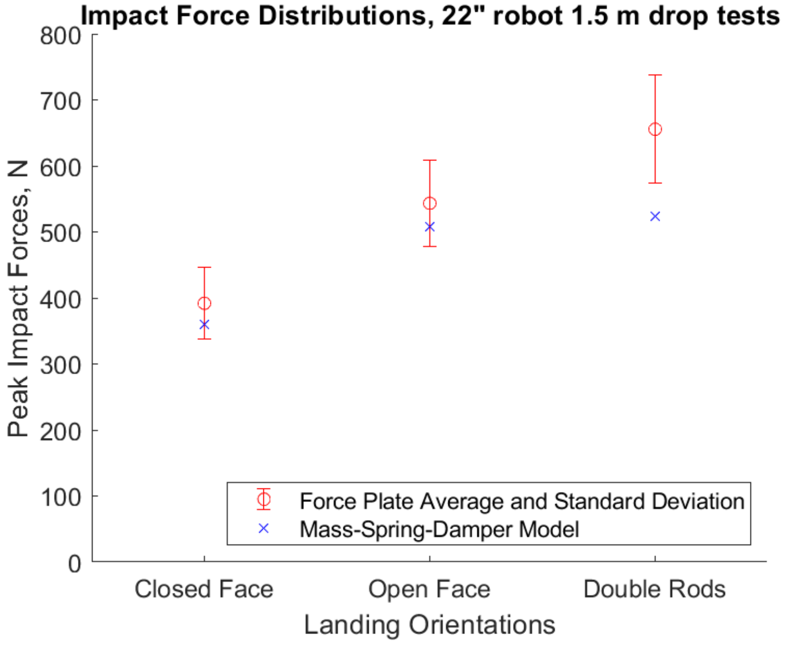

Figure 3.4: Drop test impact force distributions, 22" robot 1.5 m drop tests

orientations is more important since those are the primary landing modes the structure should aim to land on to minimize payload acceleration. The next chapters will provide a thorough quantitative justification for the optimal landing face and explore options to ensure that the tensegrity can land in this orientation.

While the mass-spring-damper model is useful in capturing the overall macroscopic behavior of the tensegrity structure during impact, it is dependent on landing orientation. However, further investigation is needed to verify if the model is able to still match the experimental values at higher impact velocities, but close up video data of the force plate impact for such drops was unable to be obtained, as discussed in the experimental design presented in the following chapter. Furthermore, the model is unable to assist in the design process and instead can only be used to fit against experimental data after time and energy has been invested in building and testing a new tensegrity prototype. If the model were to be used as a design tool, it would be necessary to map the physical hardware parameters of the structure, such as rod and spring stiffnesses, into the stiffness $k$ and damping $c$ of the mass-spring-damper model. At this time the relationship between the two is unclear especially under higher rates of loading. As previously mentioned, the model parameters do not scale directly from the hardware. A quasi-static compression test of the tensegrity structure reported a best fit curve of stiffness $k = 1.4$ kN/m, much lower than those found by the model parameters fit to measured drop test experiment values (Fig. 3.5). Note that the last data point in the force-deflection curve was omitted from the curve fitting because it corresponds to the tipping point of the structure during compression when it loses stiffness and begins to collapse under any externally applied load. These experimental findings further suggest that a mass-spring-damper model can capture the effective behavior of the tensegrity structure well, since it can account for the almost visco-elastic behavior of the deformation under various rates of loading.

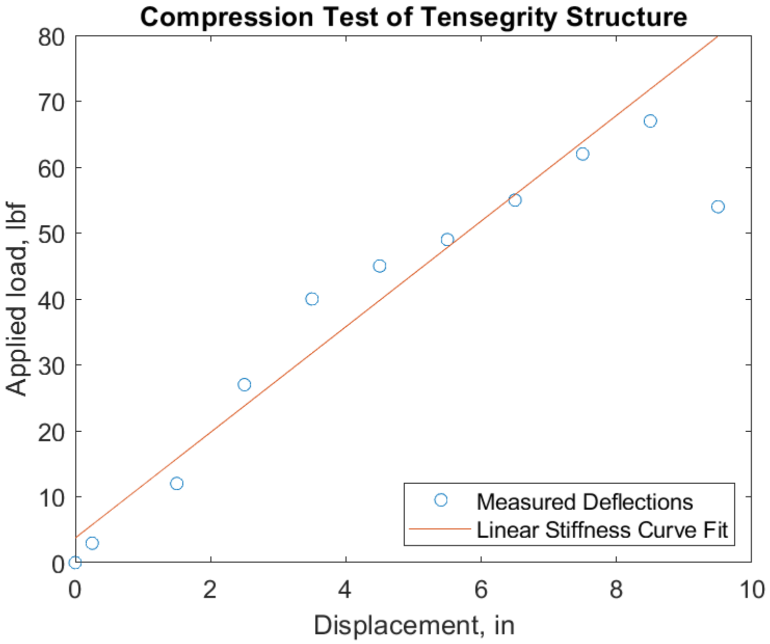

Figure 3.5: Compression test measurements of tensegrity structure in closed face orientation

## 3.3 Simulations

In addition to NTRT, MATLAB dynamics models have also been used to evaluate locomotion and actuation strategies for the tensegrity robots and utilize a simplified lumped mass representation. This lends itself better to rapid design and prototyping of locomotion strategies rather than in-depth stress analysis, but remains a valuable tool in approximating the behavior of the system. Many simulation models presented in the literature make use of mass lumping or similar simplifications in order to generate reduced-order models for the dynamics of the tensegrity. Of these simulation models, the lumped mass model remains one of the most common types for its relatively quick setup and moderately accurate results. It is presented especially well in [62], and is briefly summarized with additional considerations for the six-bar tensegrity structure below.

Consider a six-bar tensegrity structure represented by twelve lumped mass nodes (two per rod, located at the ends). The kinematics of each node in three-dimensional space can be represented by a set of three $3 \times 1$ vectors for position $\mathbf{n}_i$, velocity $\dot{\mathbf{n}}_i$, and acceleration $\ddot{\mathbf{n}}_i$, which can be appended into a corresponding set of three $36 \times 1$ vectors to parameterize the entire structure.

It is beneficial to first orient the structure such that the bars are aligned with the Cartesian coordinate axes, as seen previously in Fig. 2.1. This allows for the node coordinates to be readily located based on the tensegrity's design parameters (the values for the node positions will all be permutations of $0, \frac{L_r}{2}$, and $\frac{L_r}{4}$). Rotation matrices can then be applied to re-orient the structure into the desired landing position. To simulate a drop test the initial conditions must be set. The node positions can be offset by the desired $z$-height, and the initial velocity vector can have a nonzero $z$-component or even have randomized linear and rotational velocity components for a truly unpredictable impact.

The nodal accelerations are solved using

$$\ddot{\mathbf{n}} = \mathbf{M}^{-1}(\mathbf{f}_E - \mathbf{f}_I) \tag{3.4}$$

where $\mathbf{M}$ is the lumped mass matrix and $\mathbf{f}_E$ and $\mathbf{f}_I$ are the external and internal forces on the system, respectively. The lumped mass matrix assumes that the mass of the rods and cables are evenly split between their two respective end nodes. Given a $24 \times 1$ vector of string masses $\mathbf{m}_s$ and a $6 \times 1$ vector of bar masses $\mathbf{m}_b$, the lumped mass matrix $\mathbf{M}$ is defined as

$$\mathbf{M} = \hat{\mathbf{m}} \otimes \mathbf{I}_3 \tag{3.5}$$

where $\hat{\mathbf{m}}$ is the diagonal matrix formed from the node mass vector $\mathbf{m}$:

$$\mathbf{m} = \frac{1}{2}|\mathbf{C}_s^\top|\mathbf{m}_s + \frac{1}{2}|\mathbf{C}_b^\top|\mathbf{m}_b \tag{3.6}$$

$\mathbf{C}_s$ and $\mathbf{C}_b$ are the string and bar connectivity matrices commonly used in the literature to succinctly define the members of a tensegrity structure and map the individual nodes into bars and cables. The string connectivity matrix is $24 \times 12$, with rows representing the strings and the columns representing the nodes, while similarly the bar connectivity matrix is $6 \times 12$. The entries for a single row of either connectivity matrix indicate which nodes form the string or bar in question. In this row, the column values are 1 at the start node column index, $-1$ at the end node column index, and zero elsewhere. For example, if the nodes of the tensegrity are numbered by the designer such that Bar 4 is formed by Nodes 7 and 8, then the fourth row of the bar connectivity matrix is a $1 \times 12$ zero vector with a 1 as the 7th entry and a $-1$ as the 8th entry.

$\mathbf{f}_E$ encapsulates the external effects of gravitational acceleration, ground reaction, and friction. External forces on each node can be calculated using conditional switch conditions that check if the node is in contact and moving relative to the ground, and calculating the relevant forces using first principles. Then, the nodal vectors can be assembled into the global external force vector necessary for the kinematic solution. The internal force $\mathbf{f}_I$ is given by

$$\mathbf{f}_I = (\mathbf{C}_s^\top \otimes \mathbf{I}_3)\mathbf{f}_s + (\mathbf{C}_b^\top \otimes \mathbf{I}_3)\mathbf{f}_b \tag{3.7}$$

where $\mathbf{f}_s$ and $\mathbf{f}_b$ are the string and bar forces found by calculating stress and strain parameters using $\mathbf{n}$, $\dot{\mathbf{n}}$, and the given material properties. Finally, solving $\ddot{\mathbf{n}}$ gives the complete kinematic information of the nodes at the current time. A time-stepping method of choice can then be used to march the simulation forward and repeat the solution process for the next timestep. The MATLAB lumped mass model was used in a similar manner as the high-level first-pass design equations presented in Chapter 2, namely to give enough confidence that critical design thresholds were not overly exceeded during impact. However, they were not able to accurately predict the peak impact accelerations across a rigorous array of drop test experimental conditions.

Improving the accuracy of drop test simulation models inherently comes at a tradeoff of complexity and computational cost. Even a minor modification to the geometry of the simulated parts can result in drastic differences in the impact response [63]. Nevertheless, a new simulation and testing framework using ANSYS Explicit Dynamics STR was collaboratively built by the BEST Lab. The ANSYS 15.0 LS-DYNA software focuses on the structure of the test model, including internal force and bending moments. Its core competency lies in highly nonlinear transient dynamic finite element analysis (FEA) using explicit time integration. Thus, it is highly suitable to simulate the tensegrity structures, modeled with explicit 3D beam units and catenary units as rods and cables. Therefore, LS-DYNA is a better impact simulation package choice for tensegrity drop test simulations compared to NTRT and MATLAB. Fundamentally, the FEA model also approximates the tensegrity structure with simplified geometries, but in a more complex manner than the lumped mass model to capture the nuances of the dynamic behavior of the system.

The ANSYS 15.0 LS-DYNA Module is used to simulate the tensegrity structures under different impact conditions. The simulation uses explicit 3-D beam elements (BEAM161) for the rods, tension-only cables (LINK167) for the springs, and 3-D structural solids (SOLID164) for the TPU endcaps and payload (Fig. 3.6). The endcap and payload geometry is reduced to shape primitives with lumped mass approximations to represent the nuts, bolts, and washers inside. Furthermore, the rods and cables have their endpoints set at the center of each endcap, the friction between components is assumed to be negligible, and other simulation parameters are set to match the physical properties of the 22" stationary robot (Table 3.2).

In addition to the structural properties, the necessary constants and variables also include motion conditions and gravitational acceleration. Given a drop height and zero initial velocity, the robot is simulated during free-fall and its impact response when it lands is measured and recorded. The simulation results include the internal force, velocity, and acceleration of each element. A primary metric of success is the acceleration experienced by the payload, which measures how well it is protected by the structure during impact. A detailed discussion of the drop test methodology, data collection, and metrics will be presented in the following

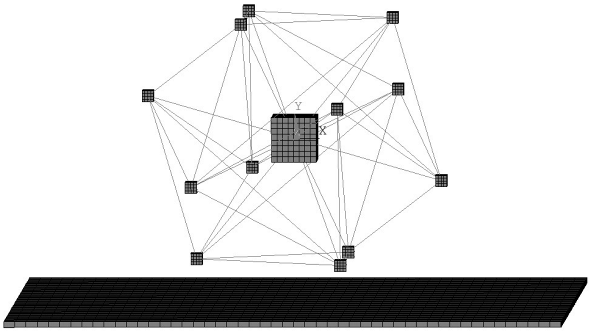

Figure 3.6: ANSYS simulation model of the stationary robot tensegrity structure, credit to Hao Hong

| **Parameter** | **Rods** | **Cables** |
|---|---|---|
| **Length (cm)** | 47 | 27 |
| **Young's Modulus (GPa)** | 134 | 2.03 |
| **Density (kg/m$^3$)** | 1500 | 300 |
| **Outer Diameter (cm)** | 1.45 (0.57 inch) | 0.08 |
| **Inner Diameter (cm)** | 1.27 (0.50 inch) | N/A |

Table 3.2: Simulation parameters for stationary robot tensegrity structure

chapter. Furthermore, the internal rod bending, compressive stresses and spring tensions can also be provided by the simulation model to compare with the estimates of the design equations. The carbon fiber rods are safe from bending and compressive failure, and the primary failure mode of the robot is generally accumulated damage of the springs over time. Simulation results for a 20 m drop predict that the peak spring tensions are approximately 100 N, two times above the normal limit of the initial springs in use. This situation would cause specific failure for the springs through plastic deformation, and the springs show the same result from the experimental tests. Improving the spring stiffness during the iterative hardware design process reduced the magnitude of the spring deformation and more than doubled the drop cycle fatigue life of the structures in the current version of the stationary robot.

The simulated motion of the structure during an impact has several key moments given as a series of timeframes of the simulation. The time lapse represents the ideal landing behavior of the structure when impacting on a closed face, with no random rotations during free-fall that result in unpredictable bouncing upon impact. After the initial landing (Fig. 3.7A), it deforms upon impact and begins to compress towards the ground (Fig. 3.7B). At its lowest point during the structural deformation, the payload contacts the ground slightly

(Fig. 3.7C) before the structure begins bouncing back to its equilibrium state (Fig. 3.7D).

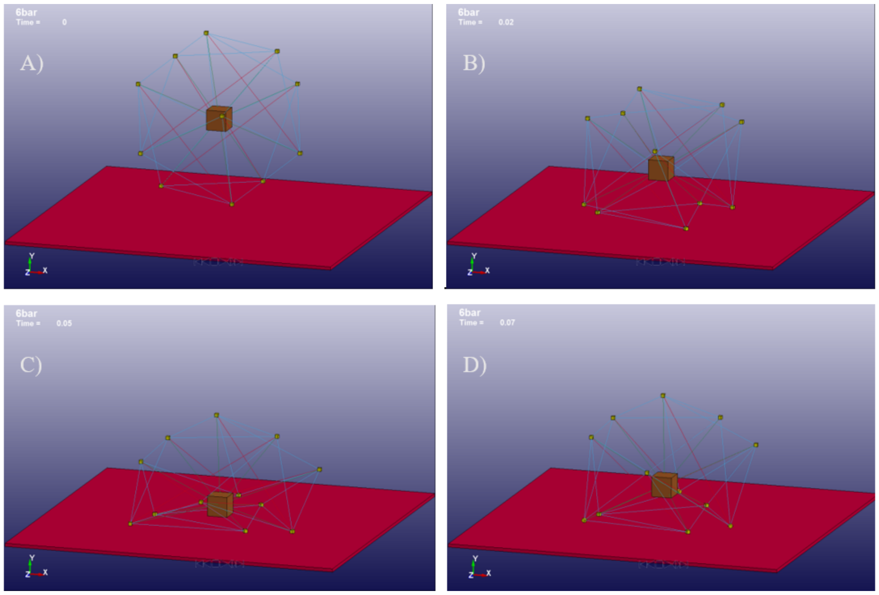

Figure 3.7: Impact motion of tensegrity structure for a 20 m drop in simulation model, credit to Hao Hong

From the preliminary experiments of drop tests of the 22" robot at drop heights of up to 20 m, the payload appears well protected with the maximum impact acceleration that occurs during the initial impact remaining below 250 g (Fig. 3.8). In comparison, during the TT-$5_{meso}$ drop test experiments the structure had its payload impact the ground and experience over 200 g for a fall from only 10 m, again indicating improved payload protection of the new structure. As previously mentioned, a detailed discussion of the drop test methodology, data collection, and metrics will be presented in the following chapter. The first round of low-altitude drop tests are primarily used to gauge the effectiveness of the simulation models as a design tool before rigorously iterating and testing tensegrity robot prototypes with increased impact capabilities.

Sample results are plotted together to evaluate the overall fit. Comparing the simulation results to the experimental data, it is apparent that there are certain discrepancies between the two. The simulation underestimates peak acceleration for lower drop heights (parameterized by the impact velocities) but then sharply increases to overestimate the peak acceleration at higher drops. The difference is likely due to the non-ideal landing conditions in experiment. The robot is consistently dropped such that it will land on a closed face of the structure. In simulation, the deformation of the structure in this ideal landing orientation prevents the payload from colliding with the rods or the ground for drops below 15 m. However, the landing orientation during experimentation is not fully controllable since minor variations in the initial conditions will lead to a wide variety of impact behavior. The

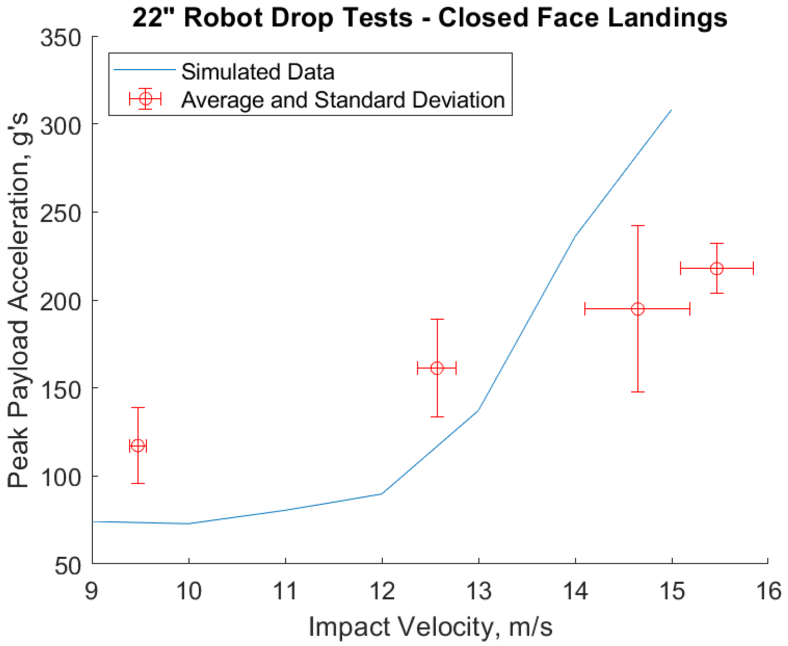

Figure 3.8: Comparison of 22" robot ANSYS simulation to averaged clusters of drop test experiment data

three rods of the closed face are not uniformly contacting the ground so the payload occasionally comes into contact with the rods or the ground for 5 m or 10 m drops, resulting in higher accelerations than in simulation. For 15 or 20 m drop simulations the impact forces are high enough for the payload to make contact with the ground, and the drastic increase in peak accelerations during element-on-element contact might be attributed to instabilities in the simulation timestep, hourglass control, or approximations in the material model of variable-infill 3D-printed TPU.

Nevertheless, data from selected drop tests indicate a strong potential for the simulation model to align with experiment (Fig. 3.9). The peak payload acceleration shown from the experimental data (blue line) maps to that of the simulation (red dotted line), and the two values are virtually identical. The two plots have been normalized in time to align the peak payload accelerations as a frame of reference. The smaller subsequent oscillations as the structure settles back into a static state for both the experimental and simulated data will vary depending on a number of random factors such as the ground conditions and the tensegrity impact orientation, but the overall qualitative behavior is relatively consistent.

Since the Stationary Robots are intended to deploy from an aerial vehicle at heights of 20 m or more, these comparisons demonstrate that the ANSYS 15.0 LS-DYNA simulation platform can provide an effective upper bound for maximum payload accelerations during impact. Overall it is a reasonably accurate simulation environment for the tensegrity drops

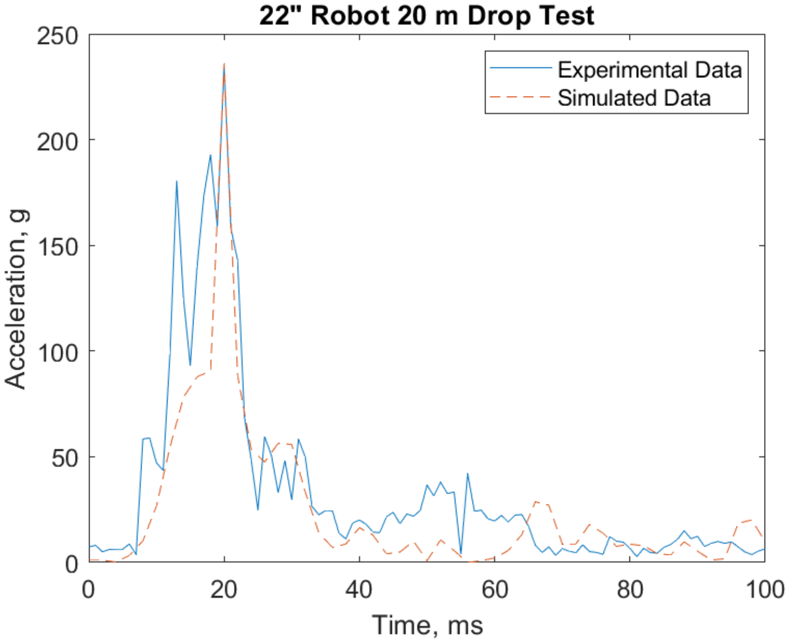

Figure 3.9: 22" robot 20 m drop test data comparison. Timescale normalized to align peak payload accelerations.

in a real mission scenario. It can rapidly provide valuable information of repeated drop tests by seamlessly changing simulation parameters. Designing the tensegrity to have safe limits at this theoretical upper bound can contribute to the optimization of tensegrity designs before beginning initial prototyping and experimental validation to provide tremendous cost savings in the deployment of tensegrity landers.

# Chapter 4

# Drop Test Experiments

## 4.1 Experimental Design

Drop test experiments were performed both to assess impact robustness of the tensegrity lander designs as well as to further investigate the unique behavior of the three characteristic landing orientations for the six-bar tensegrity structure [64]. In a similar workflow to drop test experiments in the literature [65, 66], the test system was equipped with impact sensors and camera video capture of the impact event was recorded. The sensors were placed inside the payload to directly measure the impact on the most critical component of the real system (Fig. 4.1). Two onboard accelerometers (an ADXL377 and an H3LIS331DL) monitored impact acceleration data and were recorded at 1000 Hz. A BME280 barometer and pressure sensor recorded data at 60 Hz and could be used to estimate falling velocity for sufficiently high drops. A BNO055 inertial measurement unit (IMU) logged an array of sensor fusion data, including robot orientation, at 60 Hz. Video capture of the landing was used to verify impact velocity and orientation for each test. Finally, all of the tensegrity landers were qualitatively assessed through a post-impact damage inspection for the onset of failure inside the hardware components.

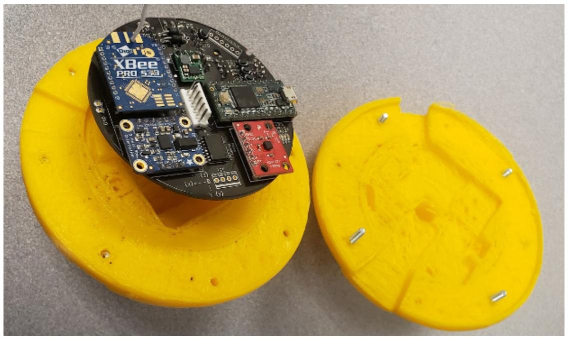

Figure 4.1: Tensegrity lander drop test experiment sensor pod, opened to show electronics

The tensegrity robots were evaluated in a variety of drop test experiment scenarios. Each type of test had its own set of unique advantages and disadvantages that, when combined, allowed for a holistic understanding of the tensegrity landers' performance in the context of a real mission scenario.

Low-altitude drops of up to 22 m from the Etcheverry Hall balcony on the UC Berkeley campus were used for rapid tests at discretized height intervals of approximately 5 m (Fig. 4.2). This maximum possible drop height was enough to obtain landing velocities that were adequately close (within 10-15%) to terminal velocity. Due to the controlled drop zone it was possible to obtain close-up videos of the impact events. Additionally, the drop zone was relatively well-shielded from cross-winds so landing orientation could be preserved as much as possible, based on the drop orientation of the tensegrity just before release. However, many drop test experiments often suffer from a randomness in the landing orientation that is caused by minor changes in the initial conditions of the system's exact position and orientation before drop [67]. Nevertheless, sensor data and detailed video capture of the impact were used to verify the correct landing within a vicinity of the target landing orientation. The large volume of drop tests sought to capture a statistical distribution of impact data that could be used to account for the randomness of the landing that would be seen in a real deployment scenario outside of a controlled laboratory environment.

To address the growing concern for potential injury in the event of a tensegrity lander impacting a human within a disaster area, the low-altitude drop tests were also used to measure the range of impact forces produced by the ground collision. A LoadStar IMF-RAP3-750M-10KHz-XL force plate with a 7342 N (1650 lbf) capacity logged data at a rate of up to 10 kHz (Fig. 4.3).

Figure 4.2: Timelapse images of tensegrity lander drop test from Etcheverry Hall balcony

Due to the limited contact area of the force plate, such experiments were limited to low-altitude drops where the landing area could be more accurately contained. A plywood board was attached to the plate to expand the impact area for ease of use even in this controlled environment. The measurements were then recalibrated to account for the additional moments measured at the farthest extents of the board. 10% ballistics gel was considered as a material to simulate the human torso and the force plate would measure a proxy force on the skeleton, since ballistics gel replicates flesh well but does not account for bones and other parts of the human body. The results could be compared with known blunt ballistic force corridors [68, 69], but the literature focuses primarily on small projectile impact and the use of ballistics gel as a model for tensegrity lander impact might be limited. On the other hand, stricter and more critical safety thresholds exist for the human head and the collision with the rigid force plate can be used as a direct model for the impact with a human skull, following the methods in [2, 70]. In particular, using the reference to the United States Federal Motor Vehicle Safety Standards gives Head Injury Criterion that are extremely accurate for narrow range of impact durations [71]. For example, the skull fracture criteria, nominally 5500 N at 124 g, has greater accuracy at lower impact durations. A lower value of 3100 N is given for neck shear, but there is no reference acceleration limit provided. In general, high impact forces can only be sustained over short periods of time, and conversely if the impact window widens the allowable force in this time must decrease. The force plate drop test experiments will characterize the tensegrity landers' impact forces within this space and evaluate its safety when dropped in a human-populated area.

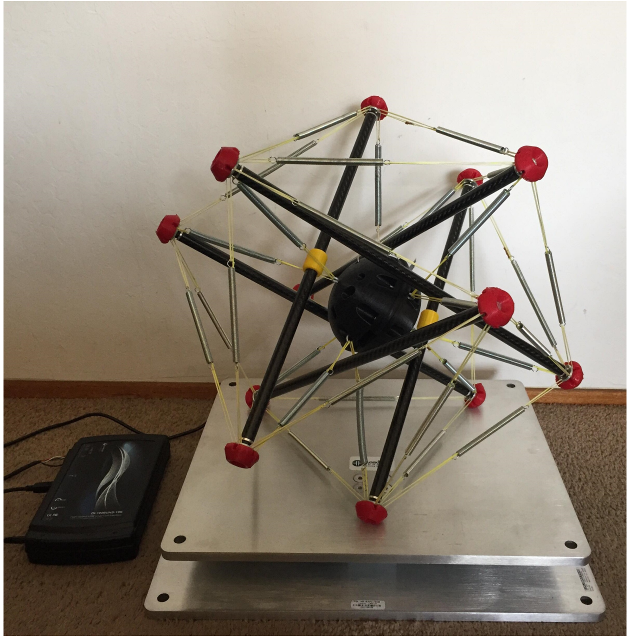

Figure 4.3: Tensegrity lander force plate experiment setup

Moderate-altitude drops of up to 122 m (400 ft, the highest drop legally allowed from a drone due to FAA regulations) from a DJI Matrice 600 drone were used primarily to simulate a real deployment scenario for the tensegrity sensor platforms (Fig. 4.4). The drone was augmented with a cable release mechanism that was used to deploy the robot automatically. The additional drop height was useful in producing true terminal velocity landings, although the tests had a significantly slower turnaround time compared to the low-altitude tests. Furthermore, it proved logistically impossible to control the landing orientation and obtain close-up video footage of substantial drops of over 50 m from the drone due to drone flight safety regulations and the inability to precisely target drop locations due to conditions such as prevailing wind.

Figure 4.4: Drone drop test of tensegrity lander

Finally, high-altitude drops of 183 m (600 ft) from a helicopter as well as drops of over 305 m (1000 ft) from a Short SC.7 Skyvan fixed-wing aircraft were used to simulate long-range deployment scenarios that the smaller drone flight ranges would not be able to achieve (Fig. 4.5). Larger tensegrity structures that would not fit underneath the drone's cable release mechanism could be drop tested in this manner. The longer drop times enabled the tests to capture the overall drift behavior of the landers in the presence of cross-winds and evaluate the performance limits of the sensors and wireless communication protocol. However, it had the same limitations of drone drop tests in that the drop zone could not be reliably controlled and video capture of the impact could not be obtained due to safety concerns. Nevertheless, these are the highest altitude drop tests performed on a tensegrity structure to date and serve to emphasize the innovative uses of tensegrity structures for payload protection.

Figure 4.5: Tensegrity landers in plane cargo hold in preparation for high-altitude drop tests

## 4.2 Results

The drop test experiment results of the tensegrity lander prototypes indicate the impact protection provided to the sensor payload by the external tensegrity structure. The accelerometer readings from all experiments compare favorably against reference drop tests of a standalone payload without a tensegrity structure (Table 4.1). All tests remained within the 500 g safety threshold required during deployment for the payload electronics to survive the landing impact [56]. The single payload is expected to exceed this limit at drops past 10 m, while the tensegrity structures are able to protect the sensors during high-altitude drops where the landers reach terminal velocity.

| **Drop Height** | **Impact Velocity (m/s)** | **Average Peak Acceleration (g)** |
|---|---|---|
| 1 | 4.30 | 121 |
| 5 | 9.79 | 392 |

Table 4.1: Drop test experiment results for single sensor payload without tensegrity structure

Each different size of the scaled tensegrity landers will first be discussed individually in the following subsections, before aggregating the results and discussing the overall trends between hardware design parameters and the impact response. Note that the 13" and 48" structures were not rigorously tested in experiment, but they were useful in providing design insights into mass and size scaling for alternative tensegrity structures. The internal volume of the 13" was relatively small compared to the drop test sensor payload, raising concerns that the payload would be guaranteed to collide with the rods even at low impact velocities and provide biased experimental data. However, it may still be considered for delivery of small, critical payloads in certain scenarios in the future where the small structure can be advantageous, such as emergency medicine being delivered by a small, fast, and lightweight drone-tensegrity system. On the other size limit, the 48" structure was deemed too large to be effectively carried by the drone for any type of moderate-altitude drops and took up a disproportionate amount of valuable plane cargo space for the high-altitude drops. Even for low-altitude drops, the large structure was unwieldly and difficult to move efficiently through the Etcheverry Hall balcony doorways, so only a few tests were performed to characterize the effects of increasing the spherical radius. As future designs of tensegrity landers introduce options to increase packing and transportation efficiency of larger-scale structures, different variations of the 48" structure will be tested to provide the necessary data in this unexplored region of design parameters.

## 22 Inch Robot

Multiple types of the 22" robot were developed to address various needs across mission scenarios (Table 4.2). Across all robot designs, the main hardware parameters that were tuned were the bounding radius, payload mass, interior and exterior spring stiffness, as well as any special design modifications for additional functionality.

| **Robot Number** | **Description** | **Mass (kg)** | **Int/Ext Spring (N/m)** |
|---|---|---|---|
| 22-1 | Standard | 1.103 | 740/520 |
| 22-2 | Heavier Payload | 1.253 | 740/520 |
| 22-3 | Asymmetric 1 | 1.271 | 740/520 |
| 22-4 | Asymmetric 2 | 1.439 | 740/520 |
| 22-5 | Stiffer Asymm 2 | 2.066 | 1320/1150 |
| 22-6 | Stiffer Asymm 2 | 1.441 | 1030/520 |
| 22-7 | Asymmetric 3 | 1.607 | 740/520 |
| 22-8 | Rod Asymm 2 | 1.343 | 1320/520 |
| 22-9 | Rod Int Spring | 1.240 | 740/520 |

Table 4.2: Outline of 22" robot design parameters

Starting from the base design of the stationary robot platform, labeled as 22-1, the payload mass was increased to test the carrying capacity of the tensegrity lander in 22-2. Types 22-3 through 22-8 were iterative designs of an asymmetrically-weighted robot that was able to control its impact and final resting orientation during a drop event. These designs will be discussed in greater detail in the following chapter. Finally, type 22-9 introduced a new payload cable routing system to mitigate payload motion during the double rod impact orientation. While the design was successful in greatly reducing the peak payload acceleration, the assembly process was overly complex and did not easily allow for removal of the payload for rapid replacement during user operation. Greater emphasis was placed on the reorientation control which could serve dual functions in both mitigating impact by avoiding the double rod landing as well as providing guaranteed positioning of orientation-dependent sensor payloads.

Based on accelerometer readings from the central payload and velocity data from video capture for the low altitude drop tests (Table 4.3), the initial characterization of the standard stationary robot (22-1) compares favorably against the data from previous generations.

| **Drop Height** | **Average Impact Velocity (m/s)** | **Average Peak Payload Acceleration (g)** |
|---|---|---|
| 5 | 9.16 | 116 |
| 10 | 11.8 | 155 |
| 20 | 14.3 | 235 |

Table 4.3: Low-altitude drop test results for 22" standard Squishy Robotics stationary robot

Notably, the 10 m drop of the 22" robot had a very similar impact velocity with the 10 m drop of the TT-$5_{meso}$ which impacted at 11.7 m/s and resulted in substantial failures. This clearly demonstrated the improved structural integrity provided by the new hardware design. While previous iterations of the robot leading up to the 22-1 design will not be discussed for brevity, it is worth noting several interesting observations that were made during the iterative design process. First, the twelve interior springs and central payload add a substantial amount of rigidity to the structure and play a critical role in impact protection. A previous version of the structure had $k = 520$ N/m springs for both the interior and exterior springs, and a substantial improvement was measured when the interior springs were switched to the current stiffer $k = 740$ N/m springs. Compared to other elastic materials such as silicone rubber or latex elastomers, the stiffer interior elements significantly reduce the severity with which the payload will collide with the rods or the ground during high-speed impacts. Furthermore, increasing the spring stiffness on all cables resulted in fewer failures through spring deformation. Though it is still common for springs to deform slightly after each drop, the amount of plastic strain was within the scope of the design equations and much lower compared to previous iterations, effectively doubling the operational life of the tensegrity structure to approximately twenty drops before requiring replacement springs. Overall, the new stationary system prototype (22-1) performed much better in the drop tests than the previous generations of the robot due to the lighter weight, stronger carbon fiber tubes, stiffer springs, and more robust endcap, cable connector, and payload capsule designs. At higher drop heights, there are far fewer catastrophic failures involving the cables or endcaps breaking, and the payload itself is well-protected from any direct impact with the ground. Other iterations of the 22" structure discussed in this section were designed using this type of robot as a ground baseline to further explore the impact limits of the structure.

As the tensegrity landers were first being considered for emergency response deployment in unknown environments, it became imperative to quantify the risks for human injury in the event that a lander impacted a victim within the disaster area. Low-altitude tests of the 22" robot in random orientations gathered a range of impact data from the force plate measurement system and indicated that the robot does not have enough impact force to cause severe injuries such as skull fracture or neck shear (Fig. 4.6).

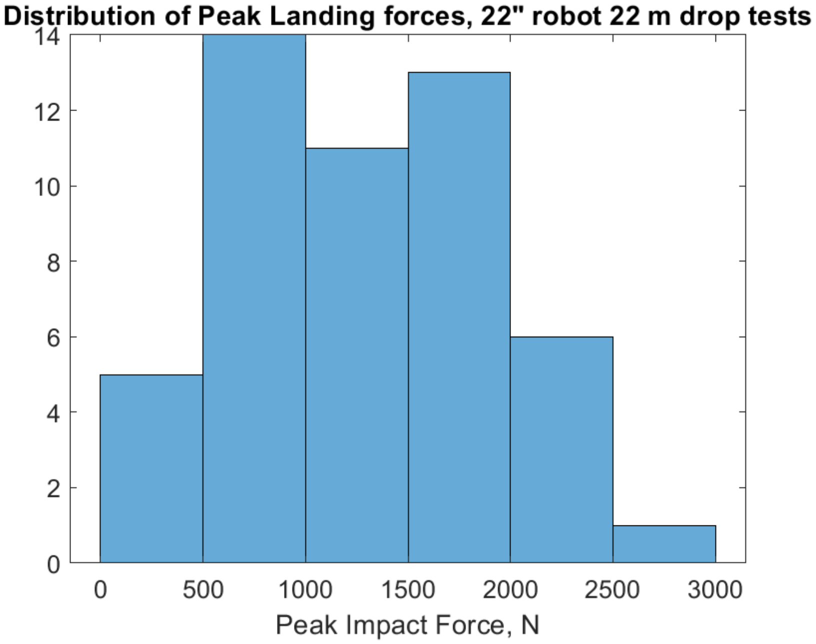

Figure 4.6: Impact force distribution for low-altitude drop tests of 22" robot

The impact forces are safe from the critical threshold for skull fracture, 5500 N, but come close to exceeding the limits for neck shear, 3100 N. The impact must also consider the peak acceleration, and the human limits are given in the literature as 124 g at short duration impacts from car crashes, which are typically on the order of 100-200 ms. In the realm of evaluating human safety factors for impact, it is critical to consider both peak acceleration and the duration of impact. Generally, high loads can only be sustained over short durations, while a constant load over time must be controlled to have a much smaller peak value. In the case of the tensegrity lander, the impact of the 22" robot has both a lower load and a shorter duration and so they theoretically will not cause levels of injury such as skull fracture. Due to the nature of the experimental setup, larger radius robots are not able to be tested for impact force measurements. Furthermore, heavier payload masses would naturally scale the impact force higher and risk the onset of neck shear, but this can be avoided by recognizing the different use cases of tensegrity landers. It is intended for the standard lightweight tensegrity robot to be deployed into critical disaster zones with human victims for rapid search-and-rescue, while structures with heavier payloads can be used to carry multiple sensor packages into remote areas after humans have initially evacuated such as in the event of a chemical spill.

Plots of the complete spectrum of drop test data for 22" robots provide multiple design insights into the scaling behavior of the tensegrity landers (Fig. 4.7 and 4.8). As expected from an intuitive perspective of impact and shock protection, an increase in drop height or total mass results in a higher measured peak payload acceleration. However, it should be noted that the robot effectively reaches terminal velocity within 25 to 30 m and the peak accelerations should begin to plateau around a certain range of values for a given design of a robot.

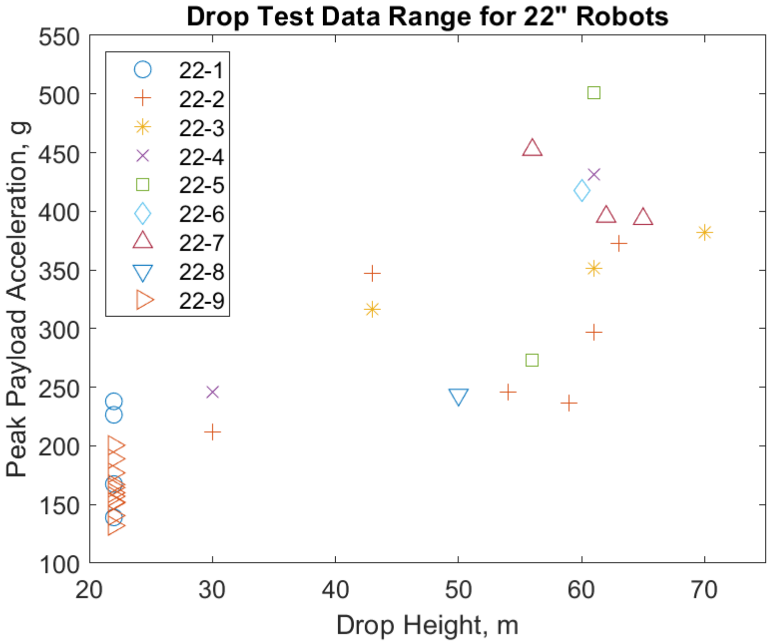

Figure 4.7: 22" robot aggregated drop test results, acceleration versus drop height

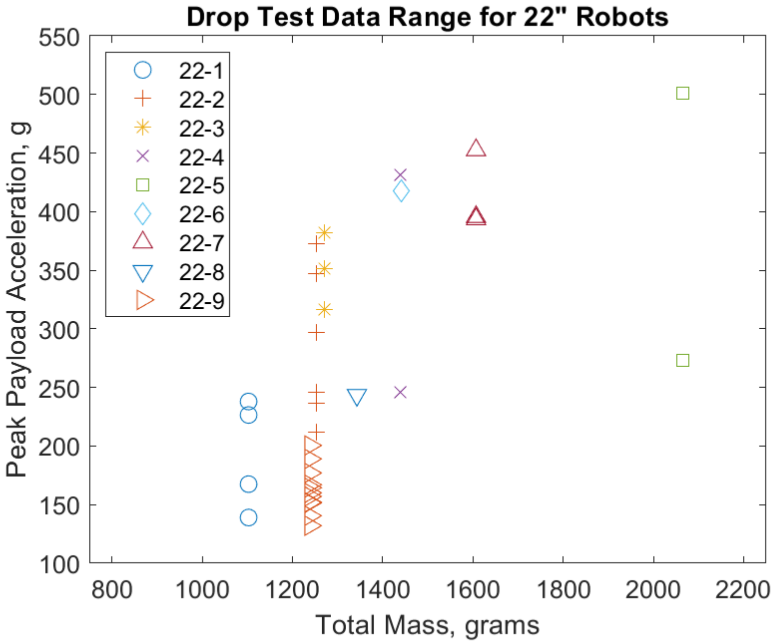

Figure 4.8: 22" robot aggregated drop test results, acceleration versus total mass

However, the aggregated plots of all data have many confounding variables within the design parameters of the robot. Examining the robot designs that vary one parameter while holding all others constant reveals a stronger correlation for these trends (Fig. 4.9 and 4.10). In both of these plots, the black markers indicate the base design of 22-1 while the colored markers track the effects of the designs with increased mass. The asymmetrically-weighted robots required testing at moderate-altitudes to characterize their in-air self-righting behavior, but the trend in the data indicates that even at 20 m drops the additional weights would result in higher peak payload accelerations than the base design.

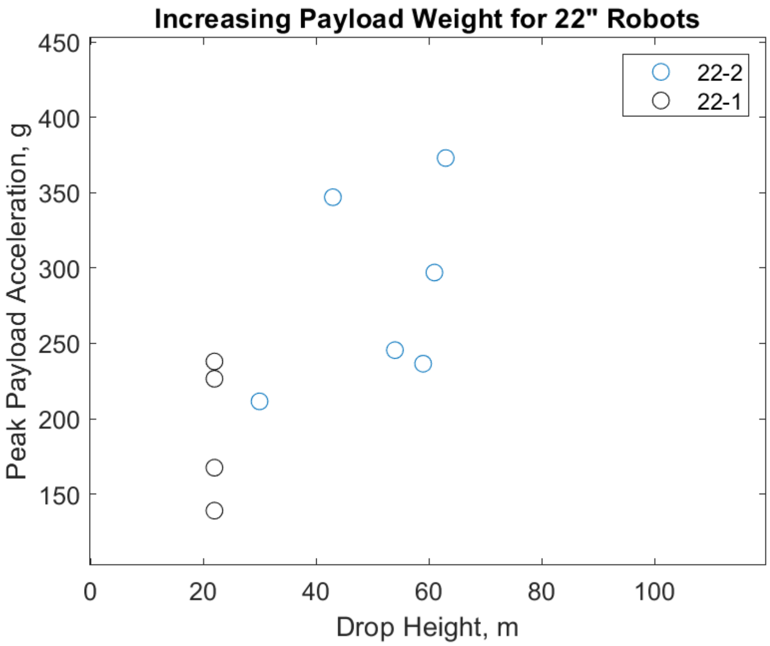

Figure 4.9: Drop test results of 22" robot with increased payload mass. Black: initial design, colors: increased payload weight

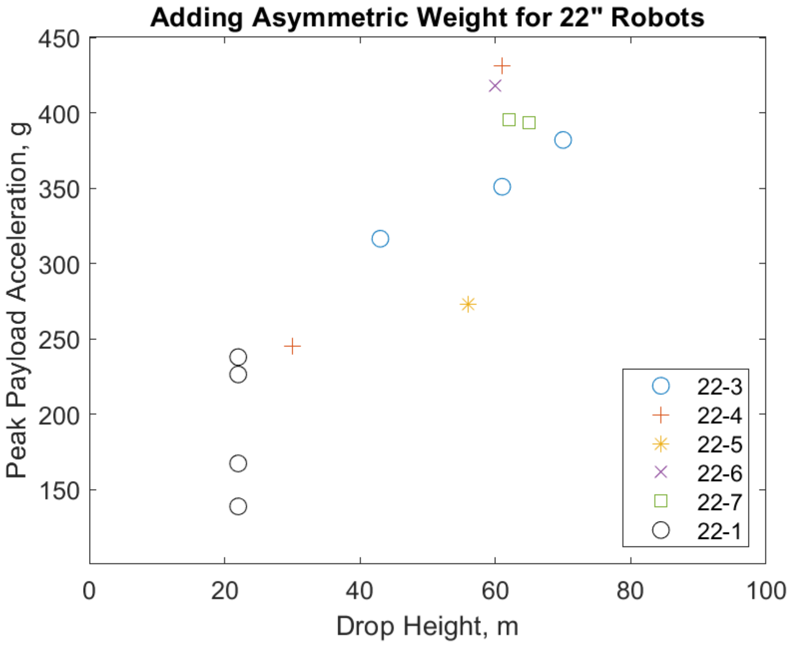

Figure 4.10: Drop test results of 22" robot with asymmetric weighting. Black: initial design, colors: with asymmetric weight

Finally, sorting the low-altitude drop test data by landing orientation agrees with the results found by the force plate impact tests to characterize the mass-spring-damper model (Fig. 4.11). The double rod landing orientation on average trends higher than the other two. However, the closed face and open face data experiences a substantial amount of overlap especially at higher impact velocities. This is due to the unpredictable nature of the drop and how minor variations of initial drop conditions greatly affect the landing orientation and the impact response. While it is beneficial to consider the closed face as the optimal landing orientation based on the force plate results, in which the landing orientation was precisely and easily controlled for a 1.5 m drop, in practice most landing impacts will be within the open face regime, as seen in the acceleration profiles for a set of closed face drops normalized in time to align the peak accelerations (Fig. 4.12). While some profiles are wider and have lower peaks, as expected for the closed face orientation, another subset behave more similarly to the open face profiles characterized by the force plate (Fig. 3.3). Consider how the structure nominally impacting on a closed face might have a slight rotation relative to the ground, or the ground could be an uneven surface as well. In this case, the rods begin to impact at a higher angle that aligns the impact force along the compression direction of the rods, which reduces the compressive response of the structure as its behavior starts to mirror that of the double rod landing.

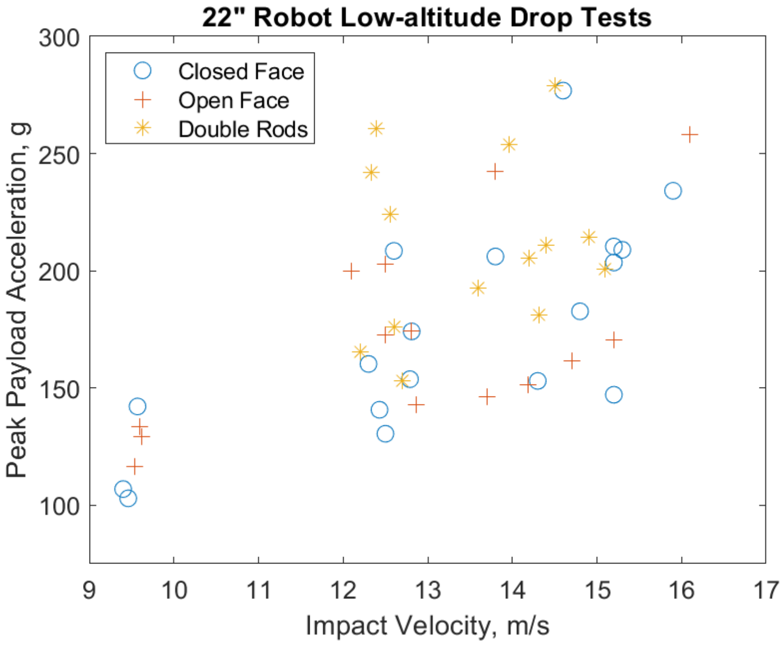

Figure 4.11: Low-altitude drop test results of 22" robot

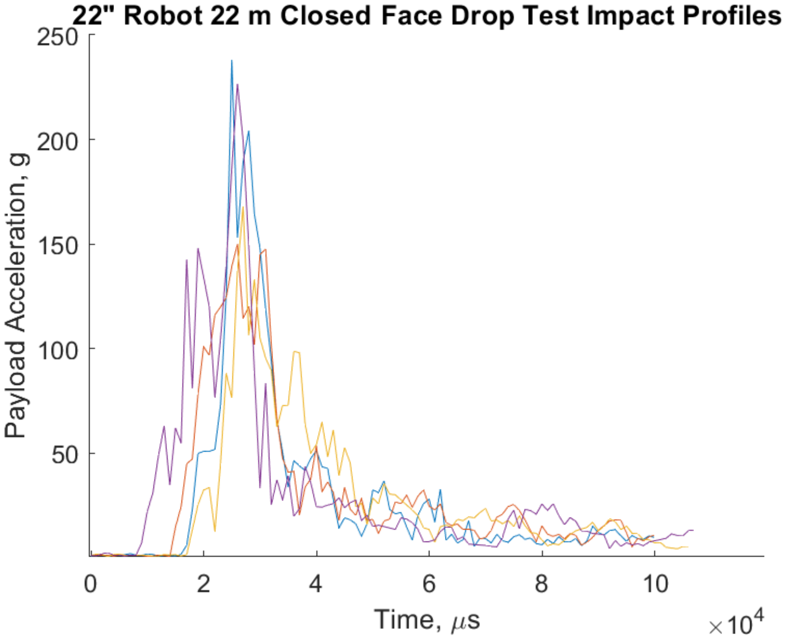

Figure 4.12: Low-altitude closed face drop test acceleration profiles of 22" robot

## 30" Robot

Similarly, multiple types of the 30" robot were developed to address various needs across mission scenarios (Table 4.4). The 30" robots were also considered for the asymmetrically-weighted designs and were also used to explore the deployment of increasingly massive payloads. The spring selection for each iteration was based on the design equations presented in Chapter 2 as well as qualitative insights from experimental testing.

Plots of the complete spectrum of drop test data for 30" robots provide additional validation for the design insights into the scaling behavior of the tensegrity landers (Fig. 4.13 and 4.14). Note that all high-altitude drops were clustered at 100 m due to lack of data on cargo plane flight altitude, but this should not affect the scaling results because the robots are at terminal velocity at any drop heights in this range.

In the same methodology as for the 22" robot, examining the 30" robot designs that vary one parameter while holding all others constant reveals a stronger correlation for the mass scaling trend (Fig. 4.15 and 4.16). In both of these plots, the black markers indicate the base design of 30-1 while the colored markers track the effects of the designs with increased mass.

| Robot Number | Description | Mass (kg) | Int/Ext Spring (N/m) |
|---|---|---|---|
| 30-1 | Standard | 1.320 | 740/520 |
| 30-2 | Light | 1.139 | 520/520 |
| 30-3 | Heavier Payload | 1.470 | 740/520 |
| 30-4 | Heavier Payload | 1.289 | 520/520 |
| 30-5 | Asymmetric 2 | 1.470 | 1030/520 |
| 30-6 | Asymmetric 3 | 2.360 | 860/860 |
| 30-7 | Heavy Payload | 1.745 | 620/320 |
| 30-8 | Heavy Payload | 3.735 | 1150/320 |

Table 4.4: Outline of 30" robot design parameters

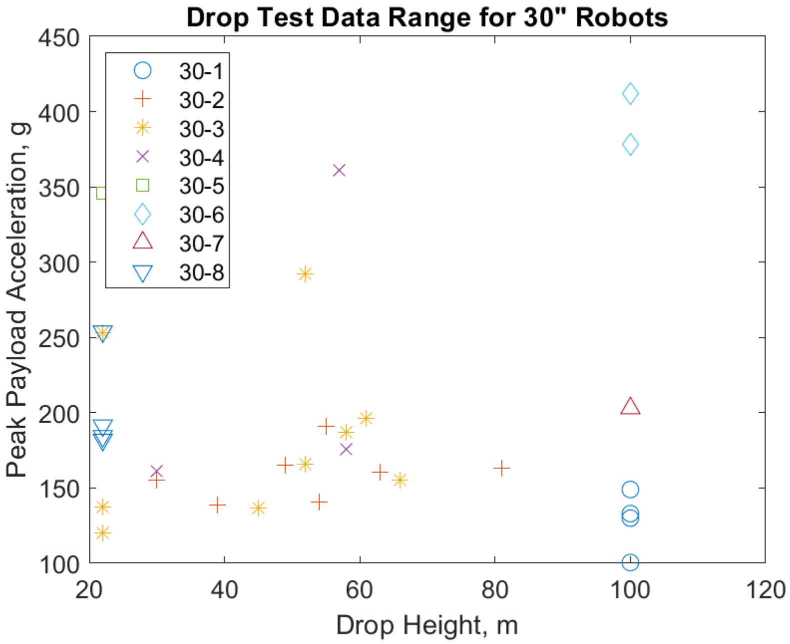

Figure 4.13: 30" robot aggregated drop test results, acceleration versus drop height

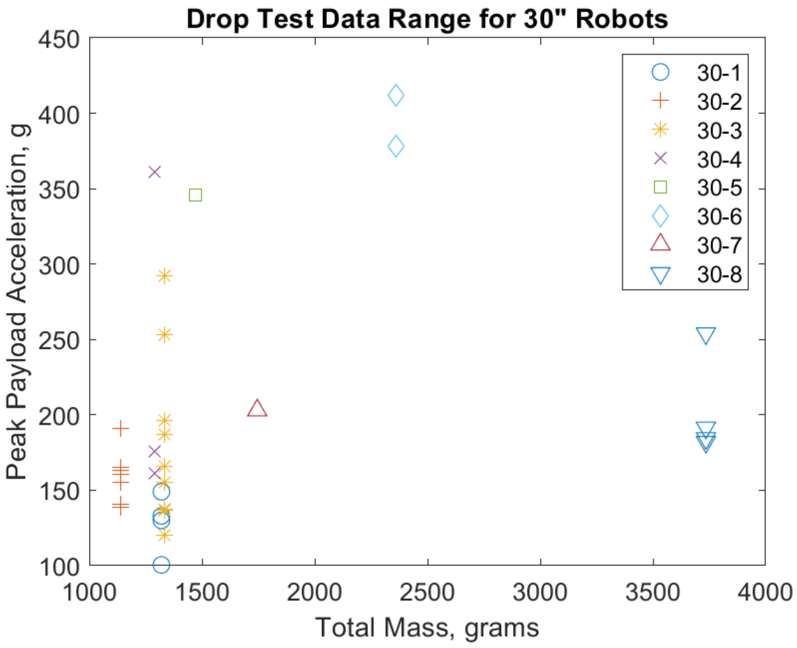

Figure 4.14: 30" robot aggregated drop test results, acceleration versus total mass

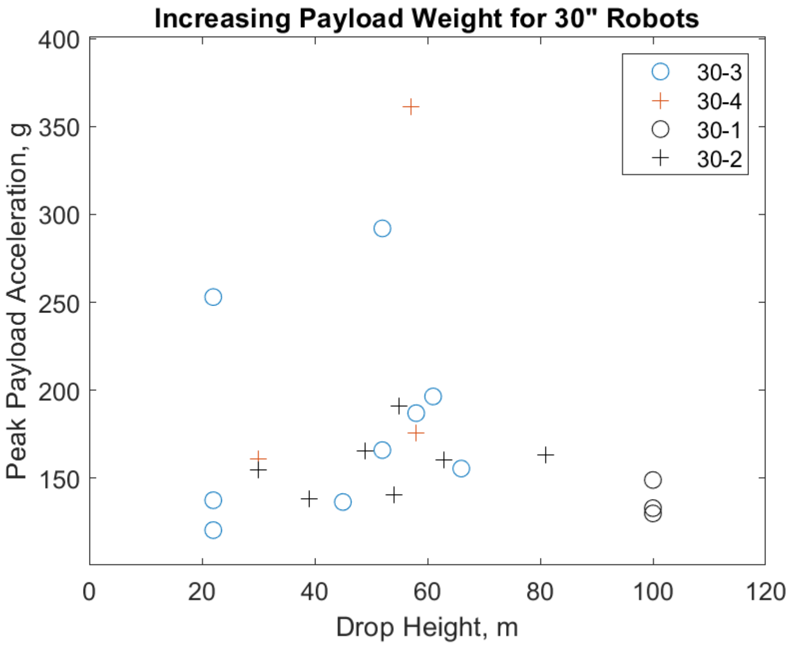

Figure 4.15: Drop test results of 30" robot with increased payload mass. Black: initial design, colors: increased payload weight, marker styles: matching robot designs

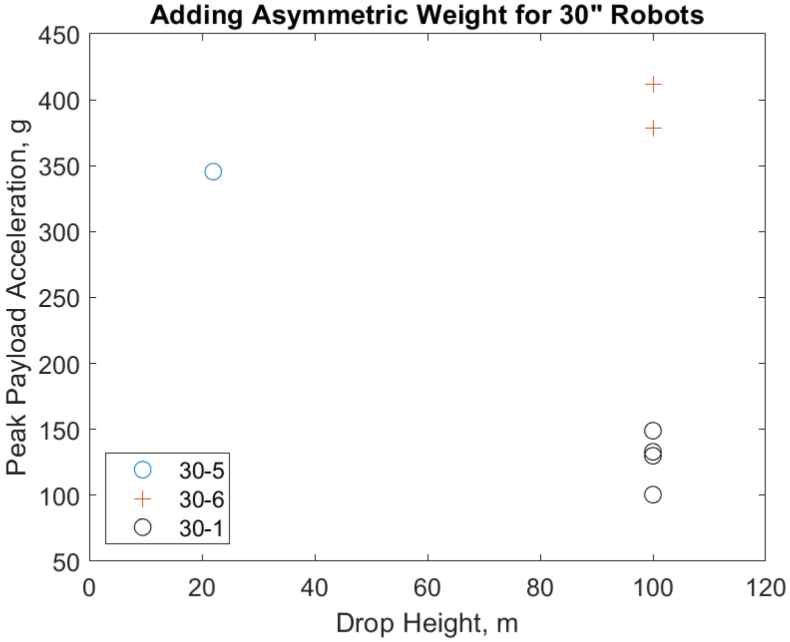

Figure 4.16: Drop test results of 30" robot with asymmetric weighting. Black: initial design, colors: with asymmetric weight

## 38" Robot

Again, multiple types of the 38" robot were developed to address various needs across mission scenarios (Table 4.5). The 38" robots were considered for the asymmetrically-weighted designs but primarily used to explore the deployment of increasingly massive payloads. The heaviest version, 38-8, was capable of carrying a 5 lb. payload at high-altitude drops. 38-9 was a tuned version of the structure based on the results of reorientation control, and will be discussed in greater detail in the next chapter. Its major accomplishment was a reduction in *total* mass and peak payload acceleration, for a heavy 38" robot carrying the same *payload* mass.

Plots of the complete spectrum of drop test data for 38" robots provide additional validation for the design insights into the scaling behavior of the tensegrity landers (Fig. 4.17 and 4.18).

Adding asymmetric weight while holding all other design variables constant reveals a stronger correlation for the mass scaling trend (Fig. 4.19 and 4.20). In both of these plots, the black markers indicate the base design while the colored markers track the effects of the designs with increased mass.

| **Robot Number** | **Description** | **Mass (kg)** | **Int/Ext Spring (N/m)** |
|---|---|---|---|
| 38-1 | Standard | 1.365 | 740/520 |
| 38-2 | Asymmetric 2 | 1.745 | 740/520 |
| 38-3 | Asymmetric 3 | 2.145 | 860/520 |
| 38-4 | Heavy Payload | 5.080 | 1420/620 |
| 38-5 | Heavy Payload | 5.104 | 1420/590 |
| 38-6 | Heavy Payload | 4.715 | 1790/1420 |
| 38-7 | Heavy Payload | 5.043 | 1790/1420 |
| 38-8 | Heavy Payload | 5.814 | 1790/1420 |
| 38-9 | Tuned Springs | 5.375 | 1790/1940 |

Table 4.5: Outline of 38" robot design parameters

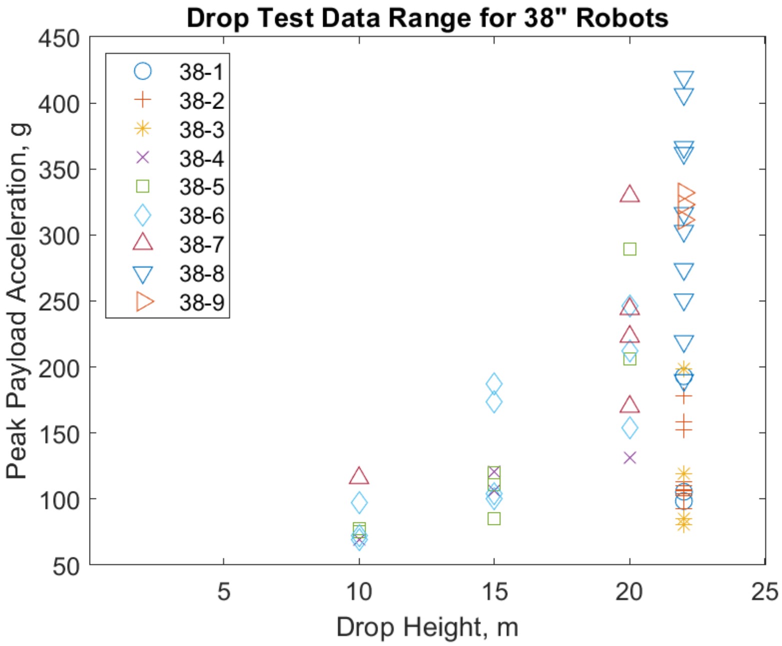

Figure 4.17: 38" robot aggregated drop test results, acceleration versus drop height

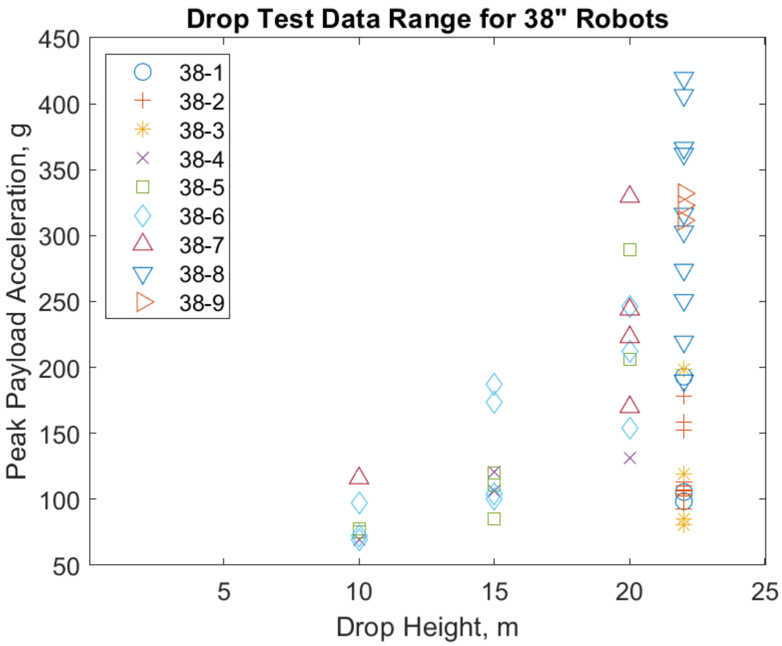

Figure 4.18: 38" robot aggregated drop test results, acceleration versus total mass

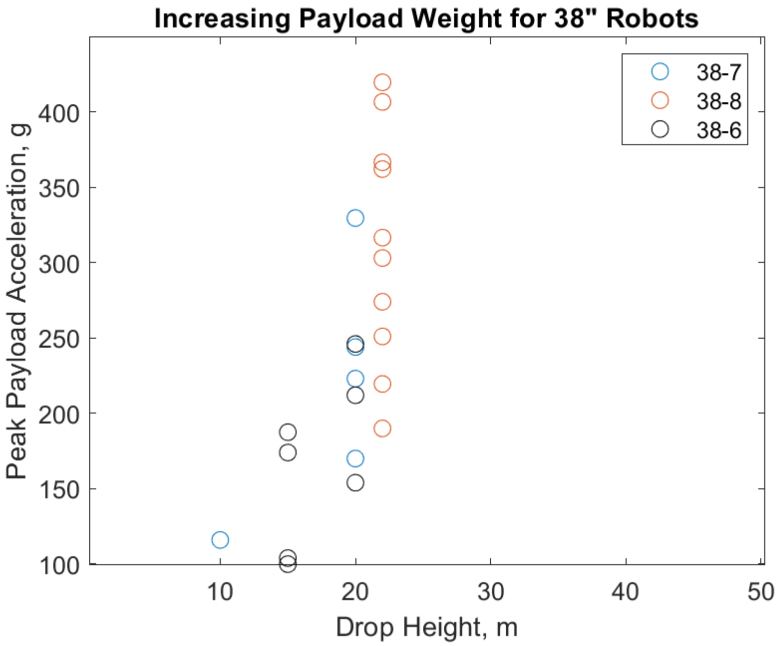

Figure 4.19: Drop test results of 38" robot with increased payload mass. Black: initial design, colors: increased payload weight

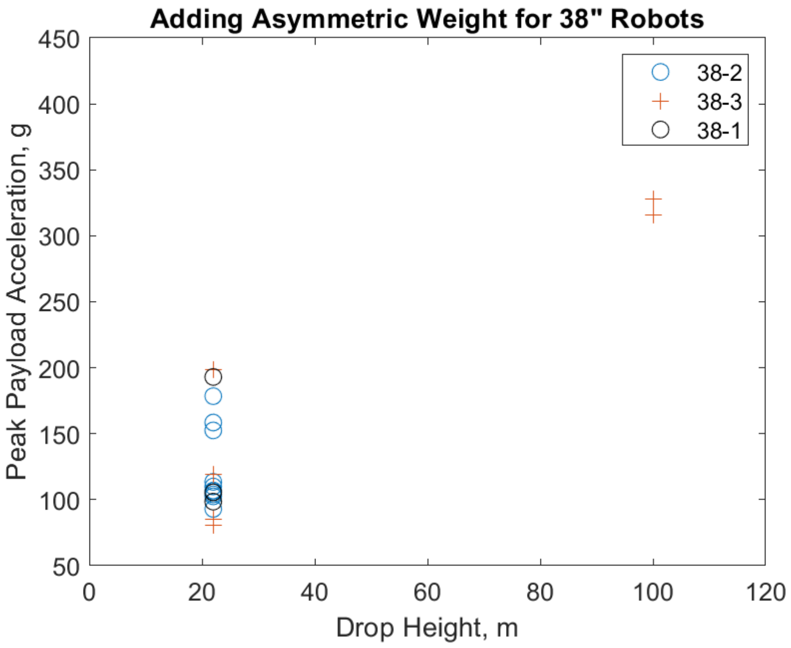

Figure 4.20: Drop test results of 38" robot with asymmetric weighting. Black: initial design, colors: with asymmetric weight

## 48" Robot

Only one type of the 48" robot was built and tested due to the size limitation concerns outlined previously (Table 4.6). This design was useful to characterize the effects of increasing the spherical radius, but further work is needed to develop heavier structures at this scale.

| Robot Number | Description | Mass (kg) | Int/Ext Spring (N/m) |
|---|---|---|---|
| 48-1 | Standard | 1.455 | 740/520 |

Table 4.6: Outline of 48" robot design parameters

Plots of the drop test data for the 48" robot provides additional validation for the design insights into the scaling behavior of the tensegrity landers (Fig. 4.21 and 4.22).

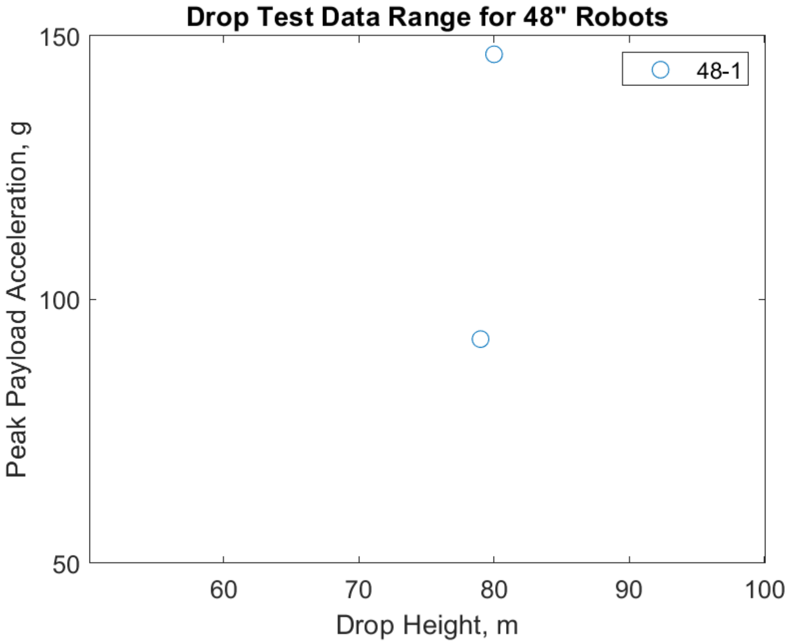

Figure 4.21: 48" robot aggregated drop test results, acceleration versus drop height

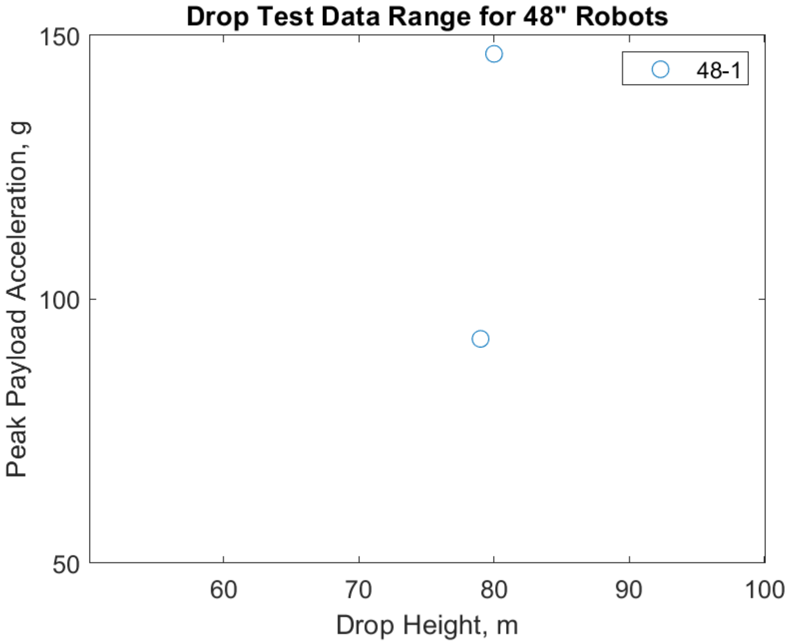

Figure 4.22: 48" robot aggregated drop test results, acceleration versus total mass

## 4.3 Empirical Scaling Laws

Considering now the impact behavior of the tensegrity structure across all designs, the same intuitive trends begin to emerge from the experimental data. Specifically, the increase in radius was correlated with a decrease in the peak acceleration due to the additional stopping distance provided by the structure, much like an airbag would perform during a vehicle collision (Fig. 4.23). This pattern is clearest when comparing the 22" (blue) and 30" (orange) robots of matching design (denoted by the + marker) in the 40-60 m range of drop heights. All other factors being equal, the cluster of data for the 30" robot has a clear difference from that of the 22" even when accounting for randomness of impact orientation. Increasing the stiffness of the springs was also shown to improve the impact performance (Fig. 4.24), with a change in the interior spring having a pronounced effect on the peak acceleration of the payload as previously discussed.

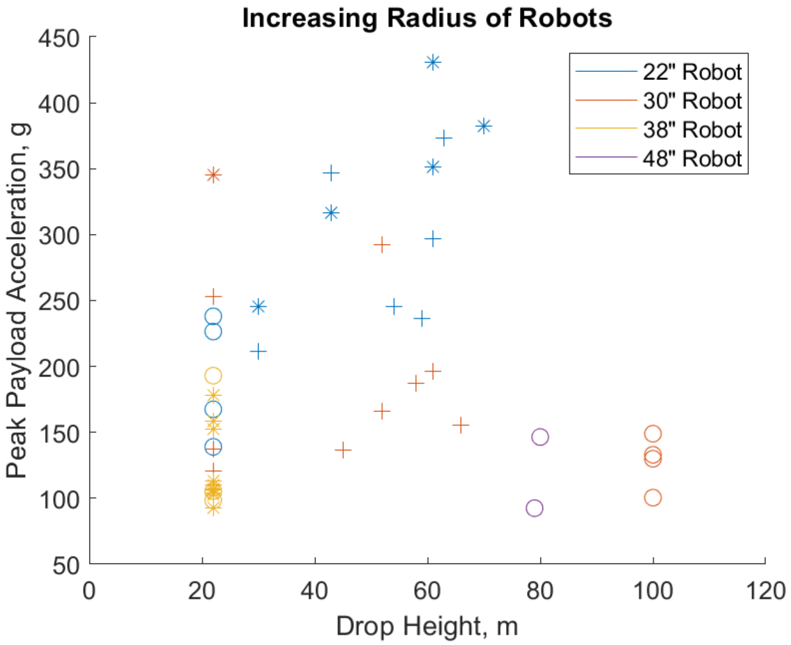

Figure 4.23: Effects of increasing radius on impact performance. Marker styles indicate matching designs across scales.

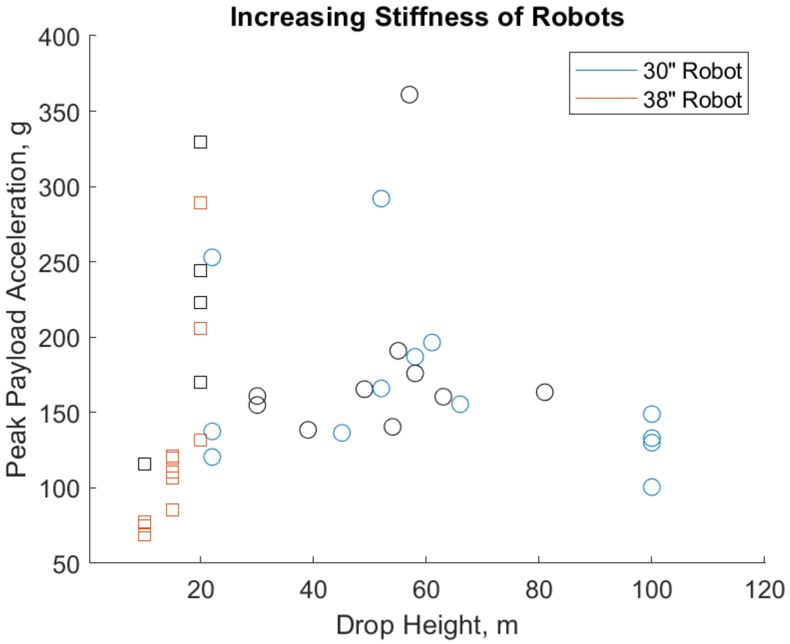

Figure 4.24: Effects of increasing stiffness on impact performance. Black: initial design, colors: improved stiffness, marker style: matching designs

Since the aggregated drop test results contain multiple variables that all affect the impact response of the structure, the acceleration data was then fit against two variables to investigate the correlation between them and propose empirical scaling laws that interpolate and predict performance metrics for new designs [72, 73]. With peak payload acceleration as the output parameter, drop height is a primary independent variable that must almost always be considered, so the polynomial surface fits compares it to total mass (Fig. 4.25), interior spring stiffness (Fig. 4.26), exterior spring stiffness (Fig. 4.27), and average spring stiffness (Fig. 4.28). The resulting polynomial surfaces are adjusted to be within the convex hull of the drop test data and therefore represent conservative boundaries for safe lander design since all data points represent a successful drop test of a particular tensegrity structure. The fit equations can be used to rapidly and efficiently evaluate the effects of new design parameters on the impact performance of the structure.

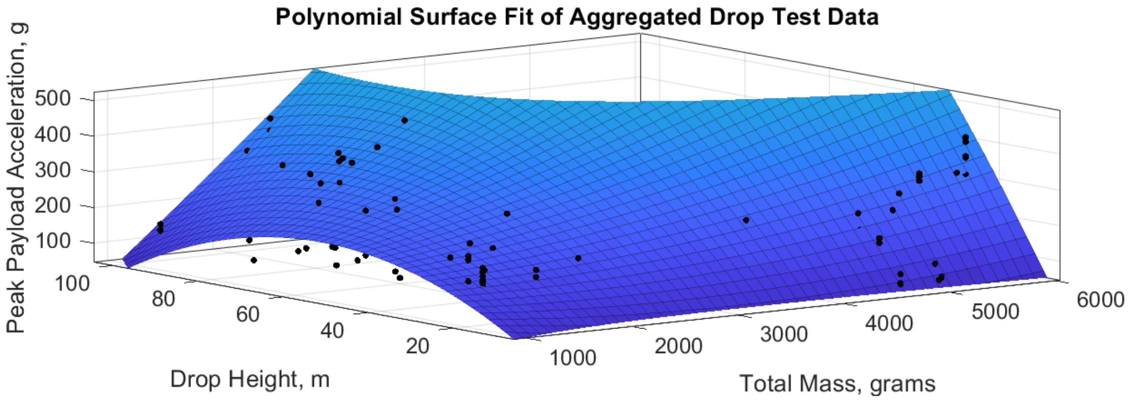

Figure 4.25: Polynomial surface fit of aggregated drop test data: peak acceleration as a function of total mass and drop height

The polynomial surface fit of acceleration $a$ as a function of mass $m$ and drop height $h$ is given by

$$a(m,h) = c_0 + c_1 m + c_2 h + c_3 m^2 + c_4 mh + c_5 h^2 \tag{4.1}$$

with fit parameters listed in Table 4.7.

| **Surface Fit Parameter** | **Value** |
|---|---|
| $c_0$ | 300.3 |
| $c_1$ | 117.1 |
| $c_2$ | 205.2 |
| $c_3$ | 21.9 |
| $c_4$ | 134.5 |
| $c_5$ | -52.7 |
| $R^2$ | 0.588 |

Table 4.7: Polynomial surface fit constants: peak acceleration as a function of total mass and drop height

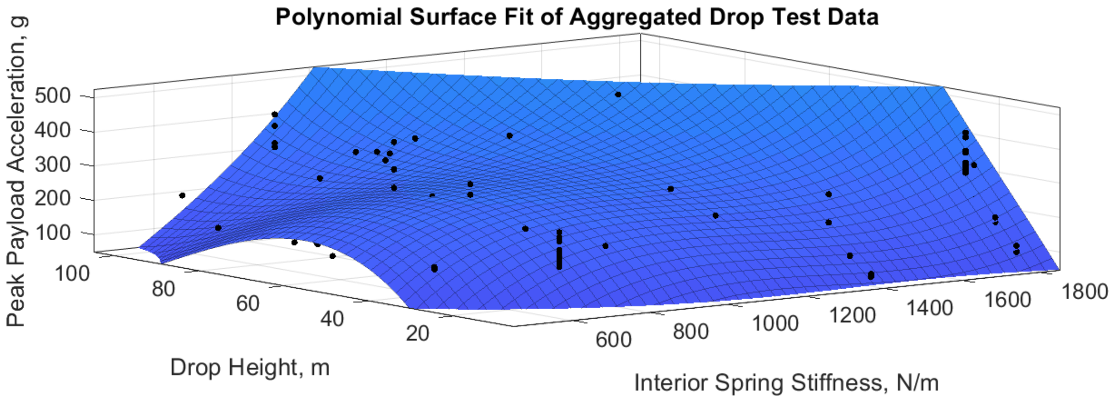

Figure 4.26: Polynomial surface fit of aggregated drop test data: peak acceleration as a function of interior spring stiffness and drop height

The polynomial surface fit of acceleration as a function of interior spring stiffness $k_{int}$ and drop height is given by

$$a(k_{int}, h) = c_0 + c_1 k_{int} + c_2 h + c_3 k_{int}^2 + c_4 k_{int} h + c_5 h^2 + c_6 k_{int}^3 + c_7 k_{int}^2 h + c_8 k_{int} h^2 + c_9 h^3 \quad (4.2)$$

with fit parameters listed in Table 4.8.

| **Surface Fit Parameter** | **Value** |
|---|---|
| $c_0$ | 285.7 |
| $c_1$ | -3.1 |
| $c_2$ | 104.9 |
| $c_3$ | -12.9 |
| $c_4$ | 38.8 |
| $c_5$ | -79.1 |
| $c_6$ | 63.5 |
| $c_7$ | 99.9 |
| $c_8$ | 80.1 |
| $c_9$ | 30.2 |
| $R^2$ | 0.5544 |

Table 4.8: Polynomial surface fit constants: peak acceleration as a function of interior spring stiffness and drop height

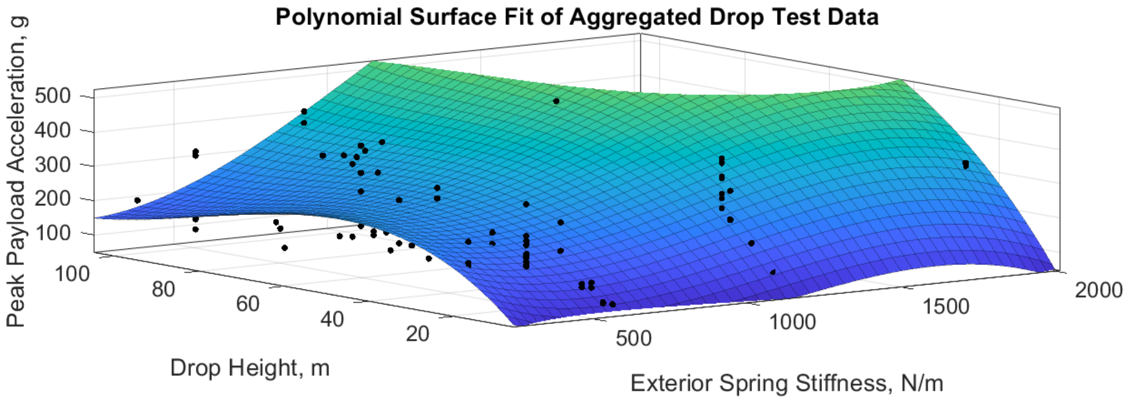

Figure 4.27: Polynomial surface fit of aggregated drop test data: peak acceleration as a function of exterior spring stiffness and drop height

The polynomial surface fit of acceleration as a function of exterior spring stiffness $k_{ext}$ and drop height is given by

$$a(k_{ext}, h) = c_0 + c_1 k_{ext} + c_2 h + c_3 k_{ext}^2 + c_4 k_{ext} h + c_5 h^2 + c_6 k_{ext}^3 + c_7 k_{ext}^2 h + c_8 k_{ext} h^2 + c_9 h^3 \quad (4.3)$$

with fit parameters listed in Table 4.9.

| **Surface Fit Parameter** | **Value** |
|---|---|
| $c_0$ | 253.9 |
| $c_1$ | 56.7 |
| $c_2$ | 109.8 |
| $c_3$ | 33.5 |
| $c_4$ | 36.3 |
| $c_5$ | -77.6 |
| $c_6$ | -8.8 |
| $c_7$ | -0.55 |
| $c_8$ | -0.51 |
| $c_9$ | 14.7 |
| $R^2$ | 0.4779 |

Table 4.9: Polynomial surface fit constants: peak acceleration as a function of exterior spring stiffness and drop height

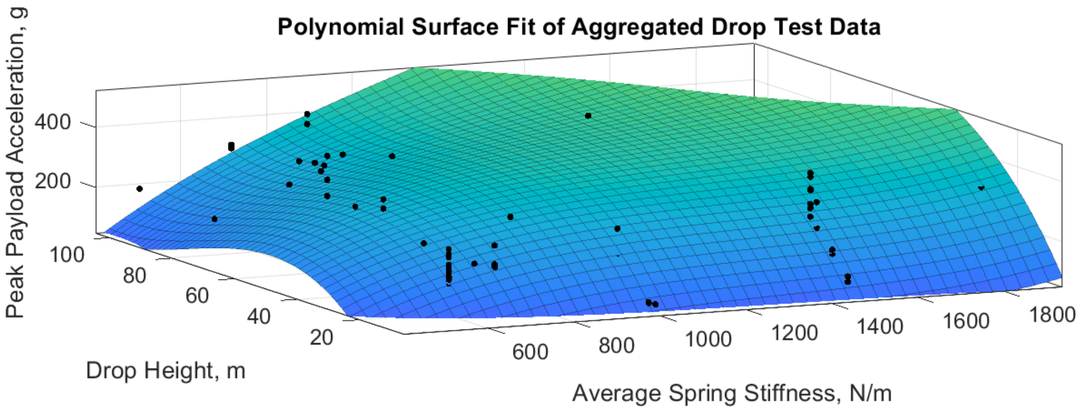

Figure 4.28: Polynomial surface fit of aggregated drop test data: peak acceleration as a function of average spring stiffness and drop height

The polynomial surface fit of acceleration as a function of average spring stiffness $k_{avg}$ and drop height is given by

$$a(k_{avg}, h) = c_0 + c_1 k_{avg} + c_2 h + c_3 k_{avg}^2 + c_4 k_{avg} h + c_5 h^2 + c_6 k_{avg}^3 + c_7 k_{avg}^2 h + c_8 k_{avg} h^2 + c_8 h^3 \quad (4.4)$$

with fit parameters listed in Table 4.10.

| **Surface Fit Parameter** | **Value** |
|---|---|
| $c_0$ | 326.7 |
| $c_1$ | 76.4 |
| $c_2$ | 132.0 |
| $c_3$ | -42.5 |
| $c_4$ | 15.9 |
| $c_5$ | -120.7 |
| $c_6$ | 12.9 |
| $c_7$ | 3.2 |
| $c_8$ | 12.8 |
| $c_9$ | 29.1 |
| $R^2$ | 0.5427 |

Table 4.10: Polynomial surface fit constants: peak acceleration as a function of average spring stiffness and drop height

Each surface fit behaves remarkably similarly in terms of qualitative shape as well as the numerical fit constants and goodness-of-fit, potentially indicating that the design parameters carry relatively equal weight on the final impact performance of the structure. Evaluating proposed design parameters along this series of surface curves can be a rapid and methodical approach to quickly determine the viability of a new tensegrity lander. However, some caution must be exercised when using simple polynomial surface fits which are limited to low order approximations and are unable to create a fully generalized surface model over a wide domain. For the drop test data, the surface fits are unable to capture the plateauing of the peak acceleration after terminal velocity is reached but the correct initial increase is observed. Furthermore, there are gaps in the independent variables that were not systematically tested in the tensegrity lander design process. This was due to mission constraints of required payload mass for certain objectives and the corresponding subset of available spring stiffnesses that could support the impact energy requirements of the heavier payload. The surface fit naturally loses accuracy as it models the impact behavior over an untested range of design parameters. Filling in the gaps of the model with finer resolution design changes would address this challenge and provide an accurate point cloud of drop test results for precisely defined scaling laws in the future.

# Chapter 5

# Landing Orientation Control

## 5.1 Motivation

While parachutes are the conventional approach for airdrop operations, “the process of de-rigging the parachute on landing has historically been a manual task” [74]. This poses a challenge for autonomous deployment of ground-based sensors that cannot be obscured by parachutes since parachutes may become tangled over the payload upon landing and often require manual de-rigging in these situations. Additionally, ground-based sensors often must be placed in required orientations (e.g., to ensure that cameras are pointed horizontally and that antennas are pointed toward the sky). Such emplacement requirements pose additional constraints on autonomous deployment, as the payload must come to rest in the correct orientation after landing without an operator manually adjusting the sensor position.

In addition to the impact-resilient properties previously discussed, tensegrity structures have a set of unique characteristics that make them especially ideal for the autonomous deployment of orientation-dependent sensors. Compared to a payload with parachutes and consumable decelerator material, tensegrities may have a greater potential to be rapidly, accurately, and autonomously deployed to a target location. They fall at higher velocities with a reduced visual signature and less lateral drift. The lightweight exterior structure provides minimal obstruction to visual sensors (Fig. 5.1). The tensegrity structures also act as their own impact decelerators and can be efficiently reused through multiple drops to reduce preparation time and material waste between deployments.

Figure 5.1: View from one of the six cameras on the tensegrity robot

The ability to guarantee orientation of the payload is a required functionality "to ensure the device is oriented such that any antennas may be pointing upward, or other sensor features are within their respective planes of operation" [74]. This requirement presents a challenge for a tensegrity-based system because a tensegrity typically absorbs energy using passive compliance and bounces several times upon landing. The exact result of this bouncing motion has been extremely difficult to predict and is sensitive to impact conditions, but based on the previous drop test experiments the closed face landing was identified as the most stable orientation for both payload protection and structural motion.

Several different active (i.e., powered) and passive options to achieve self-righting were considered prior to this work. Active solutions [24, 75] were disfavored as it was determined that the necessary actuators to guarantee orientation using a locomotion-based approach after landing led to an unreasonably large weight addition from motors, batteries, and other electronics that could be better applied to passive solutions and increased payload capacity.

## 5.2 Asymmetrically-Weighted Structure

### Modeling and Design

Passive self-righting solutions were first explored by attaching shaft collars on selected rods (Fig. 5.2). The advantage of this approach was that it did not require significant redesign of the tensegrity structure. Overall, this asymmetrically-weighted tensegrity structure behaved like a loaded dice [76] such that the tensegrity would preferentially roll towards a particular face during the impact process.

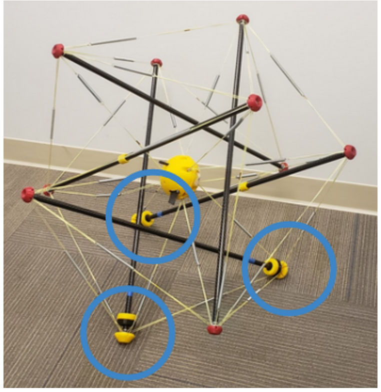

Figure 5.2: 38" tensegrity robot with asymmetric weights (circled). Target orientation is the closed face defined by the weighted nodes.

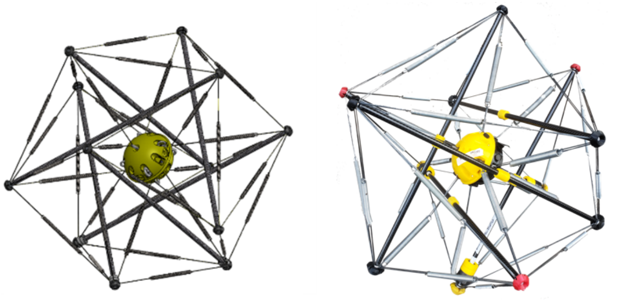

Figure 5.3: 38" robot SOLIDWORKS model (left) and asymmetrically-weighted prototype (right)

A physics-based rotational dynamics model was implemented in MATLAB to predict the oscillation time of an asymmetrically-weighted robot. The system was approximated as a rigid, damped, compound pendulum with the asymmetric weights summed at their average position relative to the center of rotation. The robot's moment of inertia was calculated from a SOLIDWORKS model (Fig. 5.3).

Simulation results of the self-righting robots indicated that the robot would have adequate time to correctly reorient itself in midair before landing on the ground, regardless of initial conditions (Fig. 5.4). The addition of further weights also aids tremendously by rolling the structure to its target face after it has finished bouncing. Various amounts of weight were tested in experiment to investigate tradeoffs between the reorientation benefits and the increased impact force due to additional weights.

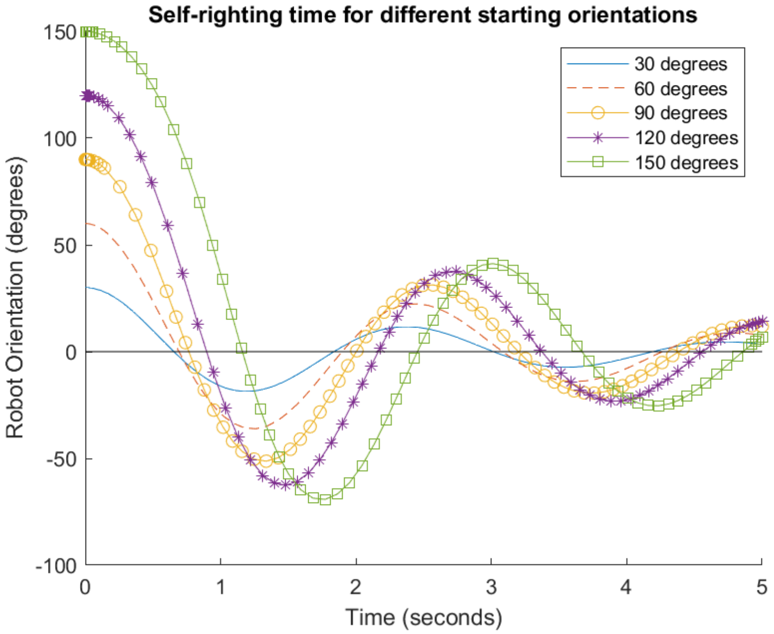

Figure 5.4: Simulated orientation data for an asymmetrically-weighted robot in free-fall. Target orientation is at zero degrees.

Taking into consideration that the robot will have subsequent bounces after its initial impact, the oscillation time was chosen to be on the same order as the timeframe of a single bounce such that the final landing position maintains the correct orientation. Given that bounces last approximately 1 s as observed in previous experimental data and assuming that the robot does not deviate more than 150° from the target orientation, the weights could be chosen for an oscillation period of at most 4 s or a quarter cycle of 1 s. Another major factor in the self-righting behavior was that the robot only needed to land within a sufficient margin from the target face so that the asymmetric weights would still cause the robot to preferentially roll to the target face after the final bounce. If the robot landed and came to a temporary rest one or two faces away from the target face, then the weights could also passively induce a correcting rotation. In this way, the orientation control had additional safeguards against the erratic and highly dynamic post-impact bouncing behavior.

Figure 5.5: Comparison of rod inserts. From left to right: shaft collars, carbon fiber rod, lengthened insert, standard insert.

The tensegrity structure required slight design modifications to account for the addition of the shaft collars. First, a protective TPU cover was placed over each shaft collar since sharp burrs could build up over repeated impacts with the ground and pose a cutting hazard to the structure's cables. In an unmodified tensegrity, the addition of a large, rigid mass in the form of shaft collars on the end of a comparatively thin carbon fiber rod can lead to rod breakage on impact. The wall thickness of the carbon fiber rods was increased, and the aluminum insert within each rod's endcap was lengthened in response (Fig. 5.5). The goal was to prevent rod fracture from the additional weight of the shaft collars as well as the stress concentration at the clamped surface. A conservative static stress analysis predicted that the stress was reduced by 13% when considering the total weight of the assembly acting on a single cross-sectional area of the rod. The reduction in the rod's peak impact stress resulting from these design decisions was validated in an impact simulation solved in ANSYS LS-Dyna. A simplified drop test simulated a single rod assembly impacting the ground diagonally at a typical landing speed of 15 m/s. The effects of cables and other rods during impact was ignored due to the negligible magnitude compared to the direct impact with the ground as well as to reduce computational cost. The peak equivalent (von-Mises) stress was reported to be 4.14E8 Pa compared to 5.35E8 Pa for an unmodified rod carrying asymmetric weights, or a 22.6% reduction (Fig. 5.6). This is lower than the nominal max equivalent stress of single strand carbon fiber specified by the manufacturer, 4.45E8 Pa. While the exact strength of the overall rod is is unspecified and depends heavily upon the particular weave of the carbon fiber layers, it is assumed that it is at least greater than that of the single strand carbon fiber and less than the simulated value that resulted in rod fractures during corresponding experiments.

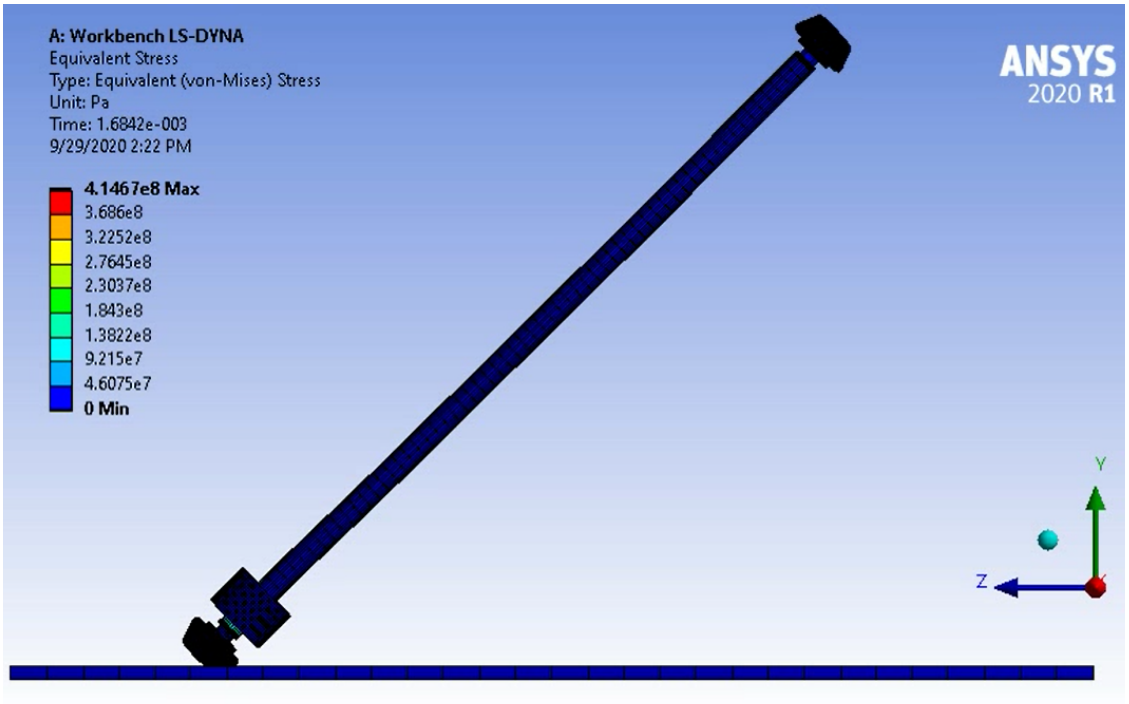

Figure 5.6: ANSYS impact simulation of a single asymmetrically-weighted rod

## Drop Test Experiments

The self-righting tensegrity landers were tested in two different ways: high-altitude drops from a drone (up to 122 m) or cargo plane (over 300 m) to observe the in-air reorientation control and settling time, and low-altitude drops from a building (22 m) to better characterize the post-impact bouncing. For each test, the starting orientation was randomized to mimic the free-fall tumble experienced when deployed from a cargo plane. Two onboard sensors, a 400g-rated accelerometer and inertial measurement unit (IMU), logged the robot's acceleration and orientation, respectively. The orientation data was compared to the acceleration data as well as video capture of the drop to identify the orientation of the robot both during impact and at its final resting state. The angular difference between the experimental IMU gravity vector and the calibrated reading when resting on the target face was used to quantify the orientation error. The experimental tests focused primarily on the 22" robot with some additional tests on scaled 30" and 38" robots carrying heavier payloads (Table 5.1 and 5.2). The asymmetric weights for these larger robots were chosen to mimic the oscillation time found on the 22" robot. Because of the larger mounting radii of the weights on these larger robots, the total amount of added mass was quite similar to that on the smaller robot. Also, note that larger robots were unable to be dropped by drone due to weight capacity limitations.

| **Robot Size (in.)** | **Total Weight (lb.), before addition of asymmetric weights** | **Payload Weight (lb.)** |
|---|---|---|
| 22 | 2.42 | 0.79 |
| 30 | 6.98 | 2.50 |
| 38 | 11.19 | 5.00 |

Table 5.1: Overview of asymmetrically-weighted robot prototypes

| **Robot Size (in.)** | **Number of Weights** | **Building Drops** | **Drone Drops** | **Plane Drops** |
|---|---|---|---|---|
| 22 | 3 (0.42 lb.) | - | 4 | - |
| | 6 (0.85 lb.) | 23 | 10 | 3 |
| | 9 (1.27 lb.) | - | 3 | - |
| 30 | 6 | 3 | - | - |
| | 9 | - | - | 3 |
| 38 | 6 | 10 | - | - |
| | 9 | 11 | - | 3 |
| | 12 (1.69 lb.) | 3 | - | - |

Table 5.2: Overview of drop test experiments for asymmetrically-weighted prototypes

Self-righting capability was first demonstrated on a 22" robot carrying a 0.79 lb. payload. Overall, this method of self-righting yielded the correct final orientation in more than 60% of the 22" robot drop tests (Table 5.3). Orientation data from these low-altitude drop tests confirmed that the asymmetric system was indeed oscillating according to the damped pendulum model and that the oscillation period is within the design parameters specified (Fig. 5.7). Note that the target orientation is at $\theta = 0°$ and that any tilting of the structure will result in a positive angular error measured by the IMU regardless of direction. A successful landing is defined as one in which the preferred face is resting on the ground in the robot's final orientation. This constraint corresponds to an angular error of less than 15° from vertical, driven mostly by minor variations in ground surfaces. Average error is calculated across all drop tests regardless of success. The vast majority (approximately 90%) of the tests resulted in the robot landing within one face of the target which is still sufficient for satisfactory sensor operation. The next closest face of the tensegrity that it can stably rest on has a surface normal 39.2° away from that of the target face, so any measured deviations within 15° were considered as the correct orientation after confirming with the recorded video. The success rate can be affected by the amount of asymmetric mass that is added and was shown to be relatively robust to the presence of small obstacles (e.g., rocks, non-level surfaces) in the drop zone as well as different ground materials (e.g., grass, concrete) that provided varying bounce behavior depending on their coefficient of restitution. However, the success rate was negatively impacted by larger obstacles (e.g., bushes, walls) that could impede the robots' reorientation if they collided during a bounce.

| **Number of Weights** | **Success Rate (%)** | **Average Final Error (°)** | **Average Impact Error (°)** |
|---|---|---|---|
| 3 | 66.7 | 60.0 | 19.6 |
| 6 | 77.8 | 15.7 | 19.6 |
| 9 | 66.7 | 25.0 | 44.4 |

Table 5.3: 22" robot drop combined test results for different asymmetric weights

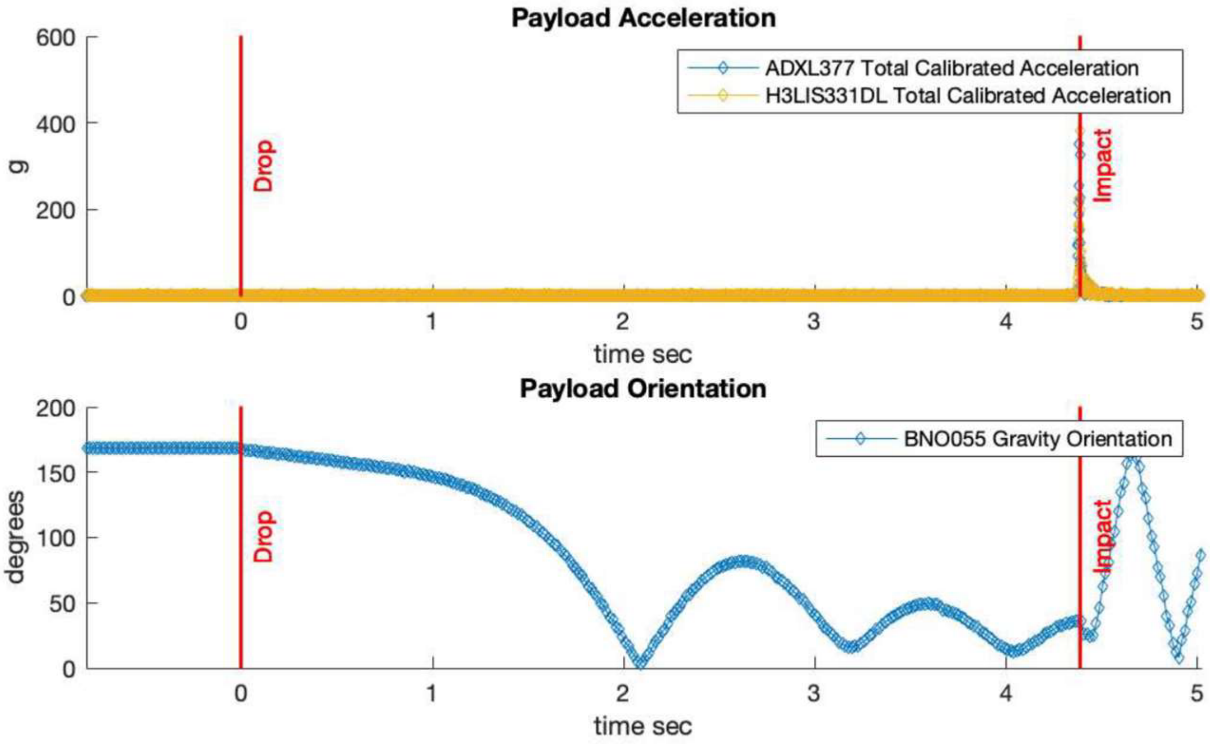

Figure 5.7: Representative low-altitude drop test data for 22" asymmetric robot with key events labeled. From top: acceleration and angular position over time

The self-righting design was then scaled for 30" and 38" robots carrying incrementally larger payloads up to 5 lb. Aggregated results from low altitude drops indicated that these robots had a similar rate of successful reorientation during the post-impact bouncing (Table 5.4), although the drop heights were not large enough to provide adequate time for the robot to always reorient before landing. Due to logistical limitations in cargo plane drop tests, each robot could only be tested a few times. Nevertheless, the 100% success rate in these tests proved to be an extremely promising demonstration of the self-righting orientation control when applied to a larger and heavier robot (Table 5.5, Fig. 5.8). It indicates that the self-righting properties can be successful across different scales of tensegrity structures with careful tuning of asymmetric weights.

| **Robot Size (in.)** | **Success Rate (%)** | **Average Final Error (°)** | **Average Impact Error (°)** |
|---|---|---|---|
| 30 | 57.1 | 37.5 | 16.0 |
| 38 | 61.5 | 28.9 | 22.3 |

Table 5.4: 30" and 38" robot building drop test results across all asymmetric weights

| **Robot Size (in.)** | **Test** | **Final Error (°)** | **Impact Error (°)** |
|---|---|---|---|
| 30 | 1 | 2.2 | 1.7 |
| | 2 | 8.2 | Data Shutoff |
| | 3 | 10.6 | 7.2 |
| 38 | 1 | 6.1 | 4.9 |
| | 2 | 11.3 | 45.1 |

Table 5.5: 30" and 38" robot cargo plane drop test results, 9 asymmetric weights each

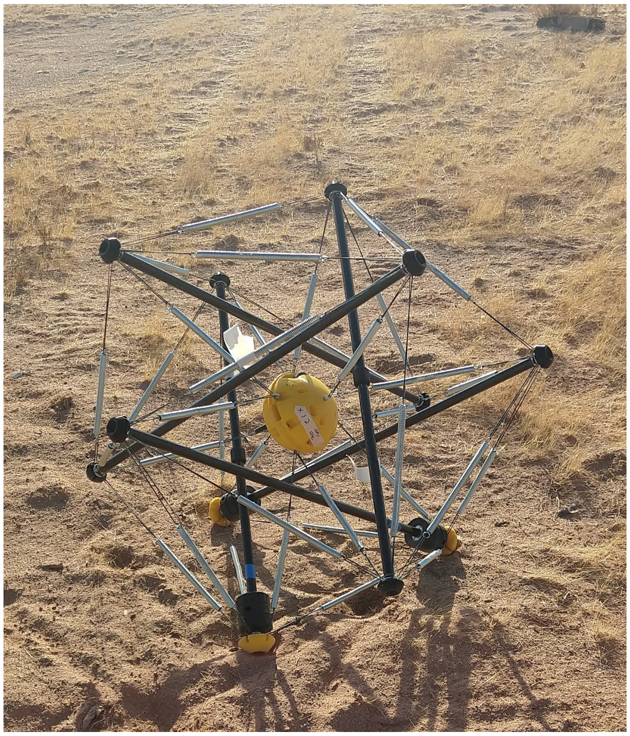

Figure 5.8: 30" robot correctly oriented after cargo plane drop test

The sensor data from high-altitude drop tests provide a valuable perspective on the unified in-air reorientation, settling, and post-impact bouncing for a single drop test (Fig. 5.9). The robot starts at rest in the cargo plane before being deployed. The sudden change in air pressure causes it to begin tumbling as it falls, but it stabilizes approximately 8 seconds into the drop which lasts approximately 25 seconds total. At impact there is a large peak in acceleration followed by several seconds of subsequent bouncing and self-righting as shown in the angular position subplot before the robot finally comes to rest. Overall, most of these high-altitude tests successfully resulted in both a correct impact and landing orientation for the self-righting robots.

As expected, the increased system mass from the asymmetric weights lead to an increased but still acceptable terminal velocity and peak acceleration (i.e., remaining below a threshold of 500 g). In particular, a 200% increase in asymmetrical weights on the 22" robot resulted in only an 8% increase in peak acceleration while greatly improving the orientation error. However, there was a noticeable decrease in the usable lifecycle (i.e., number of drops) for the self-righting robots due to the accumulated wear on the structure cables and springs. Therefore, there exists a tradeoff among payload mass, self-righting capabilities, and impact attenuation that must be considered when designing robots for new payloads in the future [77].

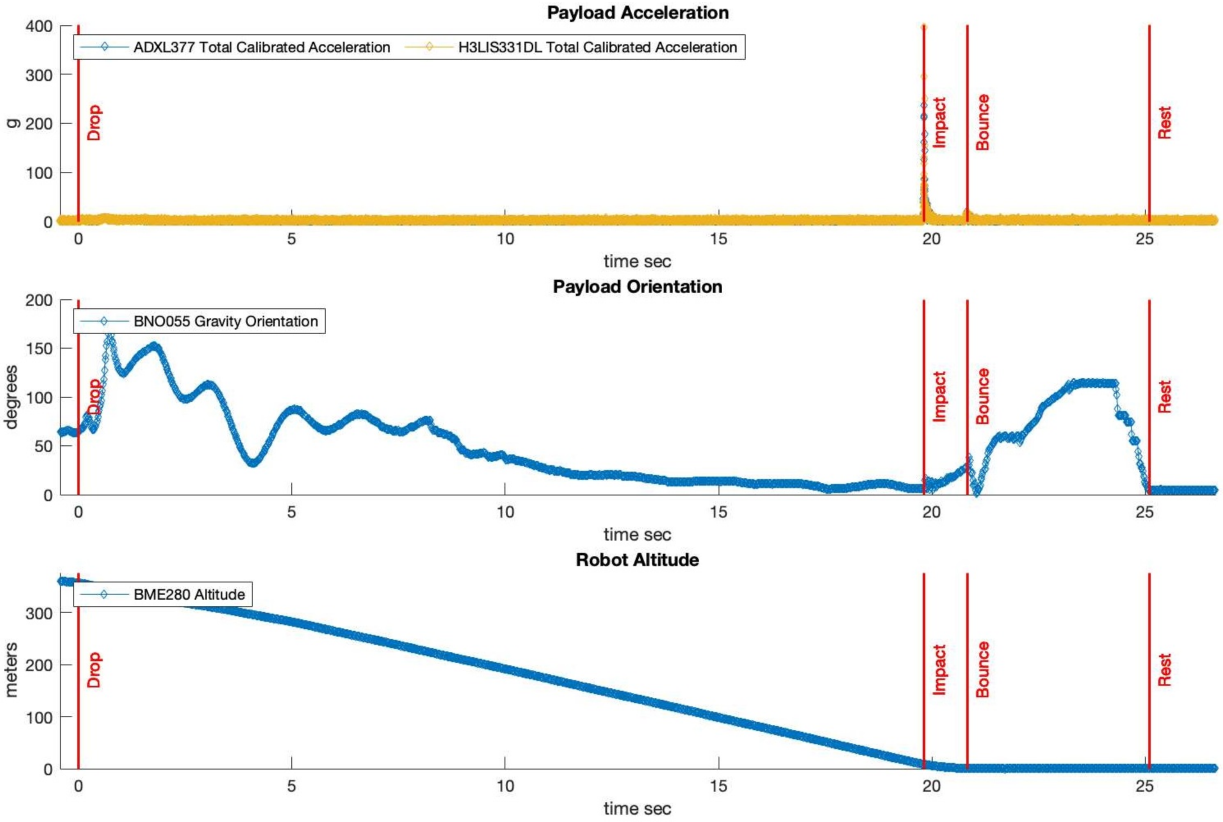

Figure 5.9: 38" robot cargo plane drop test data with key events labeled. Target orientation is at zero degrees. From top: acceleration, angular position, and altitude over time.

## 5.3 Badminton-Inspired Structure

### Modeling and Design

While the asymmetrically-weighted solution was moderately successful in maintaining the correct final sensor orientation, the design of a badminton-inspired self-righting tensegrity lander was explored as a more reliable and mass-efficient solution to controlling sensor orientation during deployment. The badminton birdie is characterized by its lightweight design and its quick turnaround time after impact with a racket such that the structure is always flying nose-first. By design, the center of mass (CoM) is separated from the center of pressure (CoP) so that when the birdie is not aligned with its direction of travel, the drag force on the center of pressure exerts a stabilizing torque on the structure to maintain alignment with the flight trajectory [78–80]. Due to these unique self-righting properties, a badminton tensegrity structure was considered as an alternative solution to the challenges associated with deploying orientation-dependent sensors. Its lightweight design has the additional benefit of redistributing mass to avoid stress concentrations and material failure as seen in the asymmetrically weighted solution.

A simplified rigid-body rotation model was used to predict the stabilizing behavior of the structure during free-fall (Fig. 5.10). If it is falling with velocity $v$ and is not aligned with the direction of travel by an angular deviation $\theta$ from the vertical axis, it will experience a stabilizing drag force $F_D$ acting at its CoP, located a distance $l$ away from its CoM.

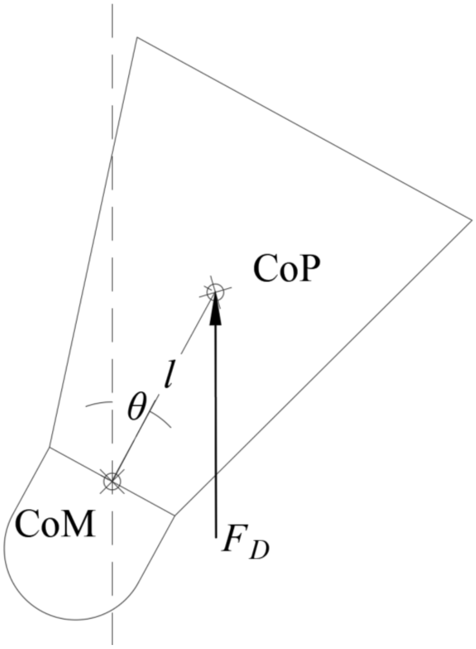

Figure 5.10: Stabilizing force on falling badminton birdie when not aligned with the vertical axis (dashed line)

At any given instant, the stabilizing torque $\tau_s$ on the structure can be used to calculate the angular acceleration $\alpha$ using

$$\tau_s = F_D l \sin\theta = I\alpha \tag{5.1}$$

where $I$ is the rotational inertia of the structure. This angular acceleration can then be used to solve for the time needed to rotate the structure back to its desired orientation using standard rotational kinematic equations.

Several assumptions were made in the initial solution of this rotation model as a proof of concept for the badminton tensegrity structure. The icosahedral tensegrity structure was approximated by its circumscribed bounding sphere (13") and the attached cone had mass and dimensions chosen to maintain the same aspect ratio as that of the badminton birdie. The overall geometry was approximated as a long cylinder so that the drag coefficient and rotational inertia were known and tabulated values. The velocity was set to a constant 10 m/s, the CoM and CoP were assumed to be 1/3 and 2/3 along the total length as measured from the end of the sphere, respectively, and the drag force and stabilizing torque were calculated at $\theta = 90°$ and assumed constant for the rotation process. With these parameters, the rotational kinematic equation predicted a turnaround time of 60 ms for an initial condition of $\theta_o = 180°$ which indicated its strong potential for self-righting and stabilizing capabilities.

The final prototype of the badminton tensegrity structure was additionally simulated using computational fluid dynamics (CFD) inside ANSYS Fluent for a numerical verification of its drag behavior (Fig. 5.11). The drag coefficient was calculated to be 0.49, which is reasonable given that the projected area of the structure is dominated by the cone. The estimated turnaround time is then higher than the initial solution, approximately 100 ms but well within the timescale of a drop event. Most importantly the cone is confirmed to act as the center of pressure for the fundamental operating principle of the design.

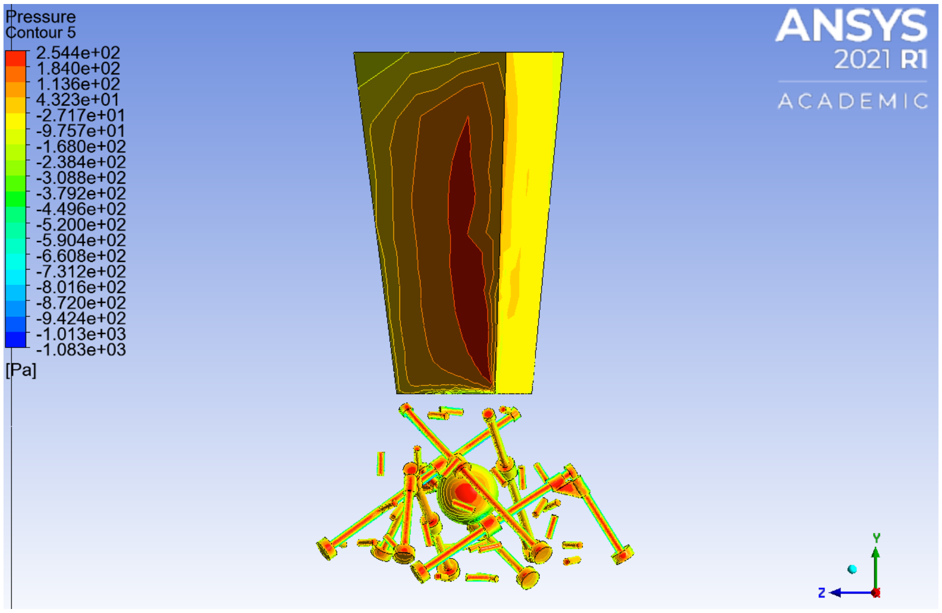

Figure 5.11: Pressure distribution on the badminton tensegrity structure. Air flow is directed into the page.

Although the aerodynamic properties of the badminton birdie stabilize it along its flight trajectory and enable it to land nose-down, it has no way of maintaining its landing orientation after the initial impact with the ground. For the badminton tensegrity structure, design modifications are therefore needed to widen the landing footprint and prevent the structure from rolling or tipping.

The icosahedral tensegrity structure rests on an equilateral triangular face and will roll when its CoM shifts past the bounds of this base triangle (Fig. 5.12). The rotation axis is any edge of the base triangle since those three rotation directions represent the modes of minimum activation energy for rolling the structure [81].

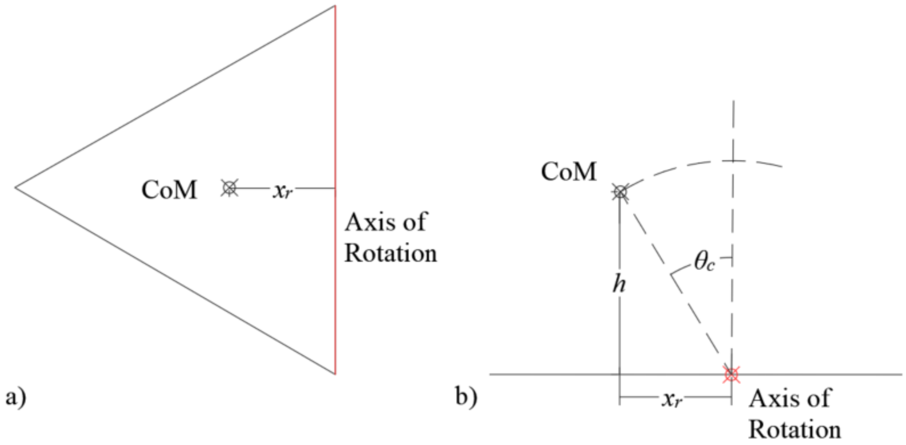

Figure 5.12: Rotation of tensegrity structure: a) top view and b) 2D side view of CoM moving over base triangle.

The critical tipping angle $\theta_c$ occurs at the instant the CoM passes over the rotation axis and can be found through geometry given the base height of the CoM $h$ and its horizontal distance to the rotation axis $x_r$. It can be expressed as

$$\theta_c = \arctan \frac{x_r}{h} \tag{5.2}$$

With the addition of the badminton cone to the tensegrity structure, $h$ will increase to a new value $h_2$, and the structure will tip more easily with the subsequent decrease in $\theta_c$. To prevent premature tipping, rod extensions can be added along the outer ring of the tensegrity structure in the form of landing gear that widen the tensegrity's stance on the ground. The legs form a hexagonal footprint that is well aligned with the base triangle's primary tipping directions (Fig. 5.13).

To maintain the same $\theta_c$ as before, the hexagonal footprint must have, at minimum, an apothem $x_{r,hex}$ of

$$x_{r,hex} = \frac{x_r}{h} h_2 \tag{5.3}$$

This imposes a design constraint on the hardware needed to stabilize the structure after its initial impact with the ground. When the structure bounces upon impact with the ground, it must not tilt past this critical angle for the structure to remain upright. The time

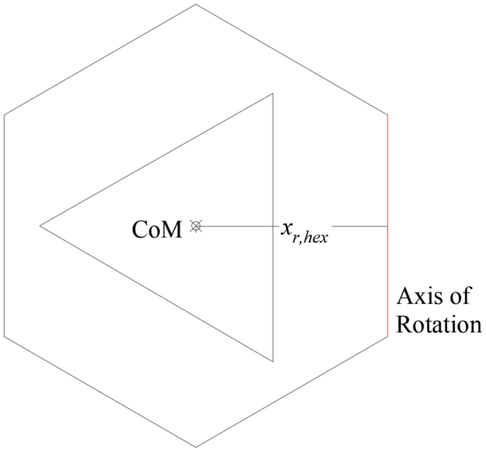

Figure 5.13: Top view of tensegrity structure's widened hexagonal footprint

scale of the bounces is not sufficient for the aerodynamic properties of the badminton cone to re-stabilize the structure, so the post-impact orientation control depends entirely upon the performance of the landing gear. The stability properties of the badminton tensegrity prototype were calculated through the above equations using values measured in Fusion 360 computer-aided design (CAD) software (Table 5.6). Note that a minimum value of 10 cm for $x_{r,hex}$ was needed to maintain a constant $\theta_c$ after the addition of the cone. Based on the structure geometry and mounting points of the landing leg extensions it was convenient to expand $x_{r,hex}$ to its current value of 18 cm for additional safety against tipping.

| **Tensegrity** | **$h$ (cm)** | **$x_r$ (cm)** | **$\theta_c$ (°)** |
|---|---|---|---|
| Standard | 12 | 6 | 26.6 |
| Badminton | 20 | 18 | 42.0 |

Table 5.6: Ground stability parameters of badminton tensegrity prototype

For the badminton tensegrity structure hardware, a lightweight cone is attached to the top face of the tensegrity and the landing gear leg extensions are connected to each rod (Fig. 5.14).

The cone is made by weaving thin carbon fiber shafts through a thin plastic sheet and attaching them with 3D-printed polylactic acid (PLA) brackets to the rod ends of the top face (Fig. 5.15a). Due to the limiting factor of three attachment points, the cone takes on the shape of a triangular prism, but the difference is acceptable compared to the additional mass and complexity of adding circular struts to brace the interior of the cone and form a round cross section. When resting on its base triangle, the tensegrity has three rods in contact with the ground and the remaining three rods are suspended in parallel above them.

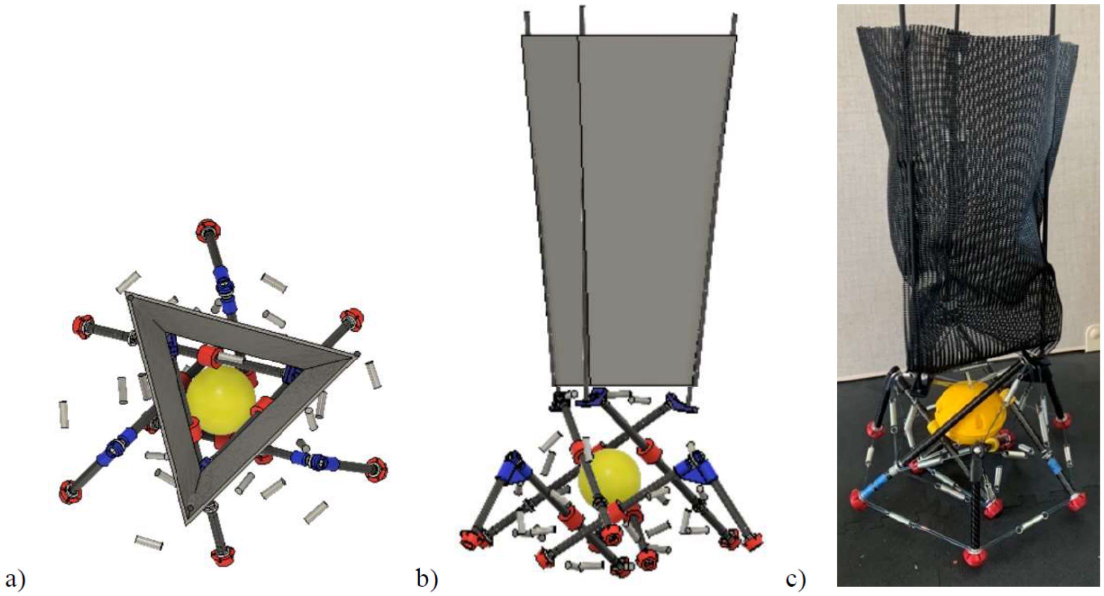

Figure 5.14: a) Top and b) side views of CAD model compared to the c) the final hardware prototype. Cables are omitted for clarity.

Due to the differences in endcap locations, they require two different types of landing gear: first, a set of TPU joints to connect a perpendicular leg extension (Fig. 5.15b), and second, a set of threaded rods to connect an in-line leg extension (Fig. 5.15c). Spring-cable tensile components are utilized to secure the ends of the leg extensions to one another and create the hexagonal footprint of the landing gear.

Figure 5.15: Detail CAD views of a) cone rod bracket, b) perpendicular leg extension, and c) in-line leg extension

## Drop Test Experiments

The badminton tensegrity structure was dropped from the top of a building (22 m) to validate the in-air reorientation behavior and the stability of the landing gear during post-impact bouncing. For the initial conditions of each test, the robot was held at rest horizontally ($\theta_i = 90^\circ$) before release. A sensor board contained in the payload used accelerometers and an IMU to record the structure's acceleration and orientation data, respectively. The data were compared to videos of the drop to verify the orientation of the robot throughout the drop event.

Over $N = 30$ tests the badminton tensegrity structure had an 86.7% success rate in achieving the desired final orientation (Table 5.7). In all tests the badminton structure self-righted along its falling trajectory and impacted on the correct face. The landing gear then proved extremely effective at stabilizing the structure against the subsequent random bounces. Peak impact accelerations of the payload were averaged across all tests and demonstrate the protection provided by the tensegrity structure. This is again using the reference calibration of the sensor payload without a tensegrity that measured a peak impact acceleration of approximately 400 g when dropped from a height of only 5 m.

| **Number of Tests** | **Impact Orientation Success Rate (%)** | **Final Orientation Success Rate (%)** | **Average Peak Acceleration (g)** |
|---|---|---|---|
| 30 | 100 | 86.7 | 328 |

Table 5.7: Ground stability parameters of badminton tensegrity prototype

The test data (Fig. 5.16) indicate that the structure self-righted within 1 second after being released. Note that the target orientation is at $\theta = 0^\circ$ and that any tilting of the structure will result in a positive angular error measured by the IMU regardless of direction. Due to the sensing fusion algorithms on the IMU there is noise in the orientation data from the sudden impact and high frequency vibration before it settles to a final resting value. It takes approximately half a second for the initial rotation needed to align the structure with the vertical axis, then another half second for the overshoot correction and full stabilization. This behavior was additionally confirmed by comparing against slow-motion frames of the drop test videos. Overall, the results verify the rapid convergence of the structure to its correct orientation during free-fall as predicted by the rotation model.

A closer examination of the accelerometer data reveals key insights into the impact performance of the badminton tensegrity structure (Fig. 5.17). Ten representative tests are plotted together with the timescale normalized around the peak acceleration value. These accelerations are naturally higher than those experienced by the standard tensegrity structure due to the additional hardware weight, but they compare favorably to those of the asymmetrically-weighted self-righting tensegrity. Post-drop analysis of the hardware revealed that the structure did not experience failures such as spring deformation or rod cracking until

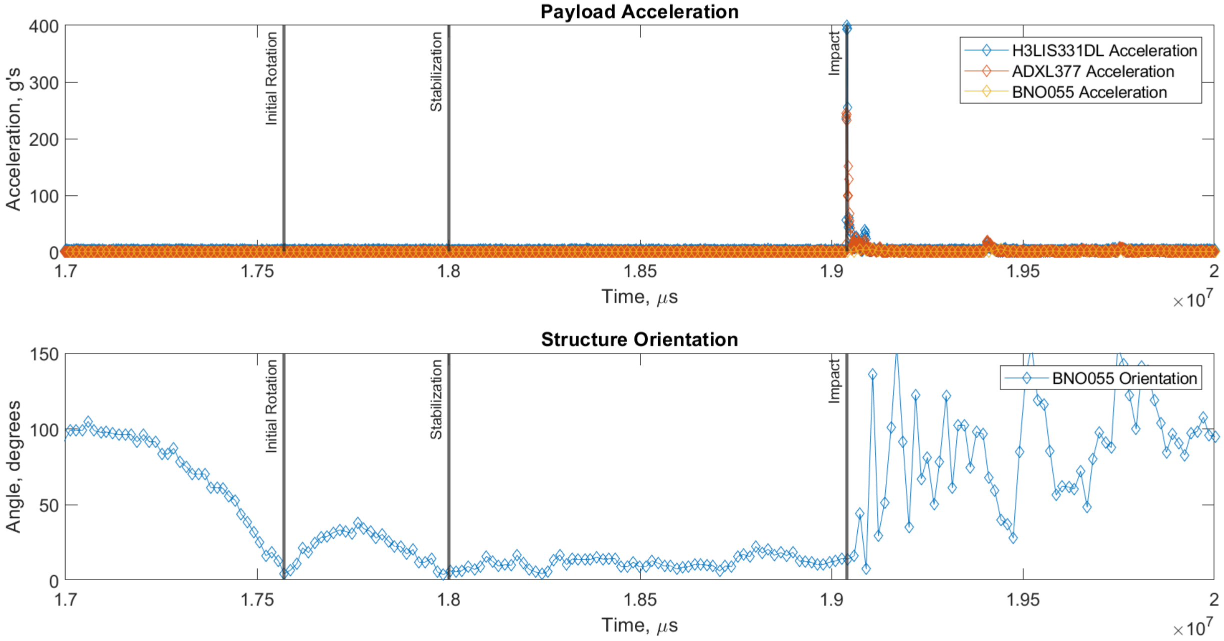

Figure 5.16: Experimental drop test data. Acceleration (top) and angular position (bottom) over time.

over 50 drops (including all tests of previous iterations before the final prototype). This is on the lower end of the expected life cycle range for the deployable tensegrity landers, but the successful self-righting capabilities is a valuable tradeoff against the impact performance. It is important to note that the acceleration profiles of all tests are very closely aligned, indicating the consistent impact response of the structure when it is repeatedly landing on the same target face. Overall, the closed-face landings indeed behave as predicted by the analytical models of the structure.

In experimental testing, it was observed that the badminton tensegrity structure had a reduced bounce height compared to other designs, potentially due to the additional damping provided by the cone. This reduced bouncing minimized the potential rotation of the structure and greatly benefited the success rate of the landing gear. Further work is needed to study the effects of different hardware modifications on the vibration and damping response of tensegrity structures, as this may prove to be an effective method of mitigating the dynamic post-impact bouncing usually experienced upon landing [82, 83].

Although the badminton tensegrity structure has proven to be both more reliable in terms of overall success rate and more mass-efficient through its lightweight design and lower impact accelerations, it does have a limiting factor when compared to the scalability of conventional tensegrity structures. Due to the aspect ratio of the cone to the tensegrity sphere, it becomes quickly impractical to build badminton tensegrity structures to carry

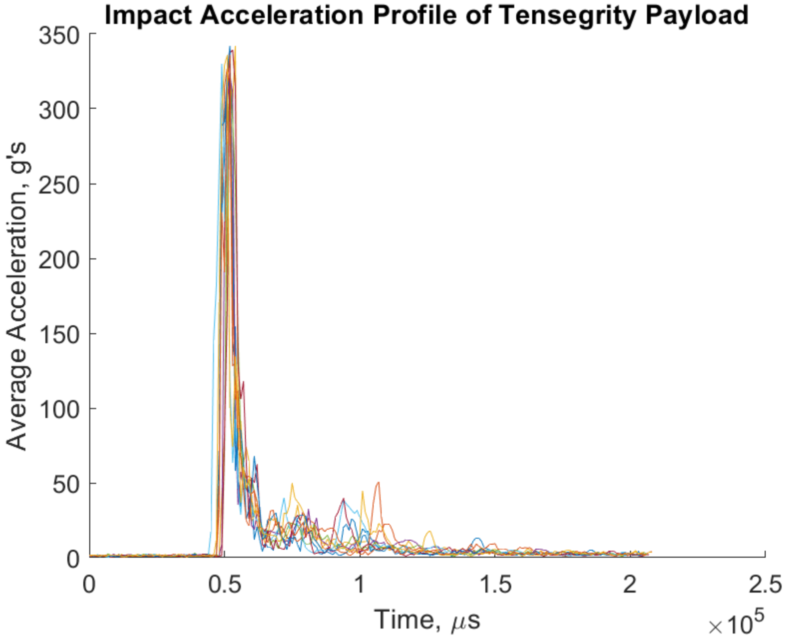

Figure 5.17: Sample cluster of badminton tensegrity drop test accelerometer data ($N = 10$)

larger and heavier payloads. Nevertheless, so far it has already demonstrated tremendous advantages in the autonomous deployment of small sensor payloads and is currently the most reliable and efficient design within its size class of self-righting tensegrity landers [84].

## 5.4 Discussion

The payload deployment platform's self-righting capabilities have an exciting potential application to design directional strength and stiffness into a stronger and more robust tensegrity robot. The orientation control forces the robot towards the targeted landing face while it is falling to guarantee the robot's impact orientation for any deployment of sufficiently high altitude. Aligning the target landing face with the previously identified minimum-impact orientation combines the structure's self-righting capabilities and impact-resistance for an optimal landing experience.

Analytical models of the structure coupled with the pattern of distributed spring deformation reveal locations where the tensegrity can improve its impact resistance. In any given landing orientation, there exists a subset of the tensegrity springs that will lose tension and go slack due to the inherent dynamics of the system. While these springs are necessary to maintain the robot's tension network in a static position, during dynamic events they do not contribute to the impact resistance of the structure. By deliberately using lighter, less stiff springs for these specific cables and switching to heavier, stiffer springs for those cables bearing most of the impact, there is the flexibility to improve impact performance while reducing the structure weight. Since the weight of all the springs makes up over a third of the system weight, any reduction that can be made will greatly reduce the expected impact velocity and forces on the robot. Individually tuning spring parameters will optimize the impact response of the structure when landing in a guaranteed impact direction due to the robust self-righting capabilities. Overall, this technique leverages self-righting to introduce directional strength for a highly reusable and more impact-resistant structure.

This asymmetric spring concept was applied to the 38" robot with a 5 lb. payload. When landing in the targeted self-righting orientation of a closed-face landing, twelve of the structure's thirty-six springs (specifically, the six springs in the top and bottom base triangles and the six vertical springs as defined in the SVD model) do not contribute to payload protection due to loss of tension or negligible extension during impact. Furthermore, three specific springs (the three upper diagonal springs) on the exterior structure consistently exhibited the most deformation post-impact even if they had been newly replaced. A modified design simultaneously reduced the weight of the 12 slack springs and increased the strength of the three most heavily loaded springs for an overall weight decrease of 0.6 lb. Low-altitude tests showed that the payload experienced a new decrease in impact acceleration of 4.7%, while the robot had an increased lifespan due to a reduction of spring overextension. The technique demonstrated here shows great promise and will be a key technique in future work where larger payloads may be carried, as they simultaneously result in orientation control and superior impact performance for a net decrease in system mass. These improvements are expected to increase as the robot more nearly matches terminal velocity for large drops, as the total amount of energy to be dissipated scales with velocity squared.

Future work will use orientation control to selectively tailor the individual spring stiffness in such a way to best optimize the structure's weight and impact resistance. Stronger and lighter robots may also create opportunities to reintegrate locomotion control with the asymmetrically-weighted solution, although further investigation is needed to identify the effects of asymmetric weighting and spring constants on locomotion performance and carefully select the active, actuated cables on the structure [85]. This will turn the tensegrity into an Unmanned Ground Vehicle (UGV) contained in the same hardware unit as the lander and open new applications in the autonomous deployment of ground-based sensors.

# Chapter 6

# Conclusions and Future Research

This dissertation established a unified design methodology for the deployment of impact-resistant tensegrity landers carrying critical sensor payloads for emergency response operations.

Starting from a series of high-level design equations used to narrow the parameter search space and propose valid tensegrity lander configurations, the stationary robot six-bar tensegrity platform was designed and prototyped. The construction is robust, scalable, and modular across multiple iterations of the robot that tune factors such as size, weight, and spring stiffness. Analytical models such as the mass-spring-damper were shown to accurately capture both the deformation and energy dissipation of the structure during impact in ideal landing orientations. Lumped mass models simulated in MATLAB and ANSYS provided a more accurate prediction of the impact performance and were used as upper-bound estimates of the peak payload acceleration experienced during landing.

The models and simulation were validated through a wide variety of drop test experiments to build the largest current repository of tensegrity lander drop test data, including the highest-altitude drops of tensegrity structures to date. The data was used to demonstrate the impact-resistant design and characterize the impact response of the structure. Scaling trends between peak payload acceleration and the design parameters were observed in the data, and a series of surface curve fits were generated to propose empirical scaling laws for future designs of tensegrity landers. These serve as conservative damage boundaries for the design of safe impact-resistant tensegrity landers.

A promising new application emerged from the drop test data, motivated by the identification of the closed-face landing orientation as the optimal impact-dissipating mode. In addition to protecting the payload, orientation control can also be used to deploy position-dependent sensors such as cameras or radio antennas. Two newly designed structures, an asymmetrically-weighted robot and a badminton-inspired robot, were built and validated in experiment as self-stabilizing tensegrity landers capable of maintaining a given landing orientation after impact. The guaranteed landing orientation provides the flexibility to design tailored material properties to introduce directional stiffness into the compression modes of the tensegrity for a new generation of optimized structure.

Overall, the work contributes design methods, reorientation capabilities, and validated hardware prototypes to the grand challenge of tensegrity robotics: demonstrating a fully autonomous tensegrity robot capable of safely navigating through unstructured terrain.

## Future Research

The research here has a rich potential for future work towards realizing such tensegrity robots with robust and autonomous capabilities.

For the hardware design of tensegrity landers, improved modelings methods to calculate and predict the impact performance will accelerate the design process of future iterations. The work presented here used conservative estimates for the damage boundaries, meaning that the landers may be overdesigned and inefficiently make use of the selected material properties. Critical damage thresholds for both human impact and electronics payload protection may also be excessively conservative, where the time of impact should also be more carefully considered alongside an absolute magnitude for peak payload acceleration. Since the peak g value in the drop test experiments is sustained for only a small fraction of the tensegrity impact time, which in itself is already comparatively low relative to the timescale referenced in the literature, it is entirely possible that tensegrity structures can provide even more impact protection than previously known. For a better understanding of the impact, an analytical mapping between the hardware parameters such as rod and cable stiffness, and the effective stiffness of the structure under highly dynamic impact events, is necessary [86]. Furthermore, as previously mentioned, increasing the range and resolution of the drop test data can lead to more accurate curve fits and design laws that can also account for the asymptotic behavior of the peak acceleration with respect to drop height and terminal velocity. While the surface fits indicated similar dependency of the peak acceleration on all design parameters, for this multifaceted design problem where numerous hardware parameters can be tuned simultaneously it is perhaps insufficient to consider 3-dimensional surface fits to visualize the scaling trends. Instead, further experiment data is needed to form a non-linear multi-parameter model that can optimally capture the aggregated behavior of the tensegrity landers under all landing conditions.

In terms of re-integrating the landing robustness properties of a stationary tensegrity robot with the ground locomotion capabilities of a mobile tensegrity robot, one of the most promising paths forward is to leverage reorientation and landing control. For the optimized structure with directional stiffness, certain cables were chosen to be stiffer than others to withstand impact, while others had reduced stiffness because they did not contribute to impact protection. It is precisely these more elastic cables that are ideal candidates for cable-based locomotion that prefers low cable stiffnesses to improve locomotion efficiency. Since the structure will be rolling, the asymmetrically-weighted structure must be redesigned to avoid uneven gaits, or the weights could also be leveraged in new locomotion schemes that do not depend on cable retraction [87, 88]. The badminton-inspired structure would also need to be redesigned as it would not be capable of rolling due to its externally-attached cone and landing legs. A potential solution is to use a series of vanes on the external rods of the tensegrity structure to control its flight direction much like the feathers on an arrow [89]. These vanes would be lightweight and flexible and would not impede any rolling motions of the mobile tensegrity lander. Further investigation is also needed to determine optimal path planning and locomotion algorithms for an underactuated tensegrity robot, since the stiff impact-resistant cables would be inaccessible to the motors. Overall the combination of both design paradigms will return the tensegrity lander to its original roots as a robust, flexible, and multi-functional robot capable of high-altitude deployment, impact-resistant landings, and autonomous locomotion across unstructured terrain. Continued work on these impact-resistant tensegrity robots will streamline disaster response operations on Earth to provide critical real-time data, assist with relief efforts, and save lives.

# Bibliography

[1] R. R. Murphy, *Disaster Robotics*. The MIT Press, 2014.

[2] M. Tardiff, *Development of a high altitude low opening humanitarian airdrop system*, US Army Natick Soldier RD&E Center, 2017.

[3] K. Snelson, “Continuous tension, discontinuous compression structures,” 3 169 611, 1965.

[4] B. R. Fuller, “Tensile-integrity structures,” 3063521 A, 1962.

[5] R. Skelton and M. de Oliveira, *Tensegrity Systems*. Springer, 2009.

[6] R. Skelton and C. Sultan, “Controllable tensegrity: A new class of smart structure,” in *Proceedings of SPIE 3039, Smart Structures and Materials 1997: Mathematics and Control in Smart Structures*, 1997.

[7] K. Snelson, “The art of tensegrity structures,” *International Journal of Space Structures*, vol. 27, 2-3 2021.

[8] D. Ingber, “Tensegrity I. Cell structure and hierarchical systems biology,” *Journal of Cell Science*, vol. 116, 7 2003.

[9] ——, “Tensegrity II. How structural networks influence cellular information processing networks,” vol. 116, 8 2003.

[10] C. Chen and D. Ingber, “Tensegrity and mechanoregulation: From skeleton to cytoskeleton,” *Osteoarthritis and Cartilage*, vol. 7, 1999.

[11] C. Sultan and R. Skelton, “Force and torque smart tensegrity sensor,” in *Proceedings of SPIE 3323, Smart Structures and Materials 1998: Mathematics and Control in Smart Structures*, 1998.

[12] J. J. Rimoli and R. Kumar Pal, “Mechanical response of 3-dimensional tensegrity lattices,” *Composites Part B*, vol. 115, 2017.

[13] S. Jiang, R. Skelton, and E. Peraza Hernandez, “Analytical equations for the connectivity matrices and node positions of minimal and extended tensegrity plates,” *International Journal of Space Structures*, vol. 35, 3 2020.

[14] D. Shah, J. Booth, R. Baines, K. Wang, M. Vespignani, K. Bekris, and R. Kramer-Bottiglio, “Tensegrity robotics,” *Soft Robotics*, vol. 0, 2021.

[15] Y. Liu, Q. Bi, X. Yue, J. Wu, B. Yang, and Y. Li, "A review on tensegrity structures-based robots," *Mechanism and Machine Theory*, vol. 168, 2022.

[16] J. Mirats Tur, S. Hernàndez Juan, and A. Rovira, "Dynamic equations of motion for a 3-bar tensegrity based mobile robot," in *IEEE Conference on Emerging Technologies and Factory Automation (EFTA)*, 2007.

[17] H. Kino, Y. Matsutani, S. Katakabe, and H. Ochi, "Prototype of a tensegrity robot with nine wires for switching locomotion and calculation method of the balancing internal force," in *IEEE International Symposium on Robotics and Intelligent Sensors (IRIS)*, 2016.

[18] E. Jung, V. Ly, N. Cessna, M. Ngo, D. Castro, V. SunSpiral, and M. Teodorescu, "Bio-inspired tensegrity flexural joints," in *Proceedings of 2018 IEEE International Conference on Robotics and Automation (ICRA)*, 2018.

[19] A. P. Sabelhaus, H. Ji, P. Hylton, Y. Madaan, C. Yang, A. M. Agogino, J. Friesen, and V. SunSpiral, "Mechanism design and simulation of the ULTRA spine: A tensegrity robot," in *Proceedings of the ASME International Design Engineering Technical Conference (IDETC)*, vol. 5A: 39th Mechanisms and Robotics Conference, 2015.

[20] J. Friesen, A. Pogue, T. Bewley, M. de Oliveira, R. Skelton, and V. SunSpiral, "DuCTT: A tensegrity robot for exploring duct systems," in *Proceedings of 2014 IEEE International Conference on Robotics and Automation (ICRA)*, 2014.

[21] F. Carreño and M. Post, "Design of a novel wheeled tensegrity robot: A comparison of tensegrity concepts and a prototype for travelling air ducts," *Robotics and Biomimetics*, vol. 5, 2018.

[22] H. Lee, Y. Jang, J. Choe, S. Lee, H. Song, J. Lee, N. Lone, and J. Kim, "3D-printed programmable tensegrity for soft robotics," *Science Robotics*, vol. 5, 2020.

[23] V. SunSpiral, G. Gorospe, J. Bruce, A. Iscen, G. Korbel, S. Milam, A. K. Agogino, and D. Atkinson, "Tensegrity based probes for planetary exploration: Entry, descent and landing (EDL) and surface mobility analysis," *International Journal of Planetary Probes*, 2013.

[24] A. P. Sabelhaus, J. Bruce, K. Caluwaerts, P. Manovi, R. F. Firoozi, S. Dobi, A. M. Agogino, and V. Sunspiral, "System design and locomotion of SUPERball, an untethered tensegrity robot," in *2015 IEEE International Conference on Robotics and Automation (ICRA)*, 2015.

[25] L.-H. Chen, K. Kim, E. Tang, K. Li, R. House, A. M. Agogino, A. K. Agogino, V. Sunspiral, and E. Jung, "Soft spherical tensegrity robot design using rod-centered actuation and control," *ASME Journal of Mechanisms and Robotics*, vol. 9, 2 2017.

[26] G. Tibert and S. Pellegrino, "Review of form-finding methods for tensegrity structures," *International Journal of Space Structures*, vol. 18, 4 2003.

[27] B. Fuller, *Sixty-strut tensegrity sphere*, UW Madison, 1979.

[28] S. Guest, "The stiffness of tensegrity structures," *IMA Journal of Applied Mathematics*, vol. 57, 2011.

[29] R. Skelton, R. Adhikari, J.-P. Pinaud, W. Chan, and J. Helton, "An introduction to the mechanics of tensegrity structures," in *Proceedings of the 40th IEEE Conference on Decision and Control*, 2001.

[30] R. Skelton, J. Helton, R. Adhikari, J.-P. Pinaud, and W. Chan, "An introduction to the mechanics of tensegrity structures," in *Handbook of Mechanical Systems Design*, CRC Press, 2001.

[31] A. Amendola, G. Carpentieri, M. de Oliveira, R. Skelton, and F. Fraternali, "Experimental investigation of the softening-stiffening response of tensegrity prisms under compressive loading," *Composite Structures*, vol. 117, 2014.

[32] F. Fraternali, G. Carpentieri, and A. Amendola, "On the mechanical modeling of the extreme softening/stiffening response of axially loaded tensegrity prisms," *Journal of the Mechanics and Physics of Solids*, vol. 74, 2015.

[33] H. Murakami, "Static and dynamic analyses of tensegrity structures. part 1. nonlinear equations of motion," *International Journal of Solids and Structures*, vol. 38, 2001.

[34] ——, "Static and dynamic analyses of tensegrity structures. part 2. quasi-static analysis," *International Journal of Solids and Structures*, vol. 38, 2001.

[35] C. Sultan, M. Corless, and R. Skelton, "Linear dynamics of tensegrity structures," *Engineering Structures*, vol. 24, 2002.

[36] P. Wenger and D. Chablat, "Kinetostatic analysis and solution classification of a class of planar tensegrity mechanisms," *Robotica*, vol. 37, 7 2018.

[37] M. Arsenault and C. M. Gosselin, "Kinematic, static, and dynamic analysis of a planar one-degree-of-freedom tensegrity mechanism," *ASME Journal of Mechanical Design*, vol. 127, 2005.

[38] ——, "Kinematic, static, and dynamic analysis of a spatial three-degree-of-freedom tensegrity mechanism," *ASME Journal of Mechanical Design*, vol. 128, 2006.

[39] K. Caluwaerts, J. Despraz, A. Iscen, A. Sabelhaus, J. Bruce, B. Schrauwen, and V. SunSpiral, *Journal of the Royal Society Interface*, 2014.

[40] C. Sultan and R. Skelton, "Tendon control deployment of tensegrity structures," in *Proceedings of SPIE 3323, Smart Structures and Materials 1998: Mathematics and Control in Smart Structures*, 1998.

[41] P. Schorr, V. Bohm, K. Zimmermann, and L. Zentner, "An approach to the estimation of the actuation parameters for mobile tensegrity robots with tilting movement sequences," in *2018 International Conference on Reconfigurable Mechanisms and Robots (ReMAR)*, 2018.

[42] D. Surovik, J. Bruce, K. Wang, M. Vespignani, and K. Bekris, “Any-axis tensegrity rolling via symmetry-reduced reinforcement learning,” in *Proceedings of the 2018 International Symposium on Experimental Robotics*, 2018.

[43] D. Surovik, K. Wang, M. Vespignani, J. Bruce, and K. Bekris, “Adaptive tensegrity locomotion: Controlling a compliant icosahedron with symmetry-reduced reinforcement learning,” *The International Journal of Robotics Research*, 2019.

[44] J. Kimber, Z. Li, A. Petridou, T. Sipple, K. Barhydt, J. Boggs, L. Dosiek, and J. Rieffel, “Low-cost wireless modular soft tensegrity robots,” in *2nd IEEE International Conference on Soft Robotics (RoboSoft)*, 2019.

[45] S. Mintchev, D. Zappetti, J. Willemin, and D. Floreano, “A soft robot for random exploration of terrestrial environments,” in *2018 IEEE International Conference on Robotics and Automation (ICRA)*, 2018.

[46] C. Sultan and R. Skelton, “Deployment of tensegrity structures,” *International Journal of Solids and Structures*, vol. 40, 2003.

[47] J. J. Rimoli, “On the impact tolerances of tensegrity-based planetary landers,” in *57th AIAA/ASCE/AHS/ASC Structures, Structural Dynamics, and Materials Conference*, AIAA SciTech Forum, 2016.

[48] J. Roth and T. McCarthy, “Optimizing compressive load capacity for differing tensegrity geometries,” *Computers and Structures*, vol. 249, 2021.

[49] M. Vespignani, J. Friesen, V. SunSpiral, and J. Bruce, “Design of SUPERball v2, a compliant tensegrity robot for absorbing large impacts,” in *IEEE/RSJ International Conference on Intelligent Robots and Systems (IROS)*, 2018.

[50] M. Fanton, P. Glick, J. Bruce, K. Caluwaerts, J. Friesen, and V. SunSpiral, “Robust and efficient multistage braking system for cable driven robots,” in *Proceedings of the 13th International Symposium on Artificial Intelligence, Robotics, and Automation in Space (i-SAIRAS)*, 2016.

[51] Z. Cheema, S. Sonatina, and J. Ying, “Spherical tensegrity drop test for NASA missions: A balancing act of robustness and compliance,” Master’s of Engineering Capstone Report, University of California, Berkeley, 2018.

[52] S. W. Lye, M. Y. Teo, and S. C. Lew, “A study of shock characterization for protective packaging design,” *Journal of Materials Engineering and Performance*, vol. 4, 3 1995.

[53] J. J. Rimoli, “A reduced-order model for the dynamic and post-buckling behavior of tensegrity structures,” *Mechanics of Materials*, vol. 116, 2017.

[54] S. Palumbo, A. Rosario Carotenuto, A. Cutolo, L. Deseri, and M. Fraldi, “Nonlinear elasticity and buckling in the simplest *Soft*-strut tensegrity paradigm,” *International Journal of Non-Linear Mechanics*, vol. 106, 2018.

[55] K. Pajunen, P. Johanns, R. Kumar Pal, J. J. Rimoli, and C. Daraio, "Design and impact response of 3d-printable tensegrity-inspired structures," *Materials and Design*, vol. 182, 2019.

[56] S. Goyal, J. Papadopoulos, and P. Sullivan, "Shock protection of portable electronic products: Shock response spectrum, damage boundary approach, and beyond," *Shock and Vibration*, vol. 4, no. 3, 1997.

[57] J. Wu, G. Song, C.-p. Yeh, and K. Wyatt, "Dropampact simulation and test validation of telecommunication products," in *ITherm'98. Sixth Intersociety Conference on Thermal and Thermomechanical Phenomena in Electronic Systems*, 1998.

[58] Y. Yau and S. Hua, "A comprehensive review of drop impact modeling on portable electronic devices," *Applied Mechanics Reviews*, vol. 64, 2 2011.

[59] K. Li and A. Darby, "Modeling a buffered impact damper system using a spring-damper model of impact," *Structural Control and Health Monitoring*, vol. 16, 2009.

[60] M. Nagurka and S. Huang, "A mass-spring-damper model of a bouncing ball," in *Proceedings of the American Control Conference*, 2004.

[61] S. Goodwill and S. Haake, "Spring damper model of an impact between a tennis ball and racket," in *Proceedings of the Institution of Mechanical Engineers Part C*, vol. 215.

[62] L. Zhao and E. Peraza Hernandez, "Tensegrity structures for impact energy absorption and dissipation in planetary landers," in *ASCE Earth and Space Conference*, 2021.

[63] K. Jackson, J. Littell, M. Annett, and I. Haskin, *Finite element simulations of two vertical drop tests of F-28 fuselage sections*, NASA Technical Memorandum.

[64] A. Zhang, B. Cera, and A. M. Agogino, "Characterization of six-bar spherical tensegrity topologies," in *Proceedings of the IASS Symposium*, 2018.

[65] M. Polanco and J. Littell, "Vertical drop testing and simulation of anthropomorphic test devices," in *AHS International 67th Annual Forum and Technology Display*, 2011.

[66] J. Littell and S. Kellas, *Full-scale passive earth entry vehicle landing tests: Methods and measurements*, NASA Technical Memorandum, 2018.

[67] C. White, K. van der Walde, and J. Tippmann, "An experimental investigation of the dynamics of the MSL Rover landing event," in *9th AIAA Gossamer Spacecraft Forum*, 2008.

[68] C. Bir, D. Viano, and A. King, "Development of biomechanical response corridors of the thorax to blunt ballistic impacts," *Journal of Biomechanics*, vol. 37, 2004.

[69] D. Viano, C. Bir, T. Walilko, and D. Sherman, "Ballistic impact to the forehead, zygoma, and mandible: Comparison of human and frangible dummy face biomechanics," *Journal of Trauma*, vol. 56, 6 2004.

[70] A. Y. Alhaddad, J.-J. Cabibihan, A. Hayek, and A. Bonarini, "A low-cost test rig for impact experiments on a dummy head," *HardwareX*, vol. 6, 2019.

[71] J. Stuhmiller, P. Rigby, and J. Wong, *Estimate of human injury from humanitarian air drop*, L-3/Jaycor, 2010.

[72] D. Goldman and P. Umbanhowar, "Scaling and dynamics of sphere and disk impact into granular media," *Physical Review E*, vol. 77, 2 2008.

[73] P. Umbanhowar and D. Goldman, "Granular impact and the critical packing state," *Physical Review E*, vol. 82, 1 2010.

[74] *Autonomous deployment of sensors through airdrop operations*, Last Accessed 7 December 2020, US Army SBIR Solicitation, 2019. [Online]. Available: `https://www.sbir.gov/node/1531691`.

[75] K. Kim and A. M. Agogino, "Spin axis stabilization about arbitrary axis using two reaction wheels for hopping tensegrity robots," in *Proceedings of the Conference on Decision and Control*, 2016.

[76] E. M. Levin, "Experiments with loaded dice," *American Journal of Physics*, vol. 51, 2 1983.

[77] A. Zhang, D. Hutchings, M. Gupta, and A. M. Agogino, "Orientation control of self-righting tensegrity landers," in *Proceedings of the ASME International Design Engineering Technical Conference (IDETC)*, vol. 8B: 45th Mechanisms and Robotics Conference, 2021.

[78] B. D. Texier, C. Cohen, D. Quéré, and C. Claneta, "Shuttlecock dynamics," in *9th Conference of the International Sports Engineering Association (ISEA)*, Procedia Engineering, vol. 34, 2012.

[79] C. S. Lin, C. Chua, and J. Yeo, "Badminton shuttlecock stability: Modelling and simulating the angular response of the turnover," in *Proceedings of the Institution of Mechanical Engineers, Part P*, Journal of Sports Engineering and Technology, vol. 230, 2016.

[80] Y. Konishi, Y. Matsushima, T. Misaka, H. Okuizumi, K. Tanaka, and S. Obayashi, "Effect of camber on badminton shuttlecock," in *12th Conference of the International Sports Engineering Association (ISEA)*, 2018.

[81] K. Kim, A. K. Agogino, D. Moon, L. Taneja, A. Toghyan, B. Dehghani, V. SunSpiral, and A. M. Agogino, "Rapid prototyping design and control of tensegrity soft robot for locomotion," in *Proceedings of the 2014 IEEE International Conference on Robotics and Biomimetics (ROBIO)*, 2014.

[82] I. Oppenheim and W. Williams, "Vibration of an elastic tensegrity structure," *European Journal of Mechanics A/Solids*, vol. 20, 2001.

[83] N. Bel Hadj Ali and I. Smith, "Dynamic behavior and vibration control of a tensegrity structure," *International Journal of Solids and Structures*, vol. 47, 2010.

[84] A. Zhang, A. Ibarra, and A. M. Agogino, “Badminton-inspired self-righting tensegrity landers,” in *26th AIAA Aerodynamic Decelerator Systems Technology Conference and Seminar (ADSTCS)*, 2022.

[85] D. Zhu, H. Deng, and X. Wu, “Selecting active members to drive the mechanism displacement of tensegrities,” *International Journal of Solids and Structures*, vol. 191-192, 2020.

[86] K. Yildiz and G. Lesieutre, “Effective beam stiffness properties of $n$-strut cylindrical tensegrity towers,” *AIAA Journal*, vol. 57, no. 5, 2019.

[87] T. Rhodes and V. Vikas, “Compact tensegrity robots capable of locomotion through mass-shifting,” in *Proceedings of the ASME International Design Engineering Technical Conferences and Computers and Information in Engineering Conference IDETC/CIE*, 2019.

[88] R. Goyal, M. Chen, M. Majji, and R. Skelton, “Gyroscopic tensegrity robots,” *IEEE Robotics and Automation Letters*, vol. 5, no. 2, 2020.

[89] T. Miyazaki, K. Mukaiyama, Y. Komori, K. Okawa, S. Taguchi, and H. Sugiura, “Aerodynamic properties of an archery arrow,” *Sports Engineering*, vol. 16, 2013.